

UC San Diego

UC San Diego Electronic Theses and Dissertations

Title

Ultra-low noise wavelength multicasting using multi-mode phase-sensitive parametric mixer

Permalink

<https://escholarship.org/uc/item/0t2235zq>

Author

Liu, Lan

Publication Date

2015

Peer reviewed|Thesis/dissertation

UNIVERSITY OF CALIFORNIA, SAN DIEGO

Ultra-low noise wavelength multicasting
using multi-mode phase-sensitive parametric mixer

A dissertation submitted in partial satisfaction of the
requirements for the degree Doctor of Philosophy

in

Electrical Engineering (Photonics)

by

Lan Liu

Committee in charge:

Professor Stojan Radic, Chair
Professor Leonid Butov
Professor Miroslav Krstic
Professor Zhaowei Liu
Professor Shayan Mookherjea

2015

Copyright

Lan Liu, 2015

All Rights Reserved.

The Dissertation of Lan Liu is approved, and it is acceptable in quality and form for publication on microfilm and electronically:

Chair

University of California, San Diego

2015

DEDICATION

*To my parents Kaiying Liu, Fugui Guo
and my husband Jiang Long*

TABLE OF CONTENTS

Signature Page	iii
Dedication.....	iv
Table of Contents	v
List of Figures.....	viii
List of Tables	xiii
List of Abbreviations	xiv
Acknowledgements	xvi
Vita	xx
Abstract of the Dissertation	xxiv
Chapter 1 Introduction.....	1
1.1 Motivation	1
1.2 Dissertation overview	4
Chapter 2 Phase insensitive parametric wavelength multicasting.....	6
2.1 Third order nonlinearity	6
2.2 Parametric amplification	9
2.3 Parametric mixer	15
2.4 Noise analysis.....	18
2.5 Summary.....	22
Chapter 3 Four-mode Phase-Sensitive Wavelength multicasting	23

3.1 Phase sensitive process	24
3.2 Four-mode phase sensitive multicasting	26
3.3 Experimental implementation	31
3.4 Phase-locked loop.....	34
3.5 Phase manipulation.....	39
3.6 Suppression of high order four wave mixing tones.....	42
3.6.1 Numerical simulation	45
3.6.2 Experimental implementation and results	49
3.7 Ultra-low noise wavelength multicasting	57
3.7.1 Numerical simulation in one-stage fiber mixer	57
3.7.2 Experimental characterization on NF and BER performance	59
3.8 Summary.....	63
Chapter 4 All optical regenerative multicaster	65
4.1 Introduction	65
4.2 Operating Principle.....	69
4.3 Experimental Configuration	75
4.4 Amplitude Regeneration.....	77
4.5 Phase Regeneration	80
4.6 Summary.....	84

Chapter 5 One-mode and three-mode phase sensitive wavelength multicasting	86
5.1 Introduction	86
5.2 Theory.....	89
5.3 Experimental demonstration.....	97
5.4 Discussion on ultra-low noise performance	100
5.5 Summary.....	103
Chapter 6 Summary and Future work	105
6.1 Summary.....	105
6.2 Future work	107
Bibliography	111

LIST OF FIGURES

Figure 2.1 Frequency configuration of FWM.	10
Figure 2.2 Energy diagram of FWM elastic process.	12
Figure 2.3 Frequency configurations of FWM effect. (a) fully degenerate and pump nondegenerate one-mode parametric effect. (b) One-pump two-mode parametric effect. (c) Two-pump two-mode parametric effect. (d) Two-pump three-mode parametric effect. (e) Two-pump four-mode parametric effect.	14
Figure 2.4 Fundamental principle for the dual-pump driven parametric wavelength multicasting.	15
Figure 2.5 (a) Simulated configuration of parametric mixer, which is composed of three fiber stages. Inset: frequency configuration of input three waves: two pumps were spaced by 400 GHz, the input signal was 100-GHz offset from the pump at 1550.9 nm.	17
Figure 2.6 Simulated spectrum of wavelength multicasting in a single stage mixer. (a) whole spectrum. (b) expanded spectrum of central 20 signal copies.	21
Figure 2.7 Gain and NF evolution in the 600-m long single stage fiber mixer.	21
Figure 3.1 (a) The basic configuration for PI wavelength multicasting. (b) The basic configuration for PS wavelength multicasting. (c) The simulated configuration for 4MPS multicasting with two pumps and four signals launched into the three-stage parametric mixer.	27
Figure 3.2 Spectral comparison between the 4MPS and PI wavelength multicasting. (a) The input six waves were phase synchronized as 0°. (b) The input six waves $P_1/P_2/S_1/S_2/S_3/S_4$ were arranged as 15°/60°/10°/20°/55°/65°.	29
Figure 3.3 The simulated PS-to-PI G/CE improvements response of the central 24 signal copies for individual input (i.e. $S_1/S_2/S_3/S_4$) phase sweep. (a) phase of S_1 1546.9 nm was swept from 0° to 360°. (b) phase of S_2 1548.5 nm was swept from 0° to 360°. (c) phase of S_3 1550.1 nm was swept from 0° to 360°.	31
Figure 3.4 (a) Experimental configuration including four partitions: coherent wave generation, pump recovery, parametric mixer and DPLL. (b) Part I output, an optical comb with 5-nm 10-dB-bandwidth. (c) Dispersion profile of HNL1. (d) Dispersion profile of HNL2.	33
Figure 3.5 Experimental implementation with DPLL stabilization.	36
Figure 3.6 DPLL instantaneous performance. (a) Three monitored optical channels' power fluctuations. (b) The DC driving signals on two PZTs.	38

Figure 3.7 The signal power spectra with one, two and three monitored channels. Red curve: three monitored channels, blue curves: two monitored channels, black curves: one monitored channel.	39
Figure 3.8 Experimental multicasting (i.e. central 24 copies) output power response by changing signal phase. (a) S_1 1546.9 nm phase is swept over 360° . (b) S_2 1548.5 nm phase is swept over 360° . (c) S_3 1550.1 nm phase is swept over 360° . (d) S_4 1551.7 nm phase is swept over 360°	40
Figure 3.9 Experimental spectra comparison between the PS and the PI multicasting. (a) whole spectrum. (b) a zoom-in view.....	41
Figure 3.10 The schematic of dual-pump seeded parametric wavelength multicasting based on cascaded FWMs between pumps and signals. MI: modulation instability, PC: phase conjugation, BS: Bragg scattering. P_1, P_2 : pumps, S_1 to S_4 : signals, H_1 to H_2 : high order FWM tones. (b) ICC induced by the HoFWM tone..	44
Figure 3.11 Simulated spectra of PS multicasting without and with HoFWM suppression. Red curve: for phase synchronized pumps and signals, there is no HoFWM suppression, signal to HoFWM tones extinction ratio is around 17 dB. Blue curve: for signals with complementary phase setting.....	46
Figure 3.12 Power flow of the central HoFWM term at 1549.3 nm under phase synchronized and complementary settings. Red curves: evolution of the total positive power flow, blue curves: evolution of the total negative power flow, black curves: evolution of total power of the central HoFWM term.....	48
Figure 3.13 Experimental spectra comparison between PS and PI multicasting. Red curve: PS scheme with phase setting A. Blue curve: PI scheme.	50
Figure 3.14 Experimental spectra of PS multicasting with each input signal power of -18 dBm, showing HoFWM suppression by signal phase manipulation. Red curve: PS scheme with phase setting A. Blue curve: PS spectrum with phase setting B.....	51
Figure 3.15 Experimental spectra of PS multicasting with high speed data modulation, where HoFWM tones were thoroughly suppressed under phase setting B. Red curve: Synchronized phase setting A, no analog signal modulation. Blue curve: Phase setting B, 50-GHz analog signal modulation..	53
Figure 3.16 Experimental spectra of PS multicasting with each input signal power of -12 dBm, where the fully eliminated HoFWM tone has 22-dB suppression ratio, but in limited bandwidth. Red curve: PS spectrum with phase setting A. Blue curve: PS spectrum with phase setting B.	54

Figure 3.17 Tunability of HoFWM suppression from 1533 to 1568 nm. Red curves: PS spectra with phase setting A. Blue curves: the signals' phases are optimized to maintain G/CEs and suppress HoFWM for different wavelengths.	56
Figure 3.18 Simulated gain and NF evolution in the single stage fiber mixer.	58
Figure 3.19 (a) G/CE comparison between the 4MPS and PI wavelength multicasting. (b) NF comparison.	60
Figure 3.20 Experimental architecture of characterizing BER performance. (a) PS/PI parametric mixer. (b) EDFA benchmark.	62
Figure 3.21 BER performance comparisons between the 4MPS and PI wavelength multicasting over eight multicasted signal copies from 1543.7 to 1559.7 nm.	63
Figure 4.1 The simulated configuration in NLSE solver. P_1 , P_2 : two pumps, S_1 to S_4 : four signals, AM: amplitude modulator, PM: phase modulator, HNLF: highly nonlinear fiber, SMF: single mode fiber. subset (a) Spectral overview of pump and signal seedings in phase insensitive multicasting. subset.	69
Figure 4.2 Power transfer characteristics between output and input signals, as well as pump depletion versus input signal power. (a) Power transfer curve for PS scheme. (b) Power transfer curves for PI case.	71
Figure 4.3 (a) Simulated spectra of parametric mixer based wavelength multicasting under 4MPS (red curve) and PI (blue curve) operation modes. (b) Expanded spectral comparison.	72
Figure 4.4 Experimental architecture for all-optical multicaster and regenerator, consisting of five parts: Creation of pump/signal seedings, Pump recovery, signal processing, parametric mixer, and DPLL. LD: laser diode, AM: amplitude modulator, PM: phase modulator, PS: phase shifter.	75
Figure 4.5 Experimental power transfer function of parametric wavelength multicasting under 4MPS (a) and PI (b) modes, as well as the pump depletion versus the input signal power.	76
Figure 4.6 Experimental spectra of 4MPS multicaster under saturated operation mode. (a) entire spectrum. (b) expanded spectrum for central 20 replicas.	77
Figure 4.7 Experimental configuration for AN regeneration.	78
Figure 4.8 (a) BER curves for BTB with and without the artificial AN source, and the central 20 multicasting signal copies. (b) Q factor and eye diagram comparison between the multicasting output and input at the receiver sensitivity of -35 dBm. Q factor spectra for input BTB condition.	79

Figure 4.9 Experimental configuration for 4MPS multicaster as a phase noise regenerator.....	80
Figure 4.10 (a) The BTB BER curves without and with PN are shown in black dashed and solid curves, respectively. The colorful solid curves represent the BER curves of the central 20 signal copies, characterizing the 4MPS multicaster performance as a phase regenerator, where the phase error amounted to $\pm 50^\circ$	81
Figure 4.11 (a) The BTB BER curves without and with PN are shown in black dashed and solid curves, respectively. The colorful solid curves represent the BER curves of the selected eight signal copies, characterizing the 4MPS multicaster performance as a phase regenerator.....	82
Figure 4.12 (a) The BTB BER curves without and with PN are shown in black dashed and solid curves, respectively. The colorful solid curves represent the BER curves of the selected eight signal copies, characterizing the 4MPS multicaster performance as a phase regenerator.....	83
Figure 5.1 (a) Dual-pump driven PI one-mode scheme. (b) Dual-pump driven 4MPS configuration. (c) Dual pump driven PS one-mode configuration. (d) Dual-pump driven PS three-mode configuration. (e) PS one-mode scheme is equivalent to the dual pump driven two-mode case, as shown in (f).....	90
Figure 5.2 Gain and NF evolution diagrams for one- (a) and three-mode (b) PS wavelength multicasting in normally dispersive HNLF.....	92
Figure 5.3 Simulated spectral comparison between one- and three-mode PS multicasting. Red: three-mode. Blue: one-mode.....	94
Figure 5.4 Simulated spectra of one- and three-mode PS multicasting, with different phase arrangements. (a) PS one-mode spectrum with phase setting of $P_1/P_2/S_2$: 90/50/70. (b) PS three mode spectrum with phase setting of $P_1/P_2/S_1/S_2/S_3$: 90°/50°/70°/70°/70°.....	95
Figure 5.5 Phase dependent properties of one- and three-mode PS wavelength multicasting. (a) One-mode phase transfer characteristic. (b) Three-mode phase transfer characteristic.....	97
Figure 5.6 Experimental setup configuration, including reference comb, pump recovery, parametric mixer and DPLL. LD: laser diode, AM: amplitude modulator, PM: phase modulator, PS: phase shifter, OP: optical processor, SL: slave laser, PZT: piezoelectric transducer	97
Figure 5.7 Monitored optical spectra of reference comb (a) and multicasting output (b).	98

Figure 5.8 Experimental G/CE and NF comparisons over 5 replica copies between one- and three-mode multicasting. Blue dashed: one-mode G/CE. Blue solid: three-mode G/CE. Red dashed: one-mode NF. Red solid: three-mode NF..... 101

Figure 5.9 Simulated G/CE and NF comparisons over 5 replica copies between one- and three-mode multicasting. Blue dashed: one-mode G/CE. Blue solid: three-mode G/CE. Red dashed: one-mode NF. Red solid: three-mode NF..... 101

Figure 5.10 BER performance comparison between one- and three-mode wavelength multicasting. BTB is represented by the black solid curve. Dashed curves denote the one-mode wavelength multicasting over 1549.3, 1552.5 and 1555.7 nm. Solid colored curves shows the BER performance of the three-mode multicasting..... 103

LIST OF TABLES

Table 4.1 Simulated constellation comparison among input signal and output signals in the unsaturated and saturated operation.....	74
Table 4.2 Constellation comparison for the 4MPS multicasting output replicas at selected wavelengths.....	84

LIST OF ABBREVIATIONS

2HoFWM	Second high order four wave mixing
4MPS	Four-mode phase sensitive
ADC	Analog-to-digital converter
AM	Amplitude modulator
AN	Amplitude noise
ASE	Amplified spontaneous emission
AWG	Arbitrary waveform generator
BER	Bit-error-rate
BS	Bragg scattering
CE	Conversion efficiency
CW	Continuous wave
DAC	Digital-to-analog converter
DC	Direct current
DPLL	Digital phase-locked loop
EDFA	Erbium-doped fiber amplifier
ESA	Electrical spectrum analyzer
FOPA	Fiber optic parametric amplifier
FWM	Four wave mixing
G/CE	Gain and conversion efficiency
GVD	Group velocity dispersion
HNLF	Highly nonlinear fiber
HoFWM	High order four wave mixing
ICC	Inter-channel crosstalk
ICI	Inter-channel interference
MI	Modulation instability
MZM	Mach-Zehnder modulator
NF	Noise figure
NFoM	Nonlinear figure of merit
NRZ	Non-return-to-zero
OE/EO	Opto-electronic/electro-optic

OOK	On-off keying
OP	Optical processor
PC	Phase conjugation
PD	Photodetector
PI	Phase insensitive
PLL	Phase-locked loop
PM	Phase modulator
PS	Phase sensitive
PSD	Power spectral density
PZT	Piezoelectric transducer
QAM	Quadrature amplitude modulation
QPSK	Quadrature phase shifted keying
RF	Radio frequency
SBS	Stimulated Brillouin scattering
SMF	Single mode fiber
SNR	Signal to noise ratio
SOA	Semiconductor optical amplifier
SPM	Self phase modulation
WDM	Wavelength division multiplexing
WDMer	Wavelength division multiplexer
XPM	Cross phase modulation
ZDW	Zero dispersion wavelength

ACKNOWLEDGEMENTS

To me, this dissertation is not just a conclusion of the past work, but also a starting point for new life.

Five years ago, Professor Stojan Radic offered me a precious position in Photonics Systems Lab after a phone interview. Since then, I started a wonderful five-year journey, where I not only got technical training and did research with innovations, but also learned how to professionally write, communicate and collaborate. I am sincerely grateful for all the progress that I have achieved during this five-year academic exploration, as well as for all the people that have given me encouragements and supports.

First, I owe the biggest gratitude to my advisor Professor Stojan Radic. He is a dedicated researcher with great passion and faith in photonics, giving me substantial motivations into research work. In addition to his devotion, he is a rigorous scientist as well, leading to exceptional achievements for himself and plenty of meaningful research work for graduate students. Most prominently, his constant encouragements and supports in research and life endow me with great courage and confidence to face all the challenges in these five years. Besides, I would like to thank all my committee members: Professor Leonid Butov, Professor Miroslav Krstic, Professor Zhaowei Liu and Professor Shayan Mookherjea, for their constructive discussions and contributions into this dissertation.

During these five years, I work with a group of intelligent and hardworking people, to them I also owe my sincere gratitude. I started working with Dr. Sanja Zlatanovic, had a smooth transition because of her openness to discussion and sharing.

Subsequently, I participated in the project of photonics assisted analog-to-digital converter with Dr. Andreas O. J. Wiberg, gaining in-depth knowledge and experimental experience from him. Since then, we started our five-year long collaboration. After the summer of 2012, I started working on multi-mode phase-sensitive process for ultra-low noise wavelength multicasting, initiated by Dr. Zhi Tong, Dr. Bill P.-P. Kuo and Dr. Evgeny Myslivets. I must express my gratitude to all of them. Particularly, Dr. Zhi Tong, leading the project at that time, gave me enlightening instructions, whose exceptional work, experience, sharing and discussion made a foundation for this dissertation. Besides, I would like to thank Dr. Bill P.-P. Kuo not only for his in-depth guidance in this dissertation, but also for his selfless sharing and supports in these five years. Dr. Evgeny Myslivets is a versatile researcher, full of knowledge and experimental experience, to whom I must say thanks for his countless help in programming, manufacture and experiments. In addition to the technical skills and innovated research work, I also obtain good training in terms of writing and communication. In particular, Dr. Nikola Alic gave me the most help in academic writing and presentations, to whom I must express my sincere gratitude. Besides, I would want to thank Dr. Vahid Ataie for his inspiring discussions and countless help in the lab; to Daniel Esman and Eduardo Temprana for their sharing and collaboration in the experiments; finally, to all the girls in the lab, Ana Pejic and Faezeh Gholami, I think we are not just collaborative team members, but also good friends in life.

Besides the lab life, this five-year experience is also a story with friends and family. Here, I would like to express my sincere appreciations to the friends that have

given me help and supports, Dongjin Song, Jun Li, Enming Luo, Yu Xiang, and Yuncong Chen. A lot of friends have not been mentioned here, but I will always keep my sincere gratitude in heart to all of them.

Finally, I must thank my parents: father Kaiying Liu and mother Fugui Guo, for their thirty-year's selfless love and caring. Without their supports, I will achieve nothing. In China, there is an old saying that if a soldier gets a insignia for victory, the half of which belongs to his family. To me, the half of my PhD degree is my husband's, since his eternal supports and love give me courage and confidence to finish it.

Chapter 3, in part, is a reprint of the material as it appears in *Optics Express* in the article authored by Lan Liu, Zhi Tong, Andreas O. J. Wiberg, Bill P.-P. Kuo, Evgeny Myslivets, Nikola Alic and Stojan Radic, "Digital multi-channel stabilization of four mode phase sensitive parametric multicasting," vol. 22, no. 15, pp. 18379-18388 (2014). The dissertation author was the primary investigator and author/co-author of this article.

Chapter 3, in part, is a reprint of the material as it appears in *Journal of Lightwave Technology* in the article authored by Lan Liu, Andreas O. J. Wiberg, Evgeny Myslivets, Bill. P.-P. Kuo, Nikola Alic and Stojan Radic, "Suppression of inter-channel higher order four wave mixing in four-mode phase-sensitive parametric wavelength multicasting," vol. 33, No. 11, pp. 2324-2331 (2015). The dissertation author was the primary investigator and author/co-author of this article.

Chapter 3, in part, is a reprint of the material currently being prepared for submission for publication, contributed by Lan Liu, Zhi Tong, Andreas O. J. Wiberg,

Bill. P.-P. Kuo, Evgeny Myslivets, Nikola Alic and Stojan Radic, “Noiseless channel cloning using four-mode phase-sensitive parametric mixer” The dissertation author was the primary investigator and author/co-author of this article.

Chapter 4, in full, is a reprint of the material currently being prepared for submission for publication, contributed by Lan Liu, Eduardo Temprana, Vahid Ataie, Andreas O. J. Wiberg, Bill. P.-P. Kuo, Evgeny Myslivets, Nikola Alic and Stojan Radic, “All optical wavelength multicaster and regenerator based on four-mode phase-sensitive Parametric Mixer.” The dissertation author was the primary investigator and author/co-author of this article.

Chapter 5, in full, is a reprint of the material currently being prepared for submission for publication, contributed by Lan Liu, Andreas O. J. Wiberg, Bill. P.-P. Kuo, Evgeny Myslivets, Nikola Alic and Stojan Radic, “Comparison of one and three-mode phase sensitive wavelength multicasting.” The dissertation author was the primary investigator and author/co-author of this article.

VITA

2003-2007	B. S. in Electrical Engineering (Electronic and Information Engineering), Zhejiang University, China
2007-2010	M. S. in Electrical Engineering (Electronics Science and Technology), Zhejiang University, China
2010-2015	Ph.D. in Electrical Engineering (Photonics), University of California, San Diego

PUBLICATIONS

Journal Articles

1. **Lan Liu**, Eduardo Temprana, Vahid Ataie, Andreas O. J. Wiberg, Bill P.-P. Kuo, Evgeny Myslivets, Nikola Alic and Stojan Radic, "All optical wavelength multicaster and regenerator based on four-mode phase-sensitive parametric mixer," to be submitted
2. **Lan Liu**, Zhi Tong, Andreas O. J. Wiberg, Bill P.-P. Kuo, Evgeny Myslivets, Nikola Alic and Stojan Radic, "Noiseless Channel cloning using four-mode phase sensitive parametric mixer," to be submitted
3. **Lan Liu**, Eduardo Temprana, Vahid Ataie, Andreas O. J. Wiberg, Bill P.-P. Kuo, Evgeny Myslivets, Nikola Alic and Stojan Radic, "Comparison of one and three-mode phase-sensitive wavelength multicasting," to be submitted
4. Eduardo Temprana, Evgeny Myslivets, Bill P.-P. Kuo, **Lan Liu**, Vahid Ataie, Nikola Alic, and Stojan Radic, "Overcoming Kerr-induced information capacity limit in optical fiber transmission," submitted to *Science*
5. **Lan Liu**, Andreas O. J. Wiberg, Bill P.-P. Kuo, Evgeny Myslivets, Nikola Alic and Stojan Radic, "Suppression of inter-channel high order four wave mixing in four-mode phase-sensitive parametric wavelength multicasting," *Journal of lightwave technology*, vol. 33, no. 11, pp. 2324-2331, 2015
6. Vahid Ataie, Eduardo Temprana, **Lan Liu**, Evgeny Myslivets, Bill P.-P. Kuo, Nikola Alic and Stojan Radic, "Ultrahigh count coherent WDM channels transmission using optical parametric comb based frequency synthesizer," *Journal of lightwave technology*, vol. 33, no. 3, pp. 694-699, 2015
7. Abel Lorences-Riesgo, **Lan Liu**, Samuel L. I. Olsson, Rohit Malik, Ales Kumpera, Carl Lundstrom, Stojan Radic Magnus Karlsson and Peter A. Andrekson, "Quadrature

demultiplexing using a degenerate vector parametric amplifier,” *Opt. Express*, vol. 22, no. 24, pp. 29424-29434, 2014

8. **Lan Liu**, Zhi Tong, Andreas O. J. Wiberg, Bill P.-P. Kuo, Evgeny Myslivets, Nikola Alic, and Stojan Radic “Digital multi-channel stabilization of four-mode phase-sensitive parametric multicasting,” *Opt. Express*, vol. 22, no. 15, pp. 18379-18388, 2014
9. Andreas O. J. Wiberg, Daniel Esman, **Lan Liu**, J. R. Adelman, Sanja Zlatanovic, Vahid Ataie, Evgeny Myslivets, Bill P.-P. Kuo, Nikola Alic, E. W. Jacobs, and Stojan Radic, “Coherent filterless wideband microwave/millimeter-wave channelizer based on broadband parametric mixers,” *Journal of Lightwave technology*, vol. 2, no. 20, pp. 3609-3617, 2014
10. **Lan Liu**, Zhi Tong, Andreas O. J. Wiberg, Evgeny Myslivets, Nikola Alic and Stojan Radic, “Full characterization of self-phase-modulation based low-noise, cavity-less pulse source for photonic-assisted analog-to-digital conversion,” *Opt. Express*, vol. 20, no. 26, pp. B110-B117, 2012
11. Andreas O. J. Wiberg, **Lan Liu**, Zhi Tong, Evgeny Myslivets, Vahid Ataie, Bill P.-P. Kuo, Nikola Alic, and Stojan Radic, “Photonic preprocessor for analog-to-digital-converter using a cavity-less pulse source,” *Opt. Express*, vol. 20, no. 26, pp. B419-B427, 2012
12. Faezeh Gholami, Sanja Zlatanovic, Aleksandar Simic, **Lan Liu**, David Borlaug, Nikola Alic, Maziar P. Nezhad, Yeshaiahu Fainman, and Stojan Radic, “Third-order nonlinearity in silicon beyond 2350 nm,” *Appl. Phys. Lett.*, Vol. 99, 081102, 2011

Conference papers

1. **Lan Liu**, Eduardo Temprana, Vahid Ataie, Bill P.-P. Kuo, Evgeny Myslivets, Andreas O. J. Wiberg, Nikola Alic, and Stojan Radic, “The first demonstration of phase and amplitude regenerative multicasting by a four-mode phase-sensitive process,” *IEEE Photonics Conference (IPC)*, WB2.4, San Diego, CA, 2014.
2. **Lan Liu**, Eduardo Temprana, Vahid Ataie, Evgeny Myslivets, Bill P.-P. Kuo, Andreas O. J. Wiberg, Nikola Alic, and Stojan Radic, “Demonstration of enhanced amplitude regeneration in four-mode phase-sensitive parametric multicasting mixer,” *European Conference on Optical Communication (ECOC)*, Tu1.4.2, Cannes, France, 2014
3. Daniel J Esman, Andreas OJ Wiberg, Mu-Han Yang, **Lan Liu**, Bill P-P Kuo, Nikola Alic, and Stojan Radic, “Photonic parametric sampled analog-to-digital conversion at 100 GHz and 6 ENOBs,” *European Conference on Optical Communication (ECOC)*, Mo3.5.6, Cannes, France, 2014
4. Vahid Ataie, Eduardo Temprana, **Lan Liu**, Evgeny Myslivets, Bill P.-P. Kuo, Nikola Alic and Stojan Radic, “Flex-grid compatible ultra wide frequency comb source for 31.8 Tb/s coherent transmission of 1520 UDWDM channels,” *Optical Fiber Communication Conference (OFC)*, **Postdeadline** Th5B.7, San Francisco, CA, 2014

5. Andreas O. J. Wiberg, Daniel J. Esman, **Lan Liu**, Evgeny Myslivets, Nikola Alic, and Stojan Radic, "Photonic RF-channelized receiver based on wideband parametric mixers and coherent detection," *Conference on Lasers and Electro-Optics (CLEO)*, STu2I.6, San Jose, CA, 2014
6. Mu-Han Yang, Bill P.-P. Kuo, Stojan Radic, Faezeh Gholami, and **Lan Liu**, "40-GHz analog-to-digital converter based on sampling gate of silicon waveguide with ultra-low loss and high conversion efficiency," *Conference on Lasers and Electro-Optics (CLEO)*, SW3M.5, San Jose, CA, 2014
7. **Lan Liu**, Andreas O. J. Wiberg, Evgeny Myslivets, Bill P.-P. Kuo, Nikola Alic, and Stojan Radic, "Conversion efficiency and crosstalk optimization in four-mode phase-sensitive multicasting mixer by vectorial phase manipulation," *Optical Fiber Communication Conference (OFC)*, Tu2K.4, San Francisco, CA, 2014
8. Andreas O. J. Wiberg, Daniel J. Esman, **Lan Liu**, Vahid Ataie, Evgeny Myslivets, Bill P.-P. Kuo, Nikola Alic, Stojan Radic, Sanja Zlatanovic, J. R. Adleman, and E. W. Jacobs, "Agile wideband microwave/millimeter wave analysis by coherent filterless channelizer," *International Topical Meeting on Microwave Photonics (MWP)*, **Postdeadline**, Alexandria, VA, 2013
9. Zhi Tong, **Lan Liu**, and Stojan Radic, "Generation of low noise frequency replicas in parametric frequency combs via phase-sensitive process," *SPIE LASE*, invited talk 89640M, San Francisco, CA, 2014
10. **Lan Liu**, Zhi Tong, Andreas O. J. Wiberg, Evgeny Myslivets, Bill P.-P. Kuo, Nikola Alic and Stojan Radic, "Digital phase-locked loop-stabilized four-mode phase-sensitive parametric multicasting," *European Conference on Optical Communication (ECOC)*, We.3.A.4, London, UK, 2013
11. Andreas O.J. Wiberg, Daniel J. Esman, **Lan Liu**, Zhi Tong, Evgeny Myslivets, Nikola Alic, and Stojan Radic, "Demonstration of 74 GHz parametric optical sampled analog-to-digital conversion," *European Conference on Optical Communication (ECOC)*, Tu.1.C.1, London, UK, 2013
12. Zhi Tong, **Lan Liu**, and Stojan Radic, "Low-noise optical frequency multicasting using multi-mode phase-sensitive interaction," *IEEE Photonics Conference (IPC)*, invited talk, ThG1.1, Bellevue, WA, 2013
13. Zhi Tong, **Lan Liu**, Andreas O. J. Wiberg, Evgeny Myslivets, Bill P.-P. Kuo, Nikola Alic, and Stojan Radic, "First demonstration of four-mode phase-sensitive multicasting of optical Channel," *Conference on Lasers and Electro-Optics (CLEO)*, **Postdeadline** CTh5D.6, San Jose, CA, 2013
14. **Lan Liu**, Zhi Tong, Andreas O. J. Wiberg, Nikola Alic, and Stojan Radic, "Generation and characterization of self-phase-modulation based cavity-less pulse source," *Frontiers in Optics and Laser Science (FIO/LS)*, FW5D.2, Rochester, NY, 2012 (**BEST Student Paper Award**)
15. Zhi Tong, **Lan Liu**, Andreas O. J. Wiberg, Nikola Alic and Stojan Radic, "Self-phase-modulation based low-noise, cavity-less short pulse source for photonic-assisted

- ADC,” *European Conference on Optical Communication (ECOC)*, Th.1.F.5, Amsterdam, The Netherland, 2012
16. Andreas O. J. Wiberg, **Lan Liu**, Zhi Tong, Evgeny Myslivets, Vahid Ataie, Nikola Alic, and Stojan Radic, “Cavity-less pulse source based optical sampled ADC,” *European Conference on Optical Communication (ECOC)*, Mo.2.A.3, Amsterdam, The Netherland, 2012
 17. Bill P.-P. Kuo, Andreas O. J. Wiberg, **Lan Liu**, Nikola Alic, and Stojan Radic, “Self-linearization in analog parametric sampling gate using higher-order parametric mixing,” *European Conference on Optical Communication (ECOC)*, Th.1.F.2, Amsterdam, The Netherlands, 2012
 18. Vahid Ataie, Andreas O. J. Wiberg, **Lan Liu**, Nikola Alic, and Stojan Radic, “Parametric sampling gate linearization by pump intensity modulation,” *IEEE Photonics Conference (IPC)*, TuC5, Burlingame, CA, 2012
 19. Andreas O. J. Wiberg, Zhi Tong, **Lan Liu**, Joseph L. Ponsetto, Vahid Ataie, Evgeny Myslivets, Nikola Alic and Stojan Radic “Demonstration of 40 GHz analog-to-digital conversion using copy-and-sample-all parametric processing,” *Optical Fiber Communication Conference (OFC)*, OW3C.2, Los Angeles, CA, 2012
 20. Andreas O. J. Wiberg, Zhi Tong, **Lan Liu**, Joseph L. Ponsetto, Vahid Ataie, Evgeny Myslivets, Nikola Alic and Stojan Radic, “Demonstration of parallel polychromatic sampling based analog-to-digital conversion at 8 GS/s,” *Conference on Lasers and Electro-Optics (CLEO)*, CM2B.5, San Jose, CA, 2012
 21. Sanja Zlatanovic, Faezeh Gholami, Aleksandar Simic, **Lan Liu**, Nikola Alic, Maziar P. Nezhad, Yeshaiahu Fainman, and Stojan Radic, “Kerr nonlinearity in silicon Beyond 2.35 μ m,” *IEEE Photonics Society Summer Topical Meeting Series*, pp. 59-60, 2011

ABSTRACT OF THE DISSERTATION

Ultra-low noise wavelength multicasting
using multi-mode phase-sensitive parametric mixer

by

Lan Liu

Doctor of Philosophy in Electrical Engineering (Photonics)

University of California, San Diego, 2015

Professor Stojan Radic, Chair

Rapid advances in broadband services, such as streaming media, video conference, cloud computing and data center, challenge the traditional unicasting and broadcasting network structures. To address the demands of these commercial applications and consequently to increase the cost efficiency and flexibility of optical

networks, wavelength multicasting, creating spectrally distinct copies of a signal, has been developed. An ideal wavelength multicaster ought to replicate the signal with preserved integrity and signal to noise ratio (SNR) over a sizable copy number, which is essential to various applications, ranging from commercial to defense. However, most conventional technologies require that the output signal carriers be externally seeded in the multicasting process, and moreover, a majority of the self-seeded approaches are subject to a limited number of signal copies, each with degraded SNR. This is addressed in this dissertation, where we propose a new approach to achieve ultra-low noise wavelength multicasting through a multi-stage dispersion-managed fiber mixer operated in a multi-mode phase-sensitive (PS) architecture. Two operated gain regimes, namely the unsaturated and saturated, were theoretically and experimentally investigated here for the ultra-low noise wavelength multicasting.

The multi-mode PS parametric process constructively combines the coherent signal fields, in addition to the parametric effect induced nonlinear gain, leading to gain and conversion efficiency improvement. Having the PS process induced gain, the dispersion-managed fiber mixer with locally accumulated uncorrelated noise allows theoretically noiseless wavelength multicasting. In practical implementation, experimental characterizations on noise figure and bit-error-rate performance require the multi-mode PS parametric multicasting be operated in the unsaturated regime. Conversely, in phase encoded systems, the PS process inherently translates the phase noise into amplitude perturbations, while the resulting amplitude noise can be removed by the saturated parametric effect, leading to an all-optical amplitude and phase regenerative wavelength multicasting. The dissertation includes theoretical

analysis, experimental implementation, and reports record performances of the multi-mode phase-sensitive parametric wavelength multicasting.

Chapter 1 Introduction

1.1 Motivation

Telecommunication has been revolutionized in the information era. Telegraph has been substituted by the instant messaging. The continuously growing smart phone services have accelerated the development of broadband mobile technologies. In addition, television has evolved from a broadcaster into internet service on demand. All these traditional telecommunication industries have been given new vitality, meanwhile facing unprecedented challenges. The exponential growth of the internet traffic, in support of applications such as streaming multimedia, electronic commerce, and cloud computing, has induced a tremendous increase in demand of communication bandwidth. Since the 1970s, optical fiber has been commercially deployed as an optimal transmission medium for communication links and networks [1, 2], owing to its low loss and wide bandwidth. In particular, to fully utilize the fiber bandwidth and increase the transmission capacity and network flexibility, wavelength division multiplexing (WDM) technology, transmitting multiple distinct wavelengths in one fiber medium, becomes the mainstay for the optical transmission systems and networks [3, 4].

However, rapid advances in the streaming media, internet television, and video conference challenge the traditional network structures, such as point to point unicasting and broadcasting [5]. To address the demands of these commercial applications and consequently to increase the cost efficiency and flexibility of optical networks [6], a light-tree topology with multicasting-capable

routing node has been introduced [5, 7]. Ideally, multicasting, duplicating one incoming signal to multiple outputs, ought to possess low complexity and compatibility to WDM networks, in addition to preserve the integrity of the incoming signal over a sizable copy number.

The simplest approach to achieve multicasting is power-splitting [7], however, its frequency-degenerate nature violates the scalability and dynamic of the WDM networks. Even worse, the signal to noise ratio (SNR) of the multicasting output is inevitably degraded by the power splitting loss and the following amplification for the splitting loss compensation [7]. Conversely, nonlinear effects, such as self phase modulation (SPM) [8], cross phase modulation (XPM) [9], four wave mixing (FWM) [10, 11] and cross gain modulation [12], have been exploited to create spectrally distinct wavelength multicasting. However, most of these conventional approaches require the output signal carriers be externally seeded and moreover, a majority of the self-seeded methods [13-15] are subject to a limited number of channels, each with degraded SNR.

In contrast, the dual-pump self-seeded parametric process in a multi-stage, dispersion-engineered fiber mixer (i.e. shock wave mixer type [16, 17]) has been identified as an efficient method for wavelength multicasting, offering scalable high-count copy number and low noise performance [18]. In particular, the parametric mixer based wavelength multicasting has been employed in all-optical signal processing applications [19-21], and contributes substantially. For example, a coherent filterless microwave/millimeter-wave channelizer has been successfully demonstrated based on such parametric wavelength multicasting [19], presenting improved

sensitivity and dynamic range. The proposed parametric multicasting was also an essential component in the photonics assisted analog-to-digital converter (ADC) [20, 21]. Besides, a spectrally uniform frequency comb has been achieved by incorporating a nonlinear optical loop mirror into the parametric fiber mixer design [22], which was utilized for transmission of complex modulation formats over 1520 ultra dense WDM channels [23].

In addition to the capability of creating scalable high count copy number, the noise performance of the wavelength multicasting is of critical importance to various applications. Up to now, the lowest published noise figure (NF) of wavelength conversion is 3.7 dB [24], and even worse for the dual-pump driven parametric mixer based wavelength multicasting, there is a 6-dB quantum limit NF [25]. Here, we note that all the previous investigations were implemented based on phase insensitive (PI) process, implying that the conversion efficiency (CE) of the wavelength multicasting is not dependent on the phases of the input waves and the SNR is degraded by the noise coupling between distinct wavelengths. In contrast, phase sensitive (PS) parametric process has been validated as a potential method for noiseless amplification [26-28]. Particularly, a four-mode phase-sensitive (4MPS) architecture has been employed in the dual-pump driven parametric multicasting [29], presenting a 12-dB CE improvement due to the coherent field combination. In addition, the 4MPS parametric mixer operated in the saturated gain regime has the great potential to be a regenerative multicaster over a sizable copy number.

Inspired by all these unique properties of the 4MPS parametric wavelength multicasting, in addition to its critical importance to applications in commercial

industry and signal processing, this dissertation furthers the investigations on the dispersion-managed parametric mixer operated in the multi-mode PS architecture, in order to achieve the wavelength multicasting with ultra-low noise performance in both unsaturated and saturated gain regimes.

1.2 Dissertation overview

This dissertation investigates the ultra-low noise performance of the multi-mode PS parametric multicasting, including theoretical derivation, numerical simulation, experimental implementation and concluded discussion.

Starting from the basic physics of the parametric effects, Chapter 2 introduces the principle of the dispersion-managed fiber mixer. Mathematical derivation indicates the dispersion-governed nonlinear efficiency of the parametric mixer is proportional to the fiber length, nonlinear coefficient and optical power, leading to a specific design of the parametric mixer. In particular, the noise performance of the PI wavelength multicasting was numerically simulated and discussed in Chapter 2.

Relying on the efficient parametric wavelength multicasting, 4MPS architecture is proposed in order to obtain the ultra-low noise performance, as demonstrated in Chapter 3. The PS process is mathematically introduced, followed by the numerical simulations on the phase relation of the 4MPS parametric multicasting. Experimental demonstration is described subsequently, and particularly, phase manipulation for the stabilized operation and maximized gain and conversion efficiency (G/CE), as well as for reduced high order interference tones is detailed in Chapter 3. Following the stabilized implementation, the experimental characterization

of the ultra-low noise wavelength multicasting enabled by the proposed design is demonstrated.

The NF is defined as the ratio between the input and output SNRs in electrical domain with shot noise limited input. In practical implementations, the parametric mixer is operated in the unsaturated regime as a linear multicasting device for rigorous characterization on noise performance, as demonstrated in Chapter 3. In contrast, the implementation of all-optical regenerative multicaster requires the 4MPS parametric mixer be operated in the saturated gain regime, as described in Chapter 4. The phase-dependent amplification and the amplitude perturbation removal were numerically simulated, followed by the detailed experimental demonstrations, including amplitude and phase regeneration over 20 multicasting signal copies, a record performance for regenerative multicaster.

Chapter 5 furthers the discussion on the multi-mode PS parametric multicasting through comparing the PS one- and three-mode configurations. The comparison includes phase manipulation and noise performance. Numerical simulations and corresponding results are described for comparison, followed by the experimental characterizations on noise figure and bit-error-rate performance.

Finally, Chapter 6 summarizes this dissertation and discusses the future work.

Chapter 2 Phase insensitive parametric wavelength multicasting

Recognized by the wide conversion bandwidth, instantaneous response speed and full transparency to arbitrary modulation formats, parametric effect has been employed in various applications, such as amplification and wavelength conversion. This chapter describes the multi-stage dispersion-managed parametric mixer as an efficient method for wavelength multicasting with high count copy number.

Beginning with the introduction to the third-order nonlinearity induced nonlinear effects in the silica-based optical fiber, this chapter interprets the basic equations governing the parametric effect. The principle of the dispersion-synthesized parametric mixer is numerically demonstrated in Section 2.2. Subsequently, Section 2.3 discusses the quantum limit noise performance of the PI parametric wavelength multicasting by numerical simulations.

2.1 Third order nonlinearity

In the presence of light, the electron distribution of dielectric medium is displaced from the equilibrium position of the nuclei, resulting in dipole moment, i.e. polarization field. Consequently, the wave equation governing the electrical field propagating in the dielectric medium is expressed as [30]

$$\nabla \times \nabla \times E(r, t) = -\mu_0 \varepsilon_0 \frac{\partial^2 E(r, t)}{\partial t^2} - \mu_0 \frac{\partial^2 P(r, t)}{\partial t^2} \quad 2.1$$

here ε_0 is the vacuum permittivity, μ_0 is the vacuum permeability, and P is the induced electric polarization field (i.e. matter's response to light field [31]).

Owing to the strong inter-atomic electric field ($\sim 10^{10}$ V/m) [31], laser with high output power is required, in order to observe the nonlinear effects in the dielectric medium. On the other hand, when the incident light intensity is relatively weak compared to the inter-atomic field, the nonlinear polarization is negligible and the response of dielectric medium to the incident light in frequency domain can be expressed in linear form:

$$P(r, \omega) = \varepsilon_0 \chi^{(1)}(r, \omega) \cdot E(r, \omega) \quad 2.2$$

$\chi^{(1)}(r, \omega)$ is the first order susceptibility at position of r and frequency of ω . Correspondingly, the wave equation in the frequency domain is expressed as

$$\nabla^2 E(r, \omega) + \varepsilon_r(\omega) \frac{\omega^2}{c^2} E(r, \omega) = 0 \quad 2.3$$

Here, c is the speed of light in vacuum ($\mu_0 \varepsilon_0 = \frac{1}{c^2}$). The relative permittivity $\varepsilon_r(\omega) = 1 + \chi^{(1)}(r, \omega) = [n(\omega) + i\alpha(\omega)]^2$ is defined by the refractive index $n(\omega)$ and absorptive coefficient $\alpha(\omega)$. The $\alpha(\omega)$ is not considered in this dissertation, since the silica-based optical fiber has small loss coefficient. On the other hand, the refractive index $n(\omega)$ is inherently frequency dependent, leading to frequency dependent phase velocity $v(\omega) = \frac{c}{n(\omega)}$, namely chromatic dispersion. Correspondingly, the propagation constant $\beta(\omega) = n(\omega) \frac{\omega}{c}$ can be expanded as Taylor series at the reference frequency of ω_0

$$\beta(\omega) = \beta_0 + \beta_1(\omega - \omega_0) + \frac{1}{2}\beta_2(\omega - \omega_0)^2 + \frac{1}{6}\beta_3(\omega - \omega_0)^3 + \frac{1}{24}\beta_4(\omega - \omega_0)^4 \quad 2.4$$

β_0 is the propagation constant at ω_0 , while β_j is the j th order derivative of the propagation constant at ω_0 . Here, β_1 is the group delay, while $\beta_2 = \frac{d\beta_1}{d\omega}$ is the group

velocity dispersion (GVD). In practical terms, instead of β_2 , dispersion parameter D is usually utilized, defined as

$$D = \frac{d\beta_1}{d\lambda} = -\frac{2\pi c}{\lambda^2} \beta_2$$

Regarding single mode fiber (SMF), both β_2 and D are equal to zero around wavelength of 1300 nm, namely zero dispersion wavelength (ZDW), a critical parameter for the fiber.

In addition to the linear response, the interaction of the incident light with matter (e.g. fiber in this dissertation) is inherently a nonlinear process, inducing nonlinear polarization response. Take the SMF made of silica glass as an example, it does not exhibit second-order nonlinearity ($\chi^{(2)}$), due to the inversion symmetric molecule structure of SiO₂ [30]; however, its nonlinear polarization field is dominated by the third order nonlinearity (i.e. Kerr nonlinearity), expressed as

$$P_{NL}(r, \omega) = \varepsilon_0 \chi^{(3)}(\omega) E^3(r, \omega) \quad 2.5$$

Consequently, the wave propagation with the presence of nonlinear polarization is expressed as

$$\nabla^2 E(r, \omega) + [n(\omega) + n_2 I]^2 \frac{\omega^2}{c^2} E(\omega) = 0 \quad 2.6$$

where $n_2 = \frac{3}{8n} \text{Re}(\chi^{(3)})$ is the nonlinear index coefficient. Eq. 2.6 indicates that the refractive index is dependent on the light intensity. To solve Eq. 2.6 by the method of separation of variables, the electric field is defined as

$$E(r, t) = F(x, y) A(z) e^{i\beta z - i\omega t} \quad 2.7$$

where transversal mode distribution is represented by $F(x, y)$, $A(z) e^{-i\beta z}$ is the slowly varying longitudinal envelope function of the mode at frequency of ω , the main

quantity of interest for nonlinear optics. Solving Eq. 2.6, we can obtain the Nonlinear Schrödinger Equation (NLSE)

$$\frac{\partial A(z,t)}{\partial z} = i\widehat{D}A + i\gamma|A|^2A \quad 2.8$$

where $\widehat{D} = \sum_{k=0} (i)^k \frac{\beta_k}{k!} \frac{d^k}{dt^k}$ is the differential operator accounting for dispersion.

While the right second term is a nonlinear contribution, governing the nonlinear effects on the light propagation in the fiber, whose strength is determined by the nonlinear coefficient γ , in the unit of $\text{W}^{-1}\text{km}^{-1}$.

$$\gamma = \frac{n_2\omega}{cA_{eff}} \quad 2.9$$

where $A_{eff} = \frac{(\iint_{-\infty}^{\infty} |F(x,y)|^2 dx dy)^2}{\iint_{-\infty}^{\infty} |F(x,y)|^4 dx dy}$ is the effective mode area, determined by the

transversal mode profile $F(x,y)$. Owing to the smaller A_{eff} , highly nonlinear fiber (HNLF), possessing high nonlinear coefficient, is chosen as the main nonlinear platform for parametric multicasting in this dissertation.

2.2 Parametric amplification

The parametric effect is named for the nonlinear interaction involving no energy states change of the nonlinear medium. In other words, the parametric device is playing a passive role with refractive index modulated by the injected light. Consequently, the interacted optical waves should satisfy energy and momentum conservation. As aforementioned, owing to the high nonlinear coefficient and low loss, the investigated nonlinear platform in this dissertation is HNLF.

Eq. 2.8 in Section 2.1 governs the light propagation in the Kerr nonlinear medium, where the first right term represents the linear propagation of the optical field, and the nonlinear response is dominated by the second right term. Specifically, assuming in the presence of one incident optical field, the SPM induced by the power dependent refractive index of the fiber contributes phase rotation to the input optical field. In addition, the XPM emerges when more frequency-distinct fields are present in the fiber. While the most straightforward explanation for the FWM can be done with four optical fields, as shown in Fig. 2.1. Correspondingly, the total fields are represented by

$$E(r, t) = \sum_{k=1}^4 F_k(x, y) A_k(z, t) e^{i\beta_k z - i\omega_k t} \quad 2.10$$

where $\omega_1 < \omega_2 < \omega_3 < \omega_4$, and two frequency components (at ω_2, ω_3) with higher peaks are considered as non-degenerate pumps. Note that, we consider all the input optical fields as co-polarized, and the theoretical expressions are mathematically derived in scalar form.

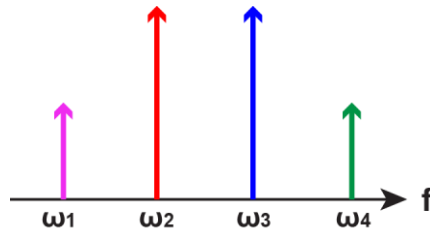


Figure 2.1 Frequency configuration of FWM.

We substitute Eq. 2. 10 into the NLSE of Eq. 2.8, and obtain

$$\begin{aligned}
\frac{dA_1}{dz} &= i\gamma[|A_1|^2 + 2(|A_2|^2 + |A_3|^2 + |A_4|^2)]A_1 \\
&\quad + i\gamma 2A_2A_3A_4^* \exp[-i(\beta_1 + \beta_4 - \beta_2 - \beta_3)z + i\Delta\omega t] \\
\frac{dA_2}{dz} &= i\gamma[|A_2|^2 + 2(|A_1|^2 + |A_3|^2 + |A_4|^2)]A_2 \\
&\quad + i\gamma 2A_1A_4A_3^* \exp[i(\beta_1 + \beta_4 - \beta_2 - \beta_3)z - i\Delta\omega t] \\
\frac{dA_3}{dz} &= i\gamma[|A_3|^2 + 2(|A_1|^2 + |A_2|^2 + |A_4|^2)]A_3 \\
&\quad + i\gamma 2A_1A_4A_2^* \exp[i(\beta_1 + \beta_4 - \beta_2 - \beta_3)z - i\Delta\omega t] \\
\frac{dA_4}{dz} &= i\gamma[|A_4|^2 + 2(|A_1|^2 + |A_2|^2 + |A_3|^2)]A_4 \\
&\quad + i\gamma 2A_2A_3A_1^* \exp[-i(\beta_1 + \beta_4 - \beta_2 - \beta_3)z + i\Delta\omega t]
\end{aligned} \tag{2.11}$$

where $\Delta\omega = \omega_1 + \omega_4 - \omega_2 - \omega_3$ is the frequency difference between the four fields. Specifically, the first four terms on the right side represent the SPM and XPM between the four input fields. The last term is the interaction of the FWM, whose efficiency is governed by the matching of the wave number, namely phase matching condition. Here, we can see that the four frequency components should satisfy $\omega_1 + \omega_4 = \omega_2 + \omega_3$, implying the conserved energy transfer between the input waves. In essence, parametric amplification absorbs two pump photons (from each pump wave at ω_2 and ω_3 , respectively), and transfers energy to one photon at lower frequency and creates a new photon at higher frequency through the nonlinear polarization mechanism (Eq. 2.5), as shown in Fig. 2.2. In this dissertation, the amplified input wave is named as signal, whereas the newly generated wave is idler.

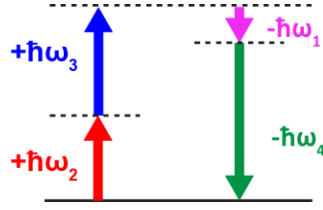


Figure 2.2 Energy diagram of FWM elastic process.

According to nonlinear polarization mechanism in Eq. 2.5, there are different possibilities for the third order generation. However, the FWM effect is inherently an elastic scattering process, requiring momentum equilibrium between the interacted waves, as indicated by the phase matching term $\Delta\beta = \beta_1 + \beta_4 - \beta_2 - \beta_3$. Particularly, in the fiber mixer, the nonlinear efficiency is governed by the dispersion profile of the fiber, and consequently, the phase matching term practically prevents the third order generation with high efficiency.

Regarding the solutions to the NLSEs in Eq. 2.11, the pump waves have much more intense power than the input signal, maintained undepleted and solved as

$$A_2(z) = A_3(z) = \sqrt{P_0} e^{i\gamma 3P_0 z} \quad 2.12$$

where P_0 is the input power of each pump and γ is the nonlinear coefficient of fiber. Eq. 2.12 indicates that the undepleted pumps are only subject to the nonlinear phase rotations. While the signal fields can be simplified as

$$\begin{aligned} \frac{dB_1}{dz} &= i\gamma 2P_0 B_4^* \exp[-i\gamma 2P_0 z - i\Delta\beta z] \\ \frac{dB_4}{dz} &= i\gamma 2P_0 B_1^* \exp[-i\gamma 2P_0 z - i\Delta\beta z] \end{aligned} \quad 2.13$$

where $B_1 = A_1 e^{-i4\gamma P_0 z}$, and $B_4 = A_4 e^{-i4\gamma P_0 z}$. Solving the coupled differential equation of Eq. 2.13, we can obtain

$$\begin{bmatrix} B_1(z) \\ B_4^*(z) \end{bmatrix} = \begin{bmatrix} \cosh gz + i \frac{\kappa}{2g} \sinh gz & i \frac{2\gamma P}{g} \sinh gz \\ -i \frac{2\gamma P}{g} \sinh gz & \cosh gz - i \frac{\kappa}{2g} \sinh gz \end{bmatrix} \begin{bmatrix} B_1(0) \\ B_4^*(0) \end{bmatrix} \quad 2.14$$

$g = \sqrt{4\gamma^2 P_0^2 - \left(\frac{\kappa}{2}\right)^2}$ is the exponential gain. Eq. 2.14 indicates that the amplification bandwidth and parametric gain are determined by the dispersion profile. To obtain the highest parametric gain, the phase matching term $\kappa = \gamma 2P_0 - \Delta\beta$ is demanded to be zero, where $\Delta\beta$ is approximated as $-\beta_2 \Delta\omega^2 - \frac{1}{12} \beta_4 \Delta\omega^4$, implying that the input waves should be selected in the anomalous dispersion region ($\beta_2 < 0$).

The frequency configuration in Fig. 2.1 is the most straightforward plot for the FWM interaction, i.e. parametric amplification. On the other hand, the energy conservation of the FWM effect allows different frequency combinations for the signals and pumps. In comparison to Fig. 2.1, the two pumps, one signal and one idler can be arranged differently, as shown in Fig. 2.3(c). Furthermore, Fig. 2.3 shows the category of the FWM effect, depending on the frequency configuration and input wave number. Fig. 2.3(a) shows the fully degenerate one-mode FWM process with pump and signal sharing the same frequency, and dual-pump one-mode FWM process, both of which are discussed in Chapter 5. Fig. 2.3(b) presents the degenerate single pump two-mode configuration, where the single pump contributes two photons in the nonlinear process, and additionally, the frequencies of the pump, signal and idler should satisfy the energy conservation: $\omega_s + \omega_i = 2\omega_p$. Historically, one-pump two-mode scheme, shown in Fig. 2.3(b), has been widely utilized for fiber optic parametric amplifier (FOPA) with wide amplification bandwidth and exponential gain. In next

section, we will focus on the dual-pump four-mode parametric effect, as shown in Fig.

2.3(d).

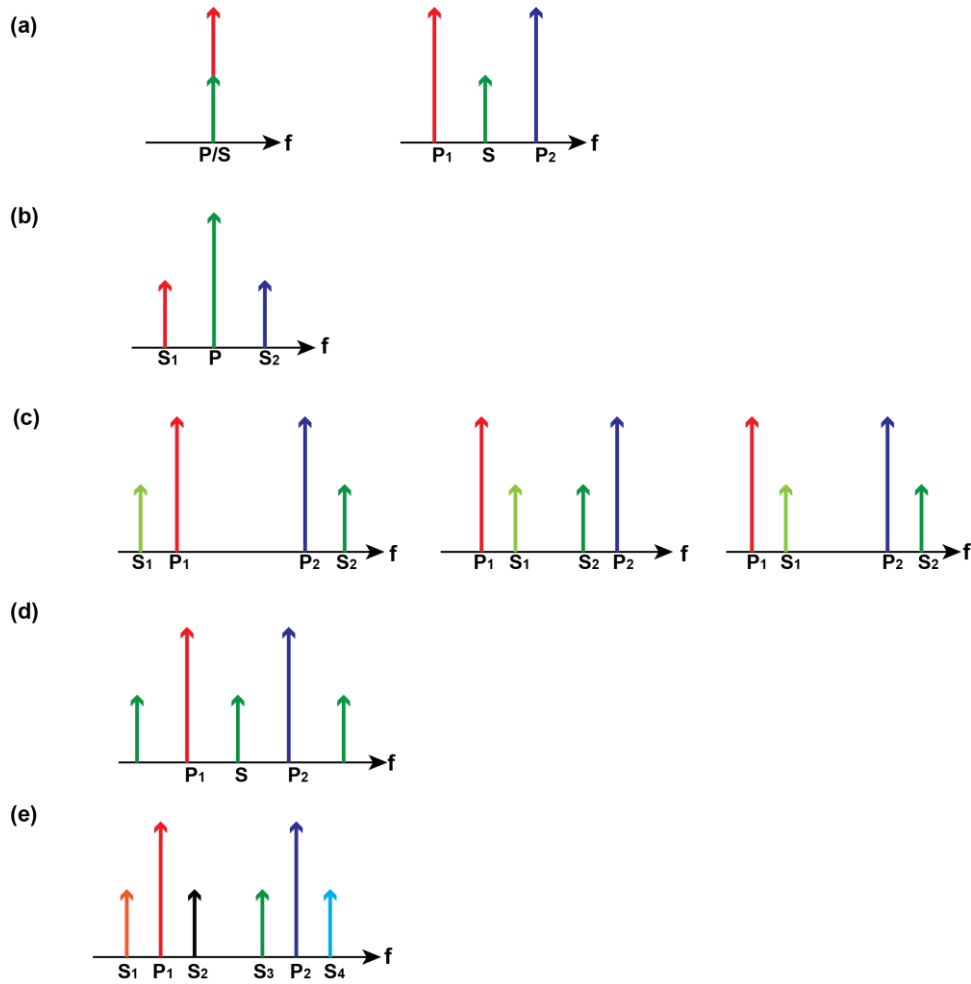


Figure 2.3 Frequency configurations of FWM effect. (a) fully degenerate and pump nondegenerate one-mode parametric effect. (b) One-pump two-mode parametric effect. (c) Two-pump two-mode parametric effect. (d) Two-pump three-mode parametric effect. (e) Two-pump four-mode parametric effect.

2.3 Parametric mixer

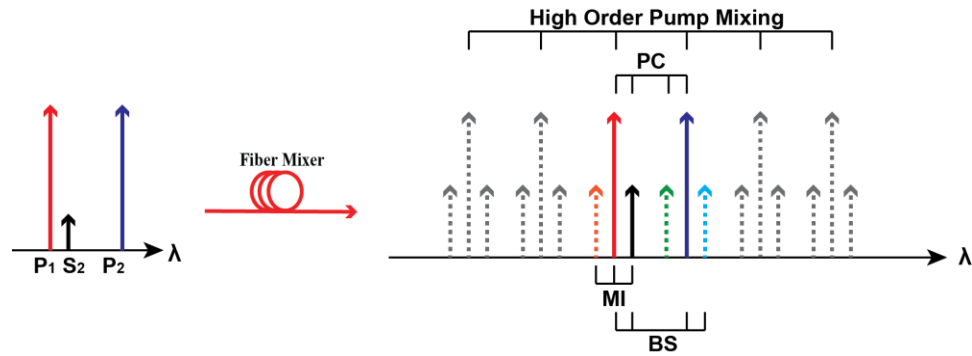


Figure 2.4 Fundamental principle for the dual-pump driven parametric wavelength multicasting.

Dual-pump seeded parametric mixer has been identified as an efficient method for wavelength multicasting with sizable number of signal copies [16, 17]. Fig. 2.4 shows the fundamental principle of the PI wavelength multicasting with two pumps and one signal at the input of the fiber mixer. Among the input three waves (i.e. signal frequency is offset from the middle of the two pumps), the nonlinear processes of modulation instability (MI), phase conjugation (PC) and Bragg scattering (BS) amplify the original input signal, and deliver three newly generated idlers [32]. Meanwhile, the refractive index of the nonlinear medium is modulated by the beating of the two pumps, inducing SPM and creating high order pumps. Consequently, cascaded FWMs multicast the input signal to spectrally distinct replica copies.

As mathematically derived in Eq. 2.14, the nonlinear efficiency of the parametric device is governed by the nonlinear figure of merit (NFoM), defined as the product of nonlinear coefficient, optical power and interaction length. In addition, the dispersion profile of the parametric device determines the phase matching condition, a prerequisite for efficient parametric effect. Recognizing these requirements, a

dispersion engineered fiber synthesized parametric mixer with sizable copy number has been developed in Ref. [16, 17] and is introduced numerically in this section.

Fig. 2.5(a) shows the simulation configuration of the dispersion-managed parametric mixer, which was calculated by a NLSE solver with adaptive step size, neglecting stimulated Brillouin scattering (SBS) and Raman interaction. In the simulation, two pumps were positioned at 1547.7 and 1550.9 nm, combined with one signal at 1550.1 nm and subsequently launched into the parametric mixer. Fig. 2.5(a) Inset shows the corresponding frequency configuration of the input three waves at checkpoint A. Specifically, each pump was initialized as having power of 0.6 W, while the signal possessed -20 dBm input power (P_{S0}). Quantum noise was modeled as an additive Gaussian white noise at the input of the mixer, with the variance defined by half-photon power spectral density (PSD).

The parametric mixer is constituted by three fibers. The first one is a 105-m HNLF (HNLF1), characterized by a ZDW of 1559 nm, dispersion slope (i.e. $\frac{dD}{d\lambda}$) of 0.025 ps/km/nm² and nonlinear coefficient of 15 km⁻¹W⁻¹, inducing SPM to the two pump defined sinusoid wave. Fig. 2.5(b) shows the frequency spectrum, time-domain waveform and chirp of the optical waves after HNLF1 (at checkpoint B). We can obviously observe that the SPM creates high order sidebands and the sinusoid waveform is positively chirped.

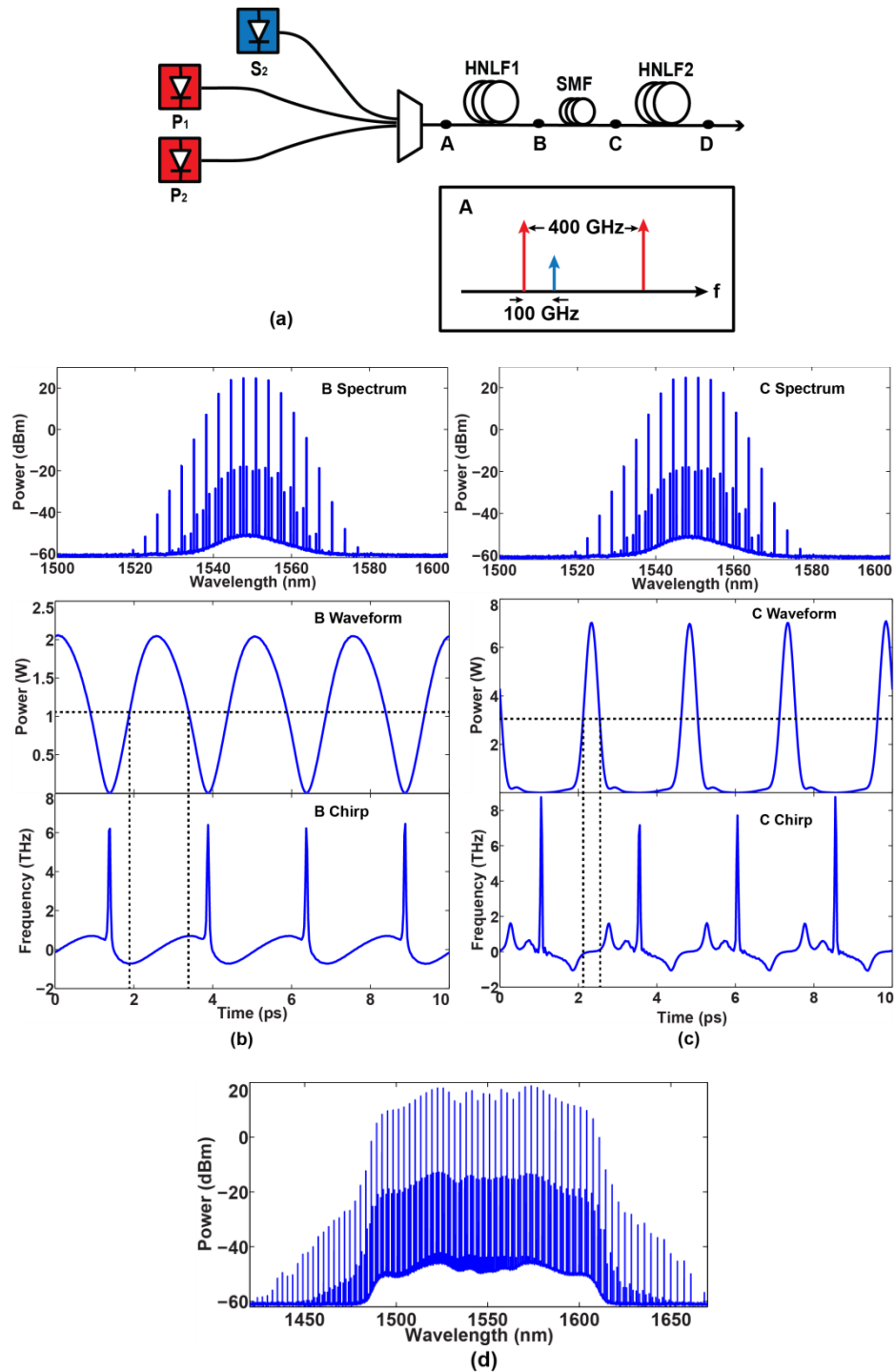


Figure 2.5 (a) Simulated configuration of parametric mixer, which is composed of three fiber stages. Inset: frequency configuration of input three waves: two pumps were spaced by 400 GHz, the input signal was 100-GHz offset from the pump at 1550.9 nm. (b) Optical spectrum, time domain waveform and chirp at checkpoint of B. (c) Optical spectrum, time domain waveform and chirp at checkpoint of C. (d) Optical spectrum at the output of the parametric mixer.

Subsequently, a 6-m SMF possessing negative GVD follows the chirping element, whose certain amount of dispersion compensates for the positive chirp, leading to narrow pulses in time domain. Correspondingly, the intensive pulses with negligible chirp are shown in Fig. 2.5(c) (for checkpoint C). In effect, the first two stages of the parametric mixer function as a pulse compressor, in order to obtain high peak power and high NFoM for the mixing stage. The final mixing stage is a 230-m dispersion flattened HNLF, characterized by a peak dispersion of -0.05 ps/nm/km and dispersion fluctuation less than 0.5 ps/nm/km over 100-nm bandwidth. Fig. 2.5(d) shows the simulated output spectrum of the parametric multicasting with over 100-nm bandwidth.

2.4 Noise analysis

The PI parametric multicasting is capable of generating high count copy number with preserved integrity, as introduced in Section 2.3. In addition, low noise operation is another essential property towards the ideal performance of wavelength multicasting. Therefore, we numerically investigate the noise performance of the proposed multi-stage parametric mixer in this section.

Noise property of optical devices is commonly evaluated by NF, defined as the ratio between the input and output SNRs in electrical domain [33] with a shot-noise limited input [34].

$$F = \frac{P_{in}/N_{in}}{P_{out}/N_{out}} \quad 2.15$$

The PI devices, including Erbium-doped fiber amplifier (EDFA), semiconductor optical amplifier (SOA), Raman amplifier, and FOPA, are widely

utilized in various applications, ranging from commercial to defense. However, all these PI amplifiers have NF quantum limits. Take the EDFA as an example, in addition to the amplified input noise, amplified spontaneous emission (ASE) are excited, resulting in excess noise and a quantum limit of 3-dB NF.

Regarding one-pump FOPA (shown in Fig. 2.3(b)) with one signal present at the input, the analytical solution can be simply denoted as

$$\begin{bmatrix} B_s(z) \\ B_i^*(z) \end{bmatrix} = \begin{bmatrix} u & v \\ v^* & u^* \end{bmatrix} \begin{bmatrix} E_{s0} + n_s \\ n_i^* \end{bmatrix} \quad 2.16$$

where u and v are determined by the phase matching condition and NFoM. Eq. 2.16 indicates that the parametric gain of the input signal is $G_{s,PIA} = \frac{P_s}{P_{s0}} = |u|^2$, while the CE of the idler is $G_{i,PIA} = \frac{P_i}{P_{s0}} = |v|^2$, further confirming the phase independent nature of the parametric amplification with the absence of the idler. The SNR is defined in the electrical domain with shot noise limited signal and correspondingly, the input SNR of one-pump FOPA can be expressed as

$$SNR_{in} = \frac{(\mathcal{R}P_{s0})^2}{4\mathcal{R}^2 P_{s0} \frac{h\nu}{2}} = \frac{P_{s0}}{2h\nu} \quad 2.17$$

where \mathcal{R} is the responsivity of the translation from optical to electrical domain, h is the Plank constant, and ν is the frequency of the detected signal. The noise term in Eq. 2.17 is dominated by the shot noise, resulting from the beating between the quantum noise source and the signal field (i.e. $P_{s0} \frac{h\nu}{2}$) [35]. While the output SNR is expressed as

$$SNR_{out} = \frac{(\mathcal{R}G_{s,PIA}P_{s0})^2}{4\mathcal{R}^2 G_{s,PIA}P_{s0} \left(G_{s,PIA} \frac{h\nu}{2} + G_{i,PIA} \frac{h\nu}{2} \right)} = \frac{P_{s0}}{4h\nu} \quad 2.18$$

where $G_{s,PIA}P_{s0}$ represents the amplified signal power. Eq. 2.18 also indicates that the parametric process couples the vacuum fluctuation from the idler to the signal mode, in addition to the amplified input noise, as denoted by $G_{s,PIA} \frac{h\nu}{2} + G_{i,PIA} \frac{h\nu}{2}$. Therefore, we can obtain $NF = \frac{1}{2}$, corresponding to 3-dB NF for the one-pump PI FOPA.

The same principle also works for the dual-pump driven FOPA, indicating that a quantum limit of 6-dB NF can be derived from the quantum noise coupling [36]. On the other hand, a parametric wavelength multicasting with high count copy number is desired in this dissertation, whose noise performance is intuitively considered as scaling up with copy number N [36, 37], expressed as

$$SNR_{out} = \frac{(\mathcal{R}G_{s,PIA}P_{s0})^2}{4\mathcal{R}^2 G_{s,PIA}P_{s0} \left(NG_{s,PIA} \frac{h\nu}{2}\right)} = \frac{P_{s0}}{N \cdot 2h\nu} \quad 2.19$$

Eq. 2.19 implies that the parametric multicasting with high count copy number is doomed to have degraded noise performance ($NF = \frac{1}{N}$), attributed to the equalized noise coupling among all the sidebands, provided that the fiber mixer has negligible dispersion. In practical terms, the normal dispersion profile of the parametric mixer is substantial to achieve efficient wavelength multicasting with ultra-low noise performance [25]. Consequently, numerical simulations on the noise performance of the parametric mixer were implemented by the NLSE solver, where two pumps and one signal were launched in to a single stage HNLF, characterized by a length of 600-m, a peak dispersion of -0.05 ps/km/nm and dispersion fluctuation less than 0.5 ps/nm/km over 100-nm bandwidth. The output spectrum of the PI multicasting in a single stage fiber mixer is shown in Fig. 2.6(a). Note that without the dispersion

management, the multicasting spectrum and copy number are largely reduced compared to the multi-stage parametric mixer in Fig. 2.5, further validating the high efficiency of the proposed dispersion-synthesized parametric mixer.

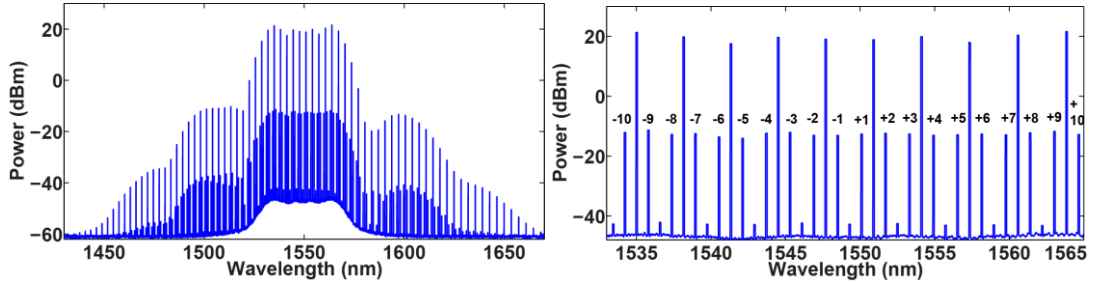


Figure 2.6 Simulated spectrum of wavelength multicasting in a single stage mixer. (a) whole spectrum. (b) expanded spectrum of central 20 signal copies.

To calculate the noise evolution in the single stage fiber mixer, the central 20 signal copies were individually derived from the comb and detected to obtain the noise PSD for the NF derivation. Fig. 2.7 shows the G/CE and NF evolution in the single stage fiber mixer, presenting a converged 6-dB G/CE for the central copies. In addition, we can observe that the NFs for the central 20 signal copies also converged to 6-dB, instead of scaling up with the copy number N . In effect, the noise coupling is localized due to the normal dispersion induced phase mismatch.

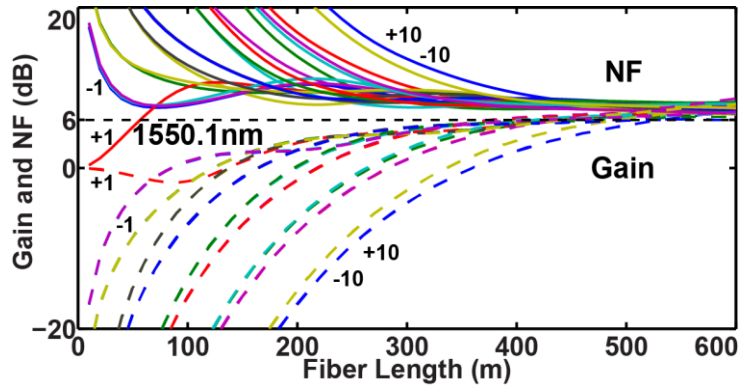


Figure 2.7 Gain and NF evolution in the 600-m long single stage fiber mixer.

Mathematically, the corresponding output SNR is expressed as

$$SNR_{out} = \frac{(\mathcal{R}G_{s,PIA}P_{s0})^2}{4\mathcal{R}^2G_{s,PIA}P_{s0}\left(4G_{s,PIA}\frac{h\nu}{2}\right)} = \frac{P_{s0}}{4\cdot 2h\nu} \quad 2.20$$

where $4G_{s,PIA}\frac{h\nu}{2}$ denotes the normally dispersive mixer induced localized noise coupling between the input waves, leading to a 6-dB NF quantum limit. Most importantly, with adequate interaction length and localized noise coupling, the wavelength multicasting with high count copy number but limited fidelity loss can be achieved by a properly designed normally dispersive fiber mixer.

2.5 Summary

In fiber communication, the parametric effect is usually treated as an impairing effect, inducing nonlinear crosstalk between the WDM channels. On the other hand, recognized by the instantaneous response speed and transparency to arbitrary modulation formats, the parametric effect has been employed in various applications, such as parametric amplification and signal processing [38]. In this dissertation, the multi-stage dispersion-managed parametric mixer was developed as an efficient method for wavelength multicasting with sizable copy number. Following the introduction to the basic physics of parametric effect, the principle of the parametric wavelength multicasting was described and numerically simulated.

Chapter 3 Four-mode Phase-Sensitive Wavelength multicasting

As demonstrated in Chapter 2, dual-pump driven parametric wavelength multicasting in normally dispersive mixer has a quantum limit NF of 6-dB, indicating a feasible high-count parametric multicaster with reasonable noise degradation. Contrary to the PI process, the PS parametric device has been acknowledged as the potential method for noiseless amplification. Therefore, we proposed to combine the 4MPS architecture with the dual-pump driven parametric mixer in this chapter, in order to the achieve the ultra-low noise wavelength multicasting.

Here, following the basic principle of the PS process in Section 3.1, the 4MPS wavelength multicasting is theoretically introduced in Section 3.2. Section 3.3 describes the experimental architecture, including coherent wave generation, pump recovery, fiber mixer, and phase-locked loop (PLL). While the essential component PLL is detailed in Section 3.4, illustrating the importance of manipulating the phases of two pumps for stabilization. Furthermore, to obtain the maximum G/CE profile and reduced high order four wave mixing (HoFWM) terms, the management on four signals' phases are demonstrated in Section 3.5 and 3.6, respectively. Subsequently, the experimental results, including NF and bit-error-rate (BER) evaluations, are presented in Section 3.7, validating the ultra-low noise performance of the 4MPS wavelength multicasting.

3.1 Phase sensitive process

According to the generalized amplifier uncertainty principle [39], the PI process, amplifying both quadratures of the input signal, has excess noise added during the amplification. Contrary to that, the PS amplification possesses phase dependent gain, considered as the potential means for noiseless amplification.

In practical terms, most reported experimental demonstrations of the PS devices were achieved by the parametric effects. As aforementioned in Section 2.2., this dissertation focuses on the HNLF (i.e. third-order nonlinearity) based PS parametric effect. The corresponding frequency configurations for one-mode, two-mode, three-mode and four-mode parametric effects are shown in Fig. 2.3. Take the one-pump two-mode FOPA (in Fig. 2.3(b)) as an example, there is a 3-dB quantum limit NF for the PI operation (with one signal present). On the other hand, when the phase correlated signal and idler both are present at the input of the parametric mixer, in addition to be coupled by the parametric process, constructive interference allows optical field coherent summations, resulting in a 6-dB gain improvement compared to the PI case. The principle has been demonstrated mathematically as

$$\begin{bmatrix} B_s(z) \\ B_i^*(z) \end{bmatrix} = \begin{bmatrix} u & v \\ v^* & u^* \end{bmatrix} \begin{bmatrix} E_{s0} + n_s \\ E_{i0}^* + n_i^* \end{bmatrix} \quad 3.1$$

where $E_{s0} = \sqrt{P_{s0}}e^{-j\theta_s}$, $E_{i0} = \sqrt{P_{i0}}e^{-j\theta_i}$, P_{s0} and P_{i0} are the initial input power for signal and idler, respectively. Solving Eq. 3.1, we can obtain the power of the signal and idler after amplification, expressed as

$$\begin{aligned}
P_s &= |u|^2 P_{s0} + |v|^2 P_{i0} + 2|uv|\sqrt{P_{s0}P_{i0}} \cos(\theta_s + \theta_i + \theta_u + \theta_v) \\
P_i &= |u|^2 P_{i0} + |v|^2 P_{s0} + 2|uv|\sqrt{P_{s0}P_{i0}} \cos(\theta_s + \theta_i + \theta_u + \theta_v)
\end{aligned}
\tag{3.2}$$

In the PI operation, the initial input power of the idler (P_{i0}) is zero, and therefore, we can obtain the PI gain is $G_{s,PIA} = \frac{P_s}{P_{s0}} = |u|^2$, while the idler CE is $G_{i,PIA} = \frac{P_i}{P_{s0}} = |v|^2$, further explaining the phase independent nature.

In contrast, when both the signal and idler are present at the input, Eq. 3.2 describes the phase dependent essence, i.e. the output powers of the signal and idler rely on the input phase relation $\theta_{rel} = \theta_s + \theta_i + \theta_u + \theta_v$. Specifically, $\theta_{rel} = 0^\circ$ leads to the constructive interference between the input waves, and therefore, we can obtain the maximum G/CE

$$\begin{aligned}
G_{s,PSA} &= \left(\frac{|u|\sqrt{P_{s0}} + |v|\sqrt{P_{i0}}}{\sqrt{P_{s0}}} \right)^2 \\
G_{i,PSA} &= \left(\frac{|u|\sqrt{P_{i0}} + |v|\sqrt{P_{s0}}}{\sqrt{P_{s0}}} \right)^2
\end{aligned}
\tag{3.3}$$

Assuming the input powers of the signal and idler are balanced, while the parametric gain is equalized, the output SNR can be obtained as

$$SNR_{out} = \frac{(\mathcal{R}G_{s,PSA}P_{s0})^2}{4\mathcal{R}^2G_{s,PSA}P_{s0}(2G_{i,PIA}\frac{h\nu}{2})} = \frac{P_{s0}}{4h\nu} \cdot \frac{G_{s,PSA}}{G_{i,PIA}} = \frac{P_{s0}}{h\nu}
\tag{3.4}$$

Owing to the coherent combination, the PS to PI gain improvement is four fold, corresponding to a 6-dB gain improvement. On the other hand, the incoherent noise coupling only doubles the noise power accumulation. Comparing the input (see Eq. 2.17) and output (see Eq. 3.4) SNRs, a -3-dB NF can be obtained for the two-mode FOPA. However, a more rigorous SNR definition relying on the combined powers of

the multiple input signal waves is utilized in this dissertation, where $SNR_{in,com} = \frac{(\mathcal{R}4P_{s0})^2}{4\mathcal{R}^24P_{s0}\frac{h\nu}{2}} = \frac{P_{s0}}{h\nu}$, leading to a theoretical 0-dB NF for the two-mode PS amplifier.

Therefore, the PS parametric process has the potential to achieve a truly noiseless amplification [39], motivating recent research efforts into this direction. Most of these studies have focused on one- and two-mode PS amplification, validating its phase squeezing [40-42] and low noise amplification [27, 28, 43] properties. Whereas, the investigation in this dissertation focuses on the 4MPS process, owing to its further improved SNR, which will be theoretically and experimentally demonstrated in next sections.

3.2 Four-mode phase sensitive multicasting

Fig. 3.1 shows the basic configuration of the dual-pump driven parametric wavelength multicasting in the PI and 4MPS operation modes. Conventional devices, mainly relying on the PI process, have phase-independent G/CE profiles, as shown in Fig. 3.1(a). Specifically, when S_3 is the only input signal, the processes of MI, BS and PC create new idlers, and meanwhile the cascaded FWM effects produce high order pumps and multicast signal replicas, as shown in Fig. 3.1(a). As discussed in Chapter 2, an ideal parametric mixer with normal dispersion localizes the noise coupling and converges the NF to 6 dB for the PI multicasting.

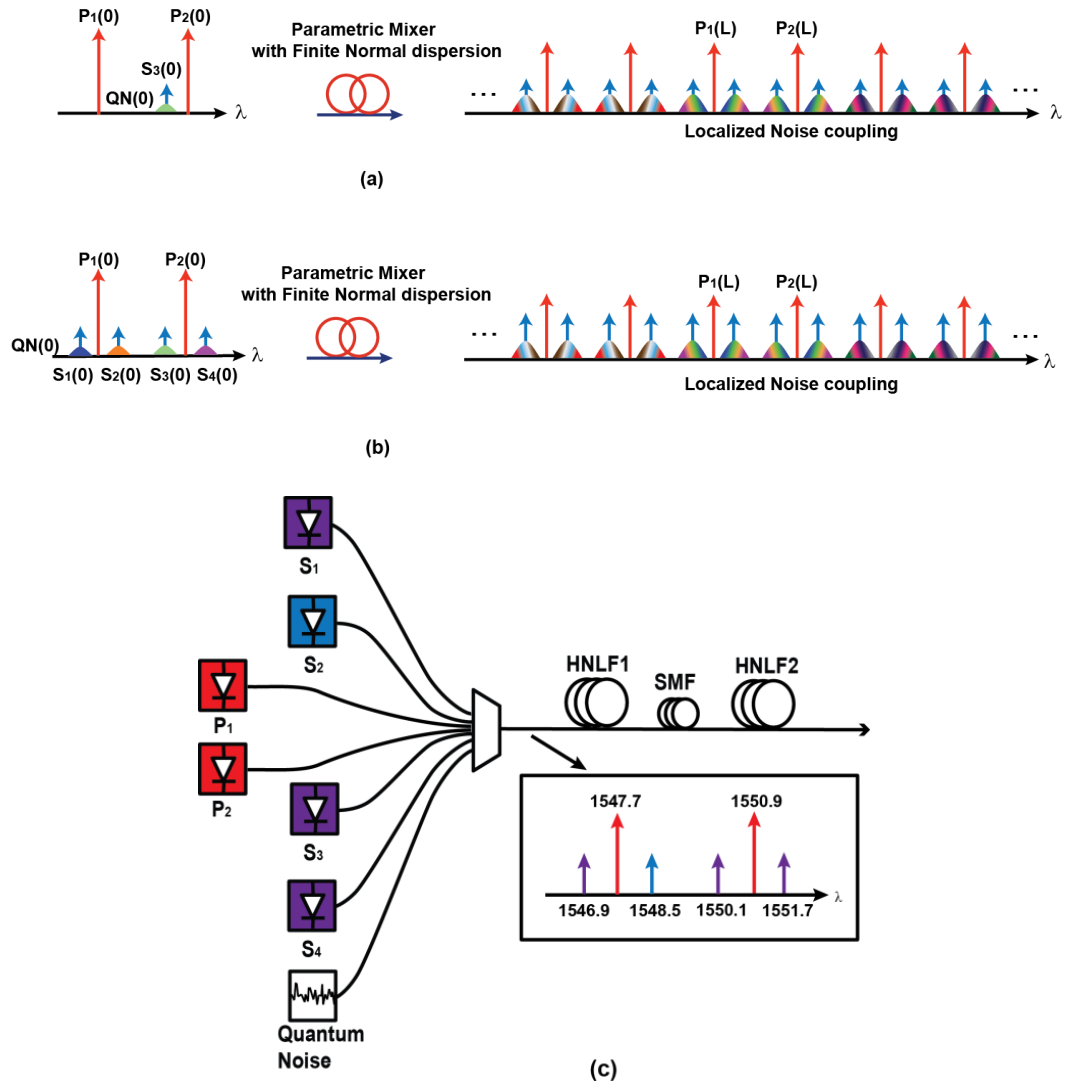


Figure 3.1 (a) The basic configuration for PI wavelength multicasting. (b) The basic configuration for PS wavelength multicasting. (c) The simulated configuration for 4MPS multicasting with two pumps and four signals launched into the three-stage parametric mixer.

In contrast, the 4MPS process corresponds to a state when all four sidebands ($S_1/S_2/S_3/S_4$) are occupied at the input, as shown in Fig. 3.1(b). Assuming that amplification process does not lead to significant pump depletion and high order mixing tone generation, one input mode (taking S_2 as an example) is amplified, while three remaining input modes contribute three idler fields to the amplified tone (S_2).

Consequently, the output mode at S_2 is the coherent summation of four fields, expressed as

$$S_{2_out} = \mu_1 S_1^* + \mu_2 S_2 + \mu_3 S_3^* + \mu_4 S_4 \quad 3.5$$

where S_{2_out} is the output mode, S_{1-4} are the input modes, and the coefficients μ_{1-4} are dictated by the characteristics of the parametric device and the input optical waves. Moreover, the parametric G/CEs are governed by the phase matching condition (assuming the dispersion, nonlinear coefficient and interaction length of the nonlinear medium, and optical powers have been optimized), as depicted in Eq. 3.5, where $\theta_{p1,p2}$ denote the pump phases, θ_{s1-s4} represent the signal phases, and m is an arbitrary integer.

$$\theta_{s1} = 2\theta_{p1} - \theta_{s2} + 2m\pi \quad 3.6(a)$$

$$\theta_{s3} = \theta_{p1} + \theta_{p2} - \theta_{s2} + 2m\pi \quad 3.6(b)$$

$$\theta_{s4} = \theta_{p2} + \theta_{s2} - \theta_{p1} + 2m\pi \quad 3.6(c)$$

Eq. 3.6 indicates that the maximum parametric G/CE mandates the phases of three signal modes match the phases of the remaining signal mode, as well as that of the two pumps. Provided that the phase conditions in Eq. 3.6 are satisfied, and the input signals' powers and parametric G/CEs on each mode are equalized, a 12-dB coherent gain increase (i.e. four-fold multiple of the single field) is expected when compared to the PI case. We note that this increase directly follows from Eq. 3.5, and was experimentally validated in Ref. [29, 44].

Regarding the parametric mixer based wavelength multicasting, it is not intuitive to analyze the phase relation between the interacted waves. Nevertheless, the response of the 4MPS multicasting architecture was calculated using an adaptive-step

NLSE model, neglecting SBS and Raman interaction. As demonstrated in Fig. 3.1(c), two pumps were positioned at 1547.7 and 1550.9 nm, and combined with four signals at 1546.9, 1548.5, 1550.1, and 1551.7 nm, respectively. Subsequently, the six phase-correlated waves were launched into the three-stage parametric mixer [16, 17], whose parameters have been detailed in Section 2.3. The power of each pump was 0.6 W, while the power of four signal modes were equalized; each mode possessing -20 dBm input power (P_{S0}). Quantum noise was modeled as an additive Gaussian white noise at the input of the mixer, with the variance defined by half-photon PSD. Here, we note that the simulation on the PI multicasting demonstrated in Section 2.3 has the same simulation setting, which, however, has only one input signal at 1550.1 nm. The G/CE of the multicasting is defined as a ratio between the output replica power and input signal power for both PS and PI schemes.

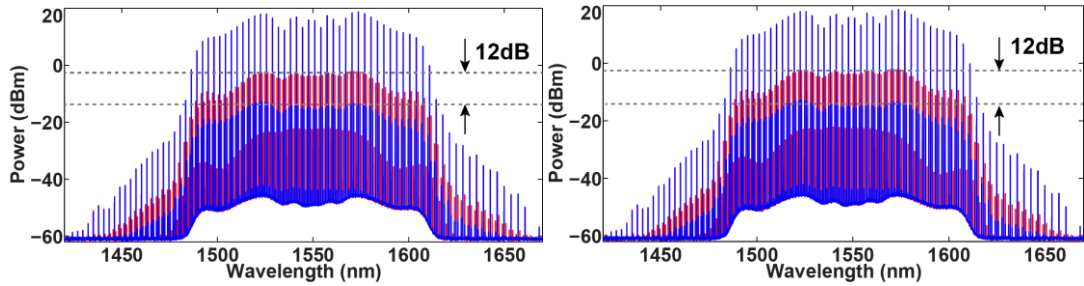


Figure 3.2 Spectral comparison between the 4MPS and PI wavelength multicasting. (a) The input six waves were phase synchronized as 0° . (b) The input six waves $P_1/P_2/S_1/S_2/S_3/S_4$ were arranged as $15^\circ/60^\circ/10^\circ/20^\circ/55^\circ/65^\circ$.

The resulting spectra from the simulated 4MPS parametric multicasting are shown in Fig. 3.2(a) and (b) as red curves, where the input optical waves were co-polarized. In Fig. 3.2(a), all the input waves were phase synchronized, i.e. the initial phases were 0° . Whereas in Fig. 3.2(b), the input phases of $P_1/P_2/S_1/S_2/S_3/S_4$ were arranged as $15^\circ/60^\circ/10^\circ/20^\circ/55^\circ/65^\circ$. Both states satisfy the phase matching condition

defined in Eq. 3.6, guaranteeing that the multicasting G/CE is maximized. Moreover, the blue curves in Fig. 3.2 correspond to the PI spectrum in Section 2.3, clearly validating that when the phase matching condition is satisfied, a 12-dB G/CE can be obtained by the 4MPS operation.

To investigate the phase dependent properties of the 4MPS wavelength multicasting, the phase of each signal was individually swept from 0° to 360° , while the phases of the remaining input waves were arranged according to the setting in Fig. 3.2(b). Based on the aforementioned multicasting G/CE definition, the PS G/CEs were calculated with each signal's phase swept. As expected, for the PI case, the G/CE was constant when the phase of the only input wave was swept. Consequently, the PS-to-PI G/CE improvements follow the same trend as the PS G/CE when the input phase is changed: with signal phase swept, corresponding response exhibits sinusoidal characteristics, as shown in Fig. 3.3. As an example, consider Fig. 3.3(a) in which S_1 's phase was swept, while the phases of $P_1/P_2/S_2/S_3/S_4$ were $15^\circ/60^\circ/20^\circ/55^\circ/65^\circ$. The corresponding PS-to-PI gain improvement peaks when the phase of S_1 is equal to 10° . In other words, a 12-dB G/CE PS improvement is obtained when the input phases obey the phase matching rule (i.e. Eq. 3.6). The same conclusion can be attained from sweeping the phase of the other inputs, as shown in Fig. 3.3: grey curves in Fig. 3.3 represent newly generated 20 signal copies. As evident, some of the grey curves deviate from optimum phase value, originating from the fact that the higher order mixing tones are dominated by FWM process that is spectrally distant from the original seeds. Recognizing the phase relations of the 4MPS multicasting, we next proceed to the experimental demonstrations with phase and power stabilizations.

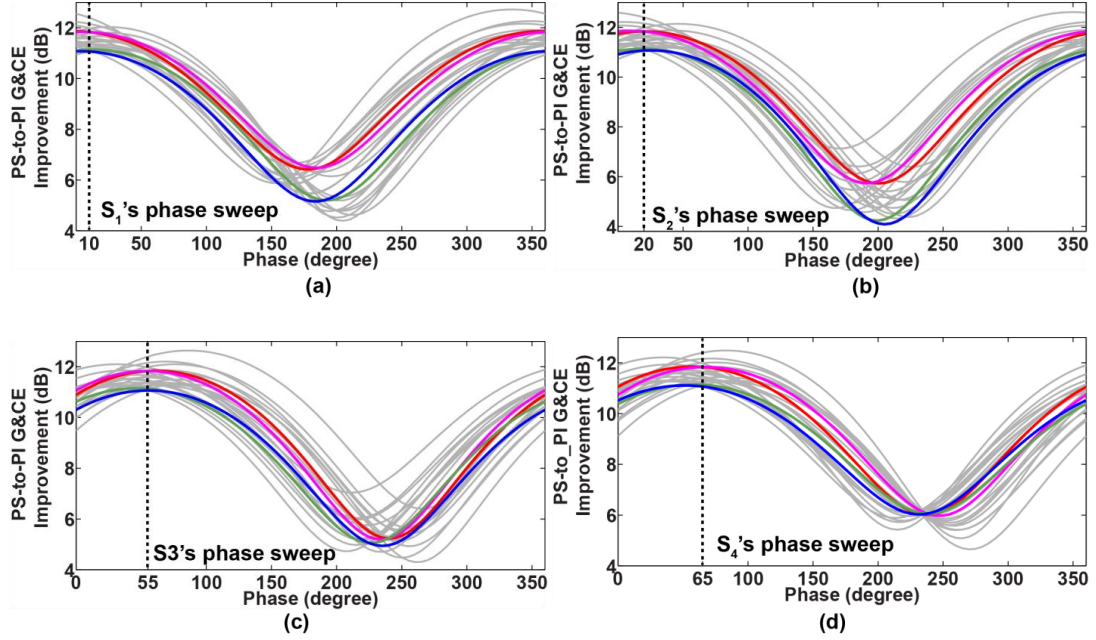


Figure 3.3 The simulated PS-to-PI G/CE improvements response of the central 24 signal copies for individual input (i.e. $S_1/S_2/S_3/S_4$) phase sweep. (a) phase of S_1 1546.9 nm was swept from 0° to 360° . (b) phase of S_2 1548.5 nm was swept from 0° to 360° . (c) phase of S_3 1550.1 nm was swept from 0° to 360° . (d) phase of S_4 1551.7 nm was swept from 0° to 360° . $S_1/S_2/S_3/S_4$ corresponding outputs are marked as blue, green, magenta and red.

3.3 Experimental implementation

We constructed the 4MPS experimental configuration as shown in Fig. 3.4(a), consisting of three distinct segments. In the first block, cascaded modulators were used to generate mutually coherent waves, essential for the phase correlation required in the PS process. A narrow linewidth laser centered at 1549.3 nm was launched into concatenated amplitude modulator (AM) and two phase modulators (PM), driven by a 25-GHz radio frequency (RF) signal. An optical comb with 5-nm 10-dB-bandwidth was generated by managing the bias of the AM and the RF phases into the PMs, with output spectrum shown in Fig. 3.4(b). EDFAs in Part I were used to compensate for the power degradation induced by the modulator cascade.

Next, the amplified comb was launched into second processing block, used to define the wavelength grid for pumps and signals, to regenerate pumps and finally to combine all polarization-aligned coherent waves before the parametric mixer. The two pumps were separated by 400 GHz and were positioned at 1547.7 and 1550.9 nm. Four signals were positioned with 100-GHz offset from the closest pump. Pump seeds and the signals were selected and de-multiplexed into three branches by an optical processor (OP). In each pump branch, injection locking was employed to maintain high SNR and guarantee high degree of phase correlation between the input waves. Subsequently, regenerated pumps were further amplified to 33 dBm, band-pass filtered and re-combined with the four signals at 1546.9, 1548.5, 1550.1 and 1551.7 nm. In the PI case, only one signal 1550.1-nm was extracted by the OP.

In the third block, all six coherent waves were launched into the three-stage dispersion-engineered parametric mixer [16, 17]. The first mixer stage consisted of a 105-m long high gamma HNLF (i.e. HNLF1 in Fig. 3.4(a)), characterized by a ZDW of 1597 nm, a dispersion slope of 0.018 ps/km/nm² and a nonlinear coefficient of 22 km⁻¹W⁻¹, which was longitudinally strained to increase the Brillouin threshold [45]. The nonlinear Kerr effects in HNLF1 induced a nonlinear phase shift (a positive chirp) and expanded the initial six tones. Note that the dispersion profile of the HNLF1 is presented in Fig. 3.4(c).

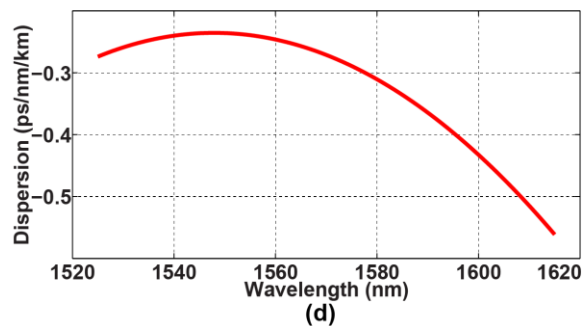
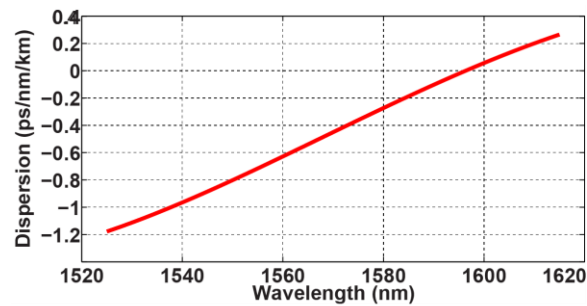
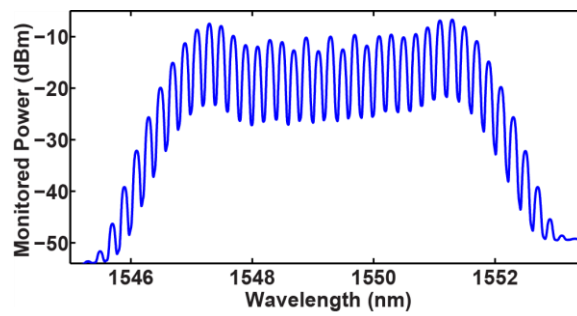
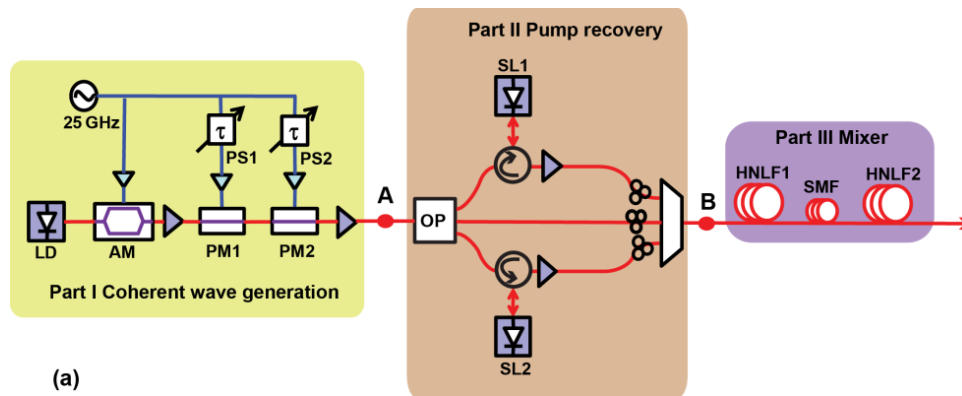


Figure 3.4 (a) Experimental configuration including four partitions: coherent wave generation, pump recovery, parametric mixer and DPLL. (b) Part I output, an optical comb with 5-nm 10-dB-bandwidth. (c) Dispersion profile of HNL F1. (d) Dispersion profile of HNL F2.

In the second mixer stage, the chirped tones were compressed in a 6-m SMF, resulting in optical pulses with high peak power in time domain. This was followed by a nonlinear stage, made of a 230-m long dispersion-flattened HNLF (see the dispersion profile of the HNLF2 in Fig. 3.4(d)), in order to further expand high-order tones and achieve broadband multicasting.

The proposed parametric mixer was capable of delivering hundreds of copies in the PI multicasting role, as validated in Ref. [16, 17, 29]. Provided that all environmental perturbations, such as thermal and acoustic fluctuations were absent, the PS operated processor chain was expected to provide a 12-dB G/CE and SNR improvement [29]. Unfortunately, the need for pump regeneration also renders this topology to be essentially an interferometer. In practice, thermal and acoustic variations induce length change in all three fiber branches of the second experimental block, resulting in fast (\sim kHz) fluctuations of the multicast output power. Consequently, a PLL is required to track and compensate for the phase fluctuations to maintain a relative constant phase relation between the six waves.

3.4 Phase-locked loop

Due to the inherent simplicity, most previous investigations focus on the one- and two-mode parametric devices, containing only one FWM process, as shown in Fig. 2.3(a) to (c). As a result, it is sufficient to phase-lock one pump's phase to signal(s) for stabilized output in these two cases, as validated in prior studies [28, 40, 41, 46]. In particular, the PLL in one- and two-mode applications can be implemented using simple, analog feedback algorithms.

In contrast, the phase relation of the dual-pump four-mode case, dominated by three FWM processes between the input six waves (MI, BS and PC), requires much more complex PLL schemes. Based on Eq. 3.6, different solutions for the PLL locking mechanism are admissible. In practical implementation, four signals are transmitted in a single waveguide and are phase locked to each other. The two pumps' phases can be manipulated independently to achieve stabilized operation. Specifically, P_1 can be controlled to be phase locked to S_1 and S_2 (see Eq. 3.6(a)), while P_2 is phase locked to P_1 , S_3 , and S_2 (see Eq. 3.6(b)). In this setting, the relative phase between the six waves are inherently maintained constant. In particular, to achieve maximum G/CE state, the phase of a signal wave should be optimized independently in order to satisfy the phase matching (i.e. S_4 in Eq. 3.6(c)). In a general case, four signals are not phase locked to each other and all the six waves possess independent phase fluctuations. In the latter setting, locking solutions, different from the one described above, would likely have to be judiciously selected.

As analyzed here, the phases of two pumps are required to be locked to maintain the constant phase relation, eliminating any simple PLL analog implementation with one dithering frequency tone from the consideration. Digital phase-locked loop (DPLL) techniques have been employed in various applications to track and maintain optical coherence [47, 48], since they allow advanced computing algorithm to be utilized in addition to the scaling of the controlled beam count.

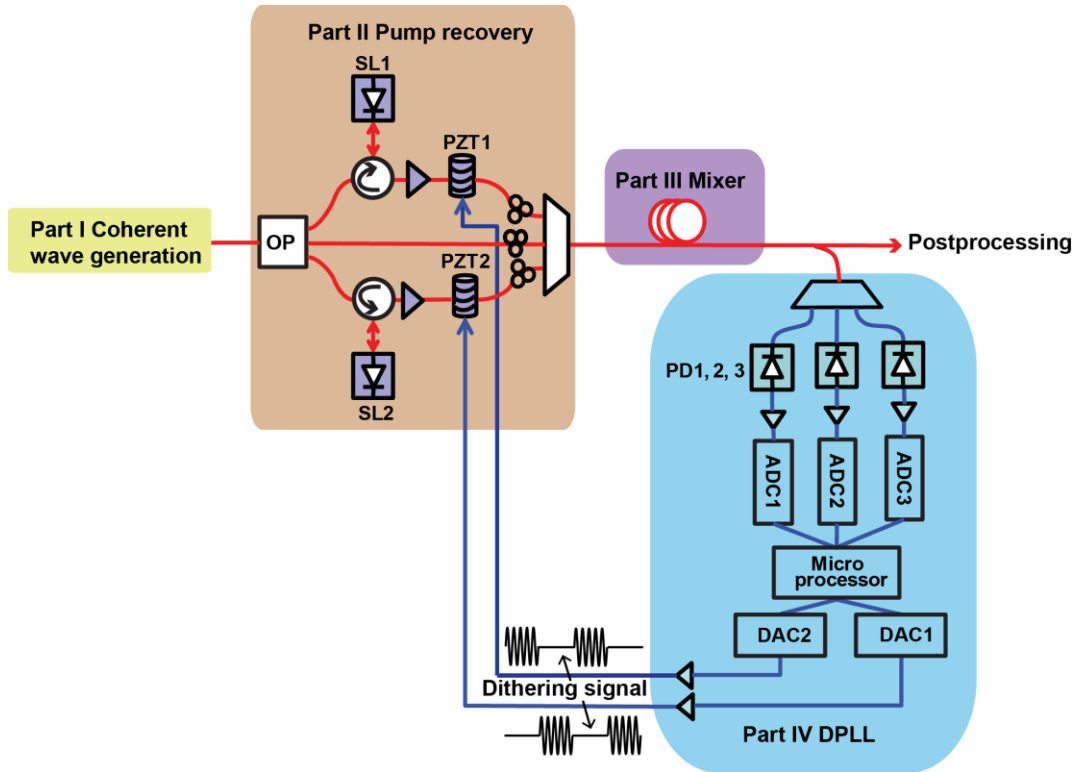


Figure 3.5 Experimental implementation with DPLL stabilization.

Consequently, we detail specific implementation of the DPLL scheme in Fig. 3.5, employed to maintain the stabilized G/CE in the 4MPS multicasting architecture. In this dissertation, the main function of the DPLL is to track the two pumps' phase fluctuations by a single dithering tone, compensate for the phase fluctuations of two pumps and maintain the relative phase relation between the three fiber branches. To obtain the error signal, the multicasting output from the architecture shown in Fig. 3.5 was split, and 10% of the power was received by the fourth processor section (i.e. DPLL). Instead of a PLL filter and a phase detector in the analog implementation, a microprocessor was utilized to calculate the phase error signals.

Furthermore, to track and lock the relative phase between the three independent fiber branches (of the pump recovery module), two piezoelectric

transducers (PZTs) were inserted into each pump path as stretching devices, while three fiber lengths were matched to within 1-cm physical difference. Two digital-to-analog converters (DACs) were used to output the phase error signals with alternating 60-kHz dithering, and subsequently electrically amplified to drive the PZTs. As a result, this phase dithering information was transferred to render 60-kHz power fluctuation of the multicasting output signals.

To achieve stabilized and equalized multicasting spectrum, three optical channels at 1548.5, 1550.1, and 1551.7 nm were filtered at the output monitor path, detected, electrically amplified and sampled by three ADCs. A dedicated microprocessor processed the sampled data in real time, inspected the phase-dithering induced power fluctuation, computed the error signal levels by the gradient descent algorithm [48, 49] and controlled the time sequence of the phase dithering of the two DACs. As indicated in Fig. 3.5, the phase dithering modulation on two pumps was time division multiplexed. Therefore, the microprocessor was capable of distinguishing phase fluctuations from each pump, a critical functionality in this architecture.

The instantaneous response of the DPLL was recorded by monitoring three channels at 1548.5, 1550.1, and 1551.7 nm, as shown in Fig. 3.6(a). Prior to the DPLL initiation (0 ms), multicasting output powers fluctuated due to the environmental perturbations. 800 ms after DPLL initiation, the digital stabilization algorithm has converged and the system has locked the loop. As seen in Fig. 3.6(a), the power fluctuations are reduced after this period and the output powers are maximized and maintained at a steady level. Note that the DPLL locking bandwidth is 3 kHz, mainly

determined by dithering frequency and error-signal extraction algorithm execution speed in the microprocessor. Fig. 3.6(b) illustrates the direct current (DC) coupled driving signals applied to two PZTs, derived from the error-signals computed by the microprocessor. In practical terms, both PZTs were digitally managed in real time to alter the two pumps phases and to compensate for environment-induced phase fluctuations, imposing a strict and stationary phase relation between the input waves.

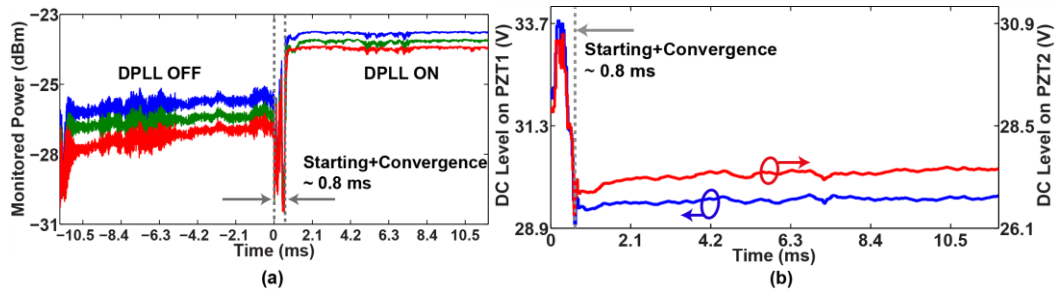


Figure 3.6 DPLL instantaneous performance. (a) Three monitored optical channels' power fluctuations. (b) The DC driving signals on two PZTs.

Finally, the requirement that the DPLL operates with three simultaneously monitored channels is validated in Fig. 3.7. As illustrated in Fig. 3.3, the high order mixing tones require a specific, optimal signal phase, different from the original seedings. In this condition, only localized maximized PS CE can be attained, whereas other multicasting copies will be attenuated. For broadband multicasting, the G/CE must be globally optimized, and thus three wavelength channels (i.e. 1548.5, 1550.1 and 1551.7 nm) were monitored for equalized spectrum, shown as the red curve in Fig. 3.7, which possessed 1.5-dB flatness over 20 signal copies. When one or two of three channels were selected for phase locking, tilted G/CE spectra were obtained and presented as the blue and black curves in Fig. 3.7, respectively. Therefore, Fig. 3.7 confirms that the globally equalized maximum G/CE spectrum mandates at least three

monitored channels in the DPLL system. In contrast, only one or two monitored channels were sufficient for stabilization, but the CE will then deviate from copy to copy and will not yield equalized spectral response.

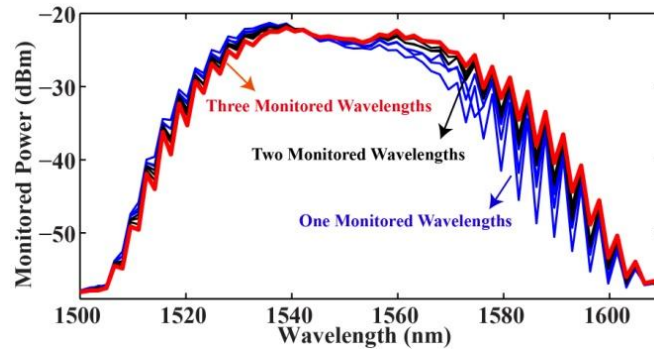


Figure 3.7 The signal power spectra with one, two and three monitored channels. Red curve: three monitored channels, blue curves: two monitored channels, black curves: one monitored channel.

3.5 Phase manipulation

According to the predictions and simulations in Section 3.2, one of the input signals' phase also needs to be controlled to obtain the maximum multicasting G/CE, in addition to two-pump phase locking. Consequently, multicasting can be optimized by sweeping the phases of the four input signals individually. According to the G/CE definition in Section 3.2, the PS G/CEs were calculated when the power of each input signal was -18 dBm and each signal's phase was swept over 360° by the OP, while the PI G/CE was obtained for the input signal of 1550.1-nm with power of -18 dBm. Experimental comparison between PS-to-PI G/CE for phase sweeping of individual input signal is presented in Fig. 3.8(a) to (d), respectively, where a 12-dB G/CE improvement was clearly seen between the PS and PI scheme. Finally, the 12-dB PS

induced gain increase over that in the PI case was observed by optimizing the input phase of any one among the four signals.

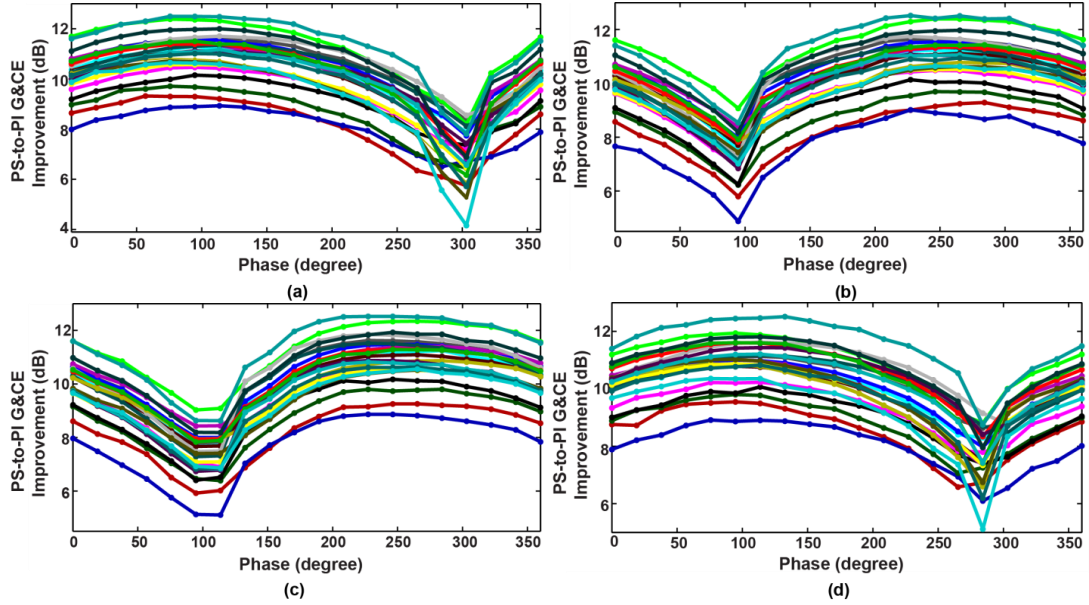


Figure 3.8 Experimental multicasting (i.e. central 24 copies) output power response by changing signal phase. (a) S_1 1546.9 nm phase is swept over 360° . (b) S_2 1548.5 nm phase is swept over 360° . (c) S_3 1550.1 nm phase is swept over 360° . (d) S_4 1551.7 nm phase is swept over 360° .

The measurements can be compared with the simulated responses shown in Fig. 3.2, where phase sweep induced difference of the PS-to-PI coherent gain was more than 6 dB. However, experimental PS-to-PI coherent gain increase was approximately 3 dB, as shown in Fig. 3.8. This discrepancy is a direct consequence of the developed DPLL algorithm that optimized the phases of the two pumps to maximize and stabilize multicasting G/CE when the signal phase was tuned; in contrast, in simulations only one signal phase in the system was tuned and all the other input phases were fixed. However, the measured improvement of PS-induced G/CE in Fig. 3.8 still illustrates that at least one signal phase should be used for optimization of multicasting G/CE. Note that in the signal phase control, the DPLL served a dual

functionality: the DPLL first controlled the relative phase between the pumps and the signals for a maximized multicasting G/CE; additionally the DPLL maintained the relative phase relation between the six waves by compensating for the phase fluctuations in each pump path.

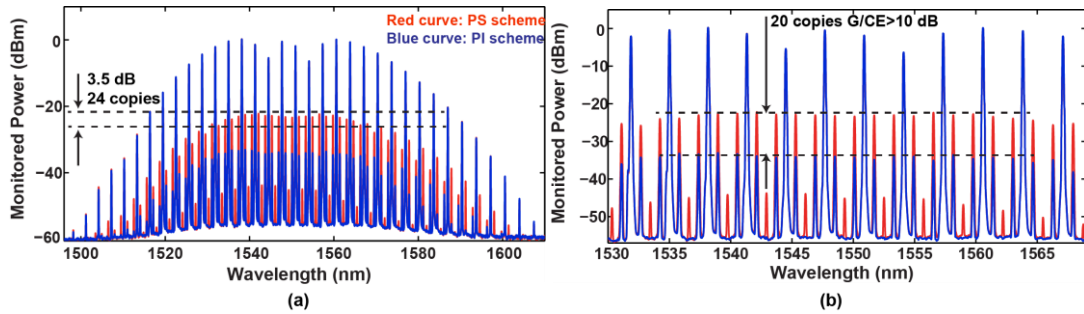


Figure 3.9 Experimental spectra comparison between the PS and the PI multicasting. (a) whole spectrum. (b) a zoom-in view.

The spectral response of the stabilized PS multicasting was compared with the PI scheme in Fig. 3.9(a), where one signal was set to the optimized phase value by the OP (e.g. signal 1546.9 nm, phase was manipulated to be 100°), leading to a maximized PS G/CE. The maximum G/CE of the PI multicasting was 5 dB for the input signal at 1550.1 nm having -18 dBm power level. In the PS multicasting case, using the same input power per mode as the PI case, a maximum of 12.5-dB CE improvement compared to the PI multicasting and 24 copies with 3.5-dB power flatness were achieved. A sub-band is shown in Fig. 3.9(b), indicating that the PS multicasting corresponding to 20-copy count had more than 10-dB gain advantage over the PI case. Equally important, the noise level remained at the same level as the PI condition. Consequently, a 12-dB optical SNR improvement over PI state in 4MPS multicasting was achieved in the case when two schemes had the same input signal power per mode (i.e. -18 dBm).

3.6 Suppression of high order four wave mixing tones

Due to the significantly improved CE of the 4MPS parametric multicasting, HoFWM effects between signals and pumps create spurious tones in the multicasting spectrum, leading to further beating between pumps or signals generating second high order four wave mixing (2HoFWM) crosstalk terms, directly degrading the multicaster performance, by virtue of inter-channel crosstalk (ICC). Various ICC suppression techniques have been investigated in WDM signal amplification based on a FOPA. In a one-pump driven FOPA, uneven frequency spacing or guard band [50, 51] has been deployed to isolate the crosstalk terms that originate from the FWM products between signals and idlers. Alternatively, it has been shown that reducing fiber length [52, 53] or nonlinearity [54] can effectively suppress HoFWM effects and thus its corresponding crosstalk. However, in those settings, the pump power needs to be increased to maintain the parametric efficiency and bandwidth. Compared to the single-pump FOPA, orthogonal pump polarization has been exploited in a dual-pump driven FOPA to reduce the FWM induced crosstalk, as well as signal degradation caused by cross gain modulation [55, 56]. Nevertheless, in the latter case the bandwidth occupied by the HoFWM tones in the wavelength multicasting still remains unusable. Even worse, for the high speed data multicasting and signal processing [19], the HoFWM terms can interfere with signal modulated sidebands and induce inter-channel interference (ICI).

The preceding sections have theoretically and experimentally demonstrated that pumps' phases and one signal's simultaneous regulation are pivotal to 4MPS multicasting power stabilization and CE maximization [41, 57]. While in this section,

the phases' manipulation of all the involved modes in the 4MPS multicasting is extended to HoFWM suppression [58, 59].

In the investigation, the wavelength multicasting is accomplished based on the dual-pump driven parametric processes in the three-stage, dispersion-synthesized shock wave mixer, whose input pump power, fiber length and nonlinearity are optimized specifically for low noise performance [18, 25], in addition to the broad bandwidth operation [16]. Moreover, in the chosen implementation, the two pumps are co-polarized in order to achieve broadband multicasting with maximized CE, making the conventional methods of suppressing HoFWM induced ICC and ICI in FOPA inapplicable. In this section, a novel scheme for removing inter-channel HoFWM tones based on 4MPS process is specifically demonstrated for the first time.

A spectral overview of dual-pump seeded parametric multicasting is shown in Fig. 3.10, where P_1 and P_2 are two pumps, and S_1 to S_4 are four signals. Due to the improved multicasting G/CE and thus the increased output power, the inter-channel HoFWM terms materialize. As shown in Fig. 3.10(a), H_1 (or H_2) is initially produced by the HoFWM between S_2 and P_1 (S_3 and P_2), and then cascaded FWM effects interact with H_1 (H_2) further, so as to generate other inter-channel HoFWM terms. However, the suppression of HoFWM effects can be engineered if the frequencies of pumps and signals are selected in the manner that H_1 and H_2 overlap, and their phases are manipulated so as to create destructive interference between H_1 and H_2 .

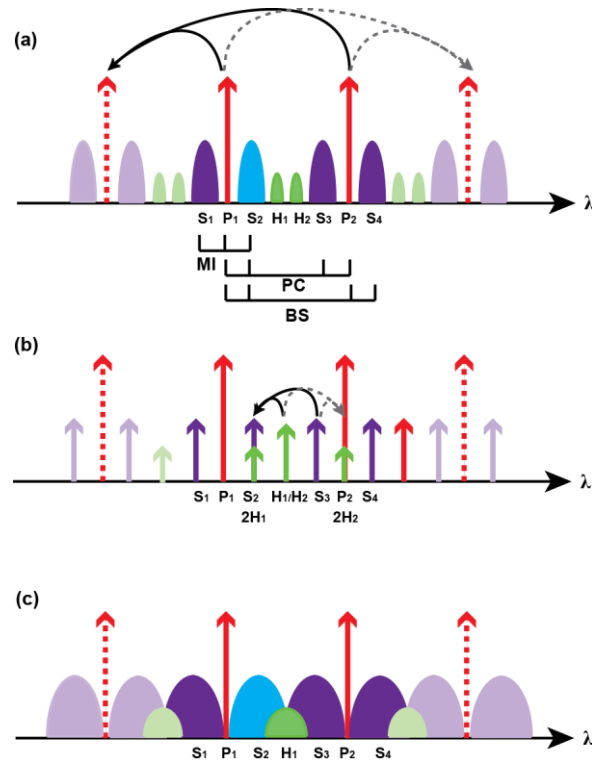


Figure 3.10 The schematic of dual-pump seeded parametric wavelength multicasting based on cascaded FWMs between pumps and signals. MI: modulation instability, PC: phase conjugation, BS: Bragg scattering. P_1, P_2 : pumps, S_1 to S_4 : signals, H_1 to H_2 : high order FWM tones. (b) ICC induced by the HoFWM tone. $2H_1$: FWM product from the second HoFWM between H_1 and S_3 . (c) ICI induced by the HoFWM tone.

On the contrary, constructive summation of H_1 and H_2 will increase the power of the central HoFWM tone, consequently boosting a 2HoFWM effect between H_1/H_2 and signals (or pumps). Take Fig. 3.10(b) as an example, assuming phase matching allows the FWM process to transfer energy from H_1/H_2 and S_3 to a 2HoFWM tone (i.e. $2H_1$), this generated tone will overlap with S_1 and inevitably result in ICC being introduced into the parametric multicasting. Certainly, when the input signal(s) contain high speed data and occupy a wide bandwidth, the generated HoFWM tone will interfere with the multicast replicas, inducing ICI and thus the degradation of the multicasting quality, as shown in Fig. 3.10(c).

3.6.1 Numerical simulation

The corresponding numerical simulations for the dual-pump driven parametric multicasting were implemented based on coupled wave equations, whose configuration and simulated parameters have been introduced in Section 3.2. As indicated in Eq. 3.7, N is the number of frequency lines that are present at the mixer output, z is the longitudinal position of the fiber mixer, γ is the nonlinear coefficient of fiber, A_i (A_j, A_k, A_l) is the optical field for each frequency line ω_i ($\omega_j, \omega_k, \omega_l$).

$$\begin{aligned} \frac{dA_i}{dz} = & i\gamma \left(|A_i|^2 + 2 \sum_{\substack{k=1 \\ i \neq k}}^N |A_k|^2 \right) A_i \\ & + 2i\gamma \sum_{\substack{\omega_i + \omega_k \\ = \omega_j + \omega_l}} A_j A_k^* A_l e^{\Delta\beta_{jki}} \\ & + i\gamma \sum_{\substack{2\omega_j \\ = \omega_i + \omega_k}} A_j^2 A_k^* e^{\Delta\beta_{jki}} \end{aligned} \quad 3.7$$

where $\Delta\beta_{jki} = (\beta_j + \beta_l - \beta_k - \beta_i)z$ is the phase matching term governed by the fiber dispersion. β_k is the propagation constant at frequency ω_k , which can be expanded around ZDW (i.e. ω_0), i.e. $\beta_k = \frac{1}{2}\beta_{k2}(\omega_k - \omega_0)^2 + \frac{1}{6}\beta_{k3}(\omega_k - \omega_0)^3 + \frac{1}{24}\beta_{k4}(\omega_k - \omega_0)^4$ [60]. Here, β_{k2} , β_{k3} and β_{k4} are the second, third and fourth order derivative of the propagation constant β_k at the ZDW, respectively.

In the simulation, A_{P1} and A_{P2} are the optical fields of the two pumps, whose initial average power and phase were 0.6 W and 0° , respectively. While the simulation-associated step size was set as 0.1 m. We note that there were 263 optical waves (including 66 pumps, 132 signals, and 65 inter-channel HoFWM tones)

interacting along the fiber mixer, where SBS, Raman interaction and noise statistics were neglected. The phase coherence between the input waves was guaranteed by managing each optical field as an ideal single frequency line. In contrast to our previous simulation work that studied the spectral comparison between the PI and PS scheme, as well as the noise evolution [25, 29] (see Section 3.2), in this contribution the investigation focuses on the phase manipulation of the 4MPS process employed for suppression of inter-channel HoFWM tones in the PS multicasting.

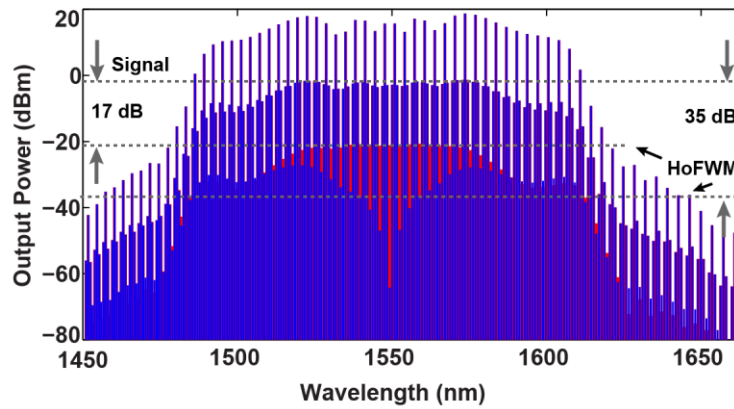


Figure 3.11 Simulated spectra of PS multicasting without and with HoFWM suppression. Red curve: for phase synchronized pumps and signals, there is no HoFWM suppression, signal to HoFWM tones extinction ratio is around 17 dB. Blue curve: for signals with complementary phase setting, signal to HoFWM tones extinction ratio is improved by over 20 dB.

The spectrum at the output of the simulated mixer with phase synchronized optical waves is shown as red curve in Fig. 3.11, where the four signals A_{S1} to A_{S4} were individually initialized with an average power of -20 dBm and phase of 0° . On the other hand, the blue curve in Fig. 3.11 shows the same signal G/CEs, but with reduced HoFWM terms, which was achieved by setting the phases of signals in a complementary manner, i.e. specifically, the phases of A_{S1} to A_{S4} were 45° , -45° , 45° , and -45° , respectively. As predicted in Section 3.2 [57, 58], both of these two phase arrangements (i.e. synchronized and complimentary) satisfy the phase matching

condition, leading to the same and maximized G/CE profiles in Fig. 3.11. Most importantly, however, as far as the objective of the present investigation, in terms of the HoFWM suppression, high extinction of the HoFWM was achieved when the signals' phases were managed in the complementary setting (see the blue curve in Fig. 3.11), and especially so for the central term at 1549.3 nm, where the signal to HoFWM extinction ratio was improved by more than 20 dB. Note that, the phase values for suppression of the central HoFWM tone was found by intensive simulations. Stemming from the phase matching requirement [23], a complimentary phase setting of $\pm 135^\circ$ reproduces the successful suppression in Fig. 3.11, with the pumps' phases set to 0° .

As implied by Eq. 3.7, all the optical fields in the mixer participate in the (total) field evolution. In particular, FWM will occur between any four optical frequencies if they satisfy the energy equilibrium, either supplementing power to or absorbing power from each other, as determined by the phase matching condition. Take the MI between P_1 , S_1 , and S_2 as an example, pump power will be transferred to the signals, and thus a positive power contribution to each signal, while a negative power flow for the pump. Regarding the central HoFWM term (at 1549.3 nm in Fig. 3.11), there are 25741 FWM interactions in total between the 263 optical waves affecting its power evolution along the simulated mixer. In order to analyze the suppression principle, the central tone was decomposed into these 25714 FWM interactions based on Eq. 3.7 and energy relations. In particular, all the FWM interactions associated with the central HoFWM tone were categorized by the power transfer direction. One group of the FWM products corresponds to the positive power

contribution alimenting the power into the central tone (positive power flow), whereas the other group consists of the products characterized by a negative power evolution that decreases the power of the central HoFWM tone (i.e. the negative power flow).

To demonstrate the power evolution of the central tone under the phase complimentary ($\pm 45^\circ$) 4MPS scheme, the FWM interactions classified as positive flow were power summed together at each simulated fiber position (there are 12853 positively flowed interactions at the final simulation step of the parametric mixer), shown as the red solid curve in Fig. 3.12, so as to the other group of the FWM interactions for negative flow, which was depicted as the blue solid curve in Fig. 3.12. While the total power of the central tone is the sum of these two groups, shown as black solid curve. In contrast, the dashed lines represent the case with synchronized phase setting (same as the red curve in Fig. 3.11), demonstrating that the positive flow contributes 0.82-dBm power into the central HoFWM tone, which, meanwhile, loses 0.79-dBm due to the negative power flow (blue dashed line).

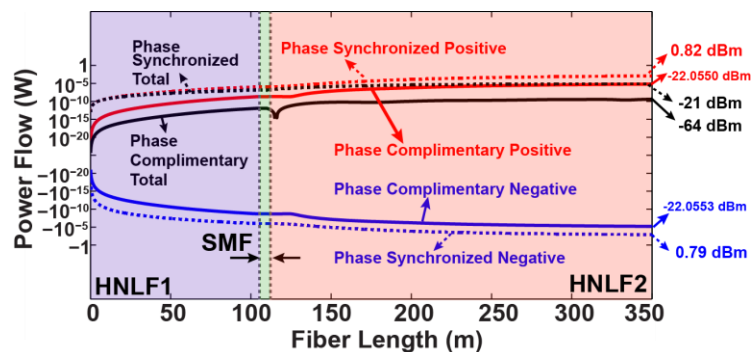


Figure 3.12 Power flow of the central HoFWM term at 1549.3 nm under phase synchronized and complementary settings. Red curves: evolution of the total positive power flow, blue curves: evolution of the total negative power flow, black curves: evolution of total power of the central HoFWM term. Solid curves: phase complementary setting, dashed curves: phase synchronized setting.

Fig. 3.12 also presents the quantized power evolution of the complimentary $\pm 45^\circ$ case (solid lines), having positive contribution of -22.055-dBm (red solid), whereas the negative flow dissipates -22.0553-dBm away from the central tone, resulting in a total power of -64 dBm at the output. Here, the total power at the output of the parametric mixer and the positive and negative power flow components were all marked in Fig. 3.12. We note that the complementary phase setting of the signal waves not only effectively reduces the efficiency of the HoFWM effects, but also causes the negative power flow to be balanced by the positive power contribution, making the total power of the central tone (black solid curve) to become negligible (i.e. -64 dBm, see the central ditch of the blue curve in Fig. 3.11) along the mixer. We note that the above analysis that constitutes the reasoning behind the adopted method, strongly implying the successful mitigation of the HoFWM in the 4MPS parametric multicasting.

3.6.2 Experimental implementation and results

We next proceed to the experimental implementation of the proposed scheme for the HoFWM suppression. The corresponding architecture and parameters have been presented in Fig. 3.4 and 3.5, consisting four partitions: coherent wave creation, pump recovery, parametric mixer and DPLL. The experimental results cover two modes of operation of the 4MPS multicaster: (i) moderate input signal power; and (ii) high input signal power. Whereas the first set of results covers the multicaster in its most practical, and also widely used mode of operation. We additionally, investigated the PS operation in the elevated input signal power regime.

Low input signal power

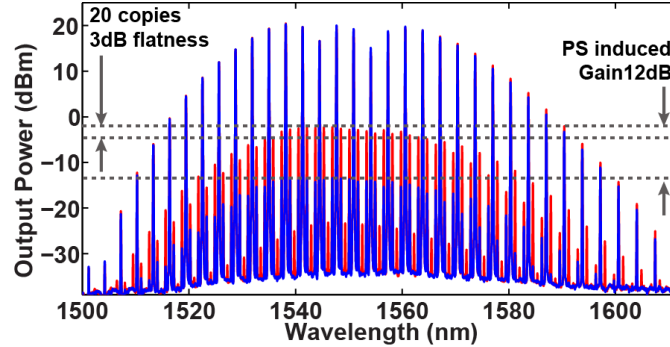


Figure 3.13 Experimental spectra comparison between PS and PI multicasting. Red curve: PS scheme with phase setting *A*. Blue curve: PI scheme.

As an introductory example of the experimental spectra, Fig. 3.13 contrasts the obtained spectra at the output of the parametric mixer in the PS and PI operation regimes. In blue shown is the PI setting, where only an input signal at 1550.1-nm with -18-dBm power was extracted by the OP and the multicasting G/CE did not depend on the input signal phase. In contrast, the stabilized PS spectrum is shown as the red curve in Fig. 3.13 (with each input signal still maintained at -18 dBm). As predicted by theory, a 12-dB G/CE improvement between the PS and PI spectra was observed (see Fig. 3.13) by managing the phases of signals (i.e. 1546.9, 1548.5, 1550.1 and 1551.7 nm) as 3, 2.7, 2 and 3 rad, respectively, in the OP (i.e. the phase setting *A*). We note that the spectra in Fig. 3.9 and Fig. 3.13 both present the maximum G/CEs, but were achieved with different phase arrangements, further confirming the multicasting G/CE profile is dictated by the phase matching condition.

In practical terms, the phase values in the setting *A* do not convey any information about the relative phase relation between the four signals. In fact, they only manifest the relative phase change of each individual signal by the OP. Due to

the absence of the information about the relative phase relation between the six waves, the observed results for neither the phase synchronized, nor the complementary settings could be (and ought to be) intuitively related to the simulations' predictions. However, the phase setting *A*, with some abuse of notation, can still be considered as a synchronized phase setting, since both the signal copies and HoFWM terms had maximized output power that were obtained by trial and error sweeping the signal phase combinations in the OP. In particular, the relative phase of each signal was individually controlled by the OP, with the signal power equalization maintained. Meanwhile, the phases of the two pump waves were manipulated by the DPLL to achieve the stabilized multicasting G/CE. Specifically, the DPLL tracked and compensated for the phase variations, and consequently maintained a constant relative phase relation between the six waves and thus stabilized the multicasting output power [57, 61]. Most prominently, however, note that the elevated gain associated with the PS operation does come at a price of a significant nonlinear crosstalk or interference, as revealed by the strong HoFWM terms in between the signal/idler tones (see the spectrum shown in red in Fig. 3.13).

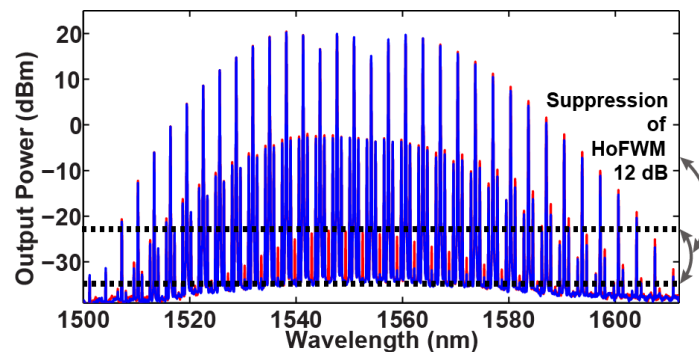


Figure 3.14 Experimental spectra of PS multicasting with each input signal power of -18 dBm, showing HoFWM suppression by signal phase manipulation. Red curve: PS scheme with phase setting *A*. Blue curve: PS spectrum with phase setting *B*.

As shown in Section 3.6.1, certain optimized phase combinations for six input waves do exist, for which the maximized G/CEs are maintained over the entire multicaster bandwidth, while the HoFWM tones are simultaneously effectively suppressed. The HoFWM-suppressed operation of the PS multicaster from Fig. 3.13 is shown in Fig. 3.14. The latter figure shows two PS spectra with equal input signal power (-18 dBm for each signal) and multicasting output G/CEs, with the red curve corresponding to the case with the phase setting *A* for the input signals (same as the red curve in Fig. 3.13). In contrast, the multicasting with the phase setting *B* (shown as blue curve in Fig. 3.14) was obtained by setting the signals' phases to 1.5, 6, 2.0, and 2.8 rad, respectively, in the OP, which was attained by trial and error phase sweeping as well. Specifically, phase sweeping of one single signal for maximizing multicasting G/CE was implemented first [57, 61], whose maximum output spectrum was employed as a benchmark for subsequent optimization. Next, the phases of all the involved modes (four signals) were optimized simultaneously and compared with the benchmark to obtain the highest G/CE, and additionally the HoFWM suppression was inspected to attain phase setting *B*. Note that, the phase setting *B* generated the 4MPS multicasting with negligible HoFWM terms over the entire 100-nm bandwidth. In particular, the maximum HoFWM suppression ratio obtained amounted to 12-dB for the central tone at 1549.3 nm.

In addition to the continuous wave (CW) (i.e. unmodulated) input operation considered above, we also verified the successful operation of the introduced method for modulated signals. Specifically, the HoFWM suppression method can potentially be used in microwave photonics applications requiring both utmost signal integrity

retention, as well as efficient bandwidth utilization. For example, in a comb-based filterless channelizer [19], the HoFWM tones cause ICI and thus degrade the sensitivity of the detection and performance. Therefore, in the latter application, it is imperative that the modulated signals induced HoFWM terms be eliminated. To demonstrate the effectiveness of the introduced technique, the HoFWM suppression was applied to the PS multicasting with analog microwave modulated input optical signals, namely millimeter-wave signals at 40-GHz and 50-GHz were amplitude imprinted onto the optical signal waves by a Mach-Zehnder modulator (MZM), while the optical signal waves were phase-managed as phase setting *B*.

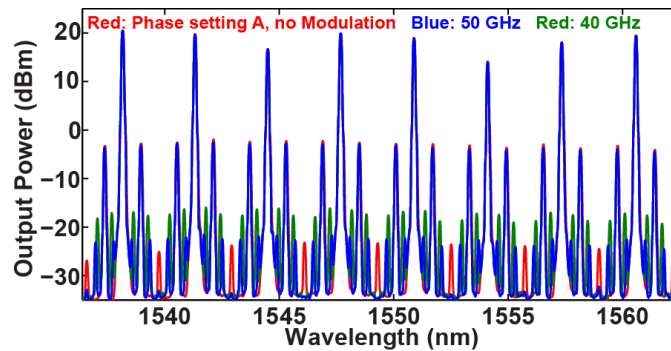


Figure 3.15 Experimental spectra of PS multicasting with high speed data modulation, where HoFWM tones were thoroughly suppressed under phase setting *B*. Red curve: Synchronized phase setting *A*, no analog signal modulation. Blue curve: Phase setting *B*, 50-GHz analog signal modulation. Green curve: Phase setting *B*, 40-GHz analog signal modulation.

The corresponding output spectra are shown in Fig. 3.15, plotted in green and blue, respectively, whereas the result from Fig. 3.14 with the phase setting *A* and no amplitude modulation is shown in red, for comparison. As seen in Fig. 3.15, and in comparison to the reference red line (i.e. the case with phase synchronized setting *A* and no amplitude modulation), the HoFWM terms have been effectively suppressed by phase manipulation in a specific manner (e.g. phase setting *B*), as recognized by the absence of parasitic interfering tones. The last result attest to the suitability of the

proposed approach for modulated input signals and specifically for micro-wave channelization devoid of parasitic interference.

High input signal power

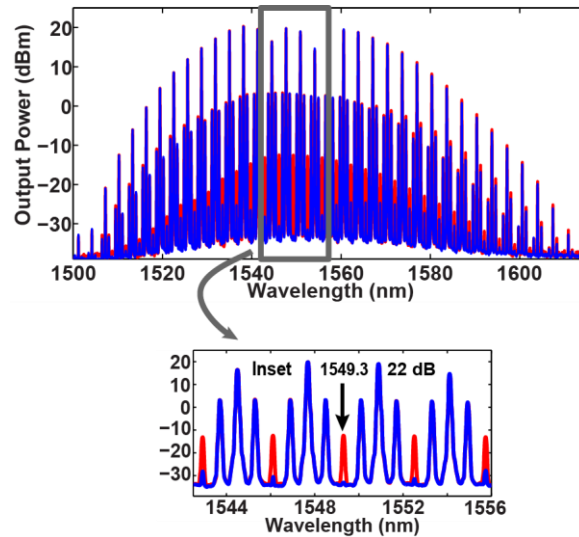


Figure 3.16 Experimental spectra of PS multicasting with each input signal power of -12 dBm, where the fully eliminated HoFWM tone has 22-dB suppression ratio, but in limited bandwidth. Red curve: PS spectrum with phase setting *A*. Blue curve: PS spectrum with phase setting *B*.

In addition to the conventional operation of the PS multicaster examined in the previous section, we also investigated the effectiveness of the proposed method for suppression of the HoFWM effects with high input signal powers. For a reference, note that in the former case shown in Fig. 3.14, the 12-dB HoFWM suppression ratio has been observed for the central HoFWM tone(s). With the power of each input signal increased to -12 dBm and the phase setting *B* employed, the suppression ratio for the central HoFWM copies (1549.3 and 1552.5 nm) was increased to 22 dB, as shown in Fig. 3.16 Inset. However, in addition to the stronger HoFWM suppression in the central region, in the case of stronger input signal power, as observed in Fig. 3.16,

the suppression of the distant spectral copies becomes spectrally non-uniform and is reduced to only about 3-dB level at the output spectrum extremities.

Note that, bandwidth selectivity in the HoFWM suppression has been predicted by the simulated spectra in Fig. 3.11 and is attributed to the phase matching conditions chromatic variation from the central tones to the multicaster emission edge [57]. Furthermore, although the signal power is increased from -18 dBm to -12 dBm and is referred as the high power condition, the difference in phase rotation induced by the signals' SPM and XPM is still negligible compared to those inflicted by the pumps'. Consequently, the HoFWM suppression has been accomplished by employing the same phase setting in both Fig. 3.14 and Fig. 3.16.

While a significant suppression variation is certainly undesirable for a wide-band operation, the HoFWM suppressed window can be easily translated across the emission spectrum by a proper input tones' manipulation, as predicted in Fig. 3.11. The tunability of the HoFWM suppression region by phase manipulation is demonstrated experimentally in Fig. 3.17, including the phase values for each case shown above each of the subplots. As can be seen, a phase change of 0.1-rad can significantly influence the output spectrum.

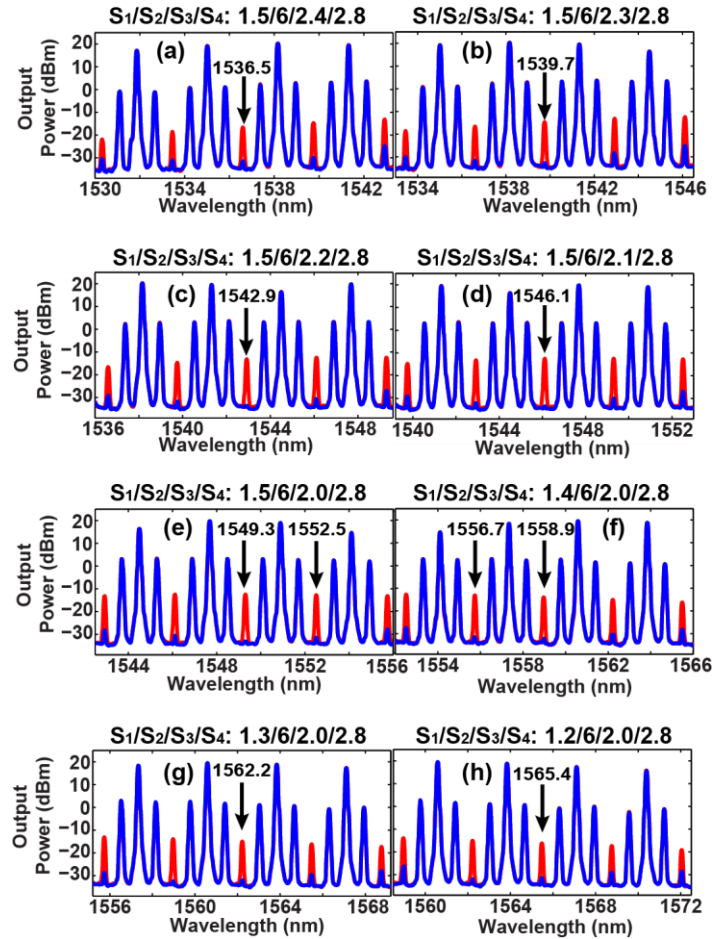


Figure 3.17 Tunability of HoFWM suppression from 1533 to 1568 nm. Red curves: PS spectra with phase setting A. Blue curves: the signals' phases are optimized to maintain G/CEs and suppress HoFWM for different wavelengths.

In particular, the tunability of the interference high order tones' suppression from 1533.3 to 1568.6 nm is demonstrated with more than 14-dB suppression ratio for each input signal power of -12 dBm, with the phases of the signal waves' appropriately set for suppression of the HoFWM tones at selected wavelengths, without compromising the signals' G/CE. The maximum suppression ratio of 22 dB is shown in Fig. 3.17(e) around 1549.3nm, while the variation of the suppression ratio is attributed to the fiber dispersion profile. We emphasize that the HoFWM cancellation in each of the cases shown in Fig. 3.17 was realized with different settings of signal

phases while the DPLL was operated with a 3-kHz bandwidth, tuning the phases of the pump waves, firstly to maximize the G/CEs, and then to maintain the relative phase relations between the pumps and signals for multicasting power stabilization.

3.7 Ultra-low noise wavelength multicasting

Section 3.1 introduces the basic principle of PS process, identifying its capability of noiseless amplification for the one-pump two-mode PS amplifier. To accomplish the noiseless wavelength multicasting, the dual-pump driven parametric mixer needs to be operated in the 4MPS mode, requiring four input optical waves present at the input with two pumps, as demonstrated in Section 3.2. In addition, the 4MPS wavelength multicasting demands strict phase manipulations, in order to achieve the 12-dB G/CE improvement compared to the PI case. Here, in this section, the investigation on the 4MPS wavelength multicasting is furthered, to validate its ultra-low noise performance theoretically and experimentally.

3.7.1 Numerical simulation in one-stage fiber mixer

Previous sections have demonstrated that the 4MPS multicasting possessing a 12-dB G/CE improvement compared to the PI case, stemming from the constructive coherent field combinations. In contrast, the incoherent noise associated with the input four signals is only power-accumulated to 6-dB increase. Mathematically, the output SNR of the 4MPS multicasting can be expressed as

$$SNR_{out} = \frac{(\mathcal{R}16G_{PI}P_{s0})^2}{4\mathcal{R}^2 16G_{PI}P_{s0}(4G_{PI}\frac{h\nu}{2})} = 4 \frac{P_{s0}}{2h\nu} \quad 3.8$$

Consequently, the theoretical NF of the 4MPS wavelength multicasting is -6 dB, assuming the NF is defined based on one input signal ($SNR_{in} = \frac{(\mathcal{R}P_{s0})^2}{4\mathcal{R}^2P_{s0}\frac{h\nu}{2}} = \frac{P_{s0}}{2h\nu}$ in Eq. 2.17). However, a more rigorous NF definition relying on the combined power of the four input signals was utilized in this dissertation (i.e. $4SNR_{in}$), leading to a theoretical 0-dB NF for the 4MPS wavelength multicasting.

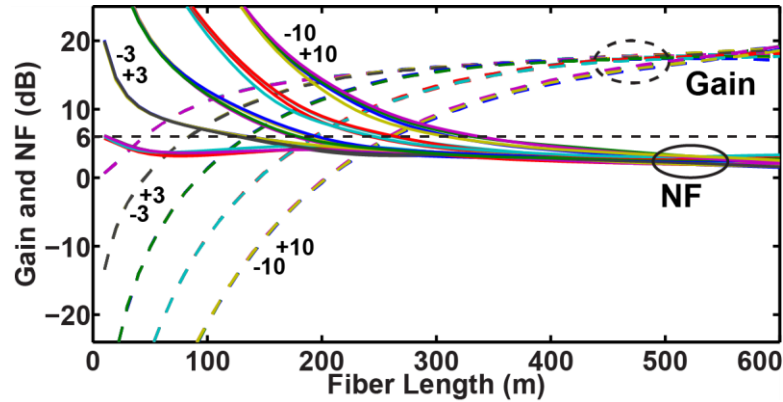


Figure 3.18 Simulated gain and NF evolution in the single stage fiber mixer.

The noise performance of the dual-pump driven PI wavelength multicasting has been numerically simulated in Section 2.4, presenting a quantum limit NF of 6-dB due to the localized noise coupling in the normally dispersive mixer. In comparison to Section 2.4, the noise evolution of the 4MPS multicasting in the 600-m dispersion flattened HNLF was numerically calculated and presented in Fig. 3.18, where the single stage HNLF had the same simulated parameters as in Section 2.4. In contrast, instead of one input signal wave (see Section 2.4), four signals at 1546.9, 1548.5, 1550.1 and 1551.7 nm were combined with two pumps and launched into the one-stage fiber. As predicted in Eq. 3.8, the central 20 signal copies have a 12-dB G/CE improvement compared to Fig. 2.7, stemming from the coherent field summation.

Most importantly, the NFs of the central 20 signal copies converged to ~1-dB, implying the ultra-low noise wavelength multicasting enabled by the 4MPS architecture.

3.7.2 Experimental characterization on NF and BER performance

To experimentally investigate the noise performance of the parametric mixer based 4MPS multicasting, NF, defined with continuous and shot-noise limited input signal wave(s), was evaluated for each output channel. Fig. 3.4 and Fig. 3.5 show the experimental configuration of the dual-pump driven parametric multicasting, and in PI case, only one input CW signal (at 1550.1 nm) was combined with co-polarized two pumps and launched into the parametric mixer. At the multicasting output, a specific signal copy was extracted from the major port of the parametric mixer by a narrow linewidth filter, and then detected by a photodetector (P) with high responsivity (Linear Photonics MPR0020). The electrical noise component was separated from the DC by a bias-T, with the PSD (S_{out}) measured by an electrical spectrum analyzer (ESA). Whereas the DC (I_{out}) component of the received signal copy was calibrated by a current meter (Agilent 34401A). Correspondingly, the expression for NF of each output channel under the PI case is

$$NF = \frac{1}{G} + \frac{P_{in}(S_{out}-S_{in})}{2h\nu I_{out}^2} \quad 3.9$$

where G is the G/CE of the replicated signal, h is the Plank constant, ν is the center frequency of the received signal copy, P_{in} is the optical power of the input signal at 1550.1 nm. Here, we note that the RIN subtraction method [62] was utilized for calculating NF, denoted as S_{in} in Eq. 3.9.

In contrast, there are four phase-correlated input signals for the 4MPS multicasting, and therefore the aforementioned RIN subtraction method for NF measurement should be modified as followed:

$$NF = 4 \left[\frac{1}{G} + \frac{P_{in} \left(S_{out} - \frac{S_{in}}{r} \right)}{2h\nu I_{out}^2} \right] \quad 3.10$$

where a factor of 4 is stemming from the fact that the NF for PS operation is defined based on the combined power of four input signals. While a calibrated factor of r in Eq. 3.10, i.e. the PS scheme induced CE improvement, scales the RIN subtraction due to the multi-mode input waves under the PS operation.

Relying on the experimental implementation in Fig. 3.4 and Fig. 3.5, and the NF calculation method, the NFs of the central 17 multicasted signal copies under the PI and PS operations were calibrated with the RIN subtraction method [62, 63], and shown as blue and red curves, respectively, in Fig. 3.19(b).

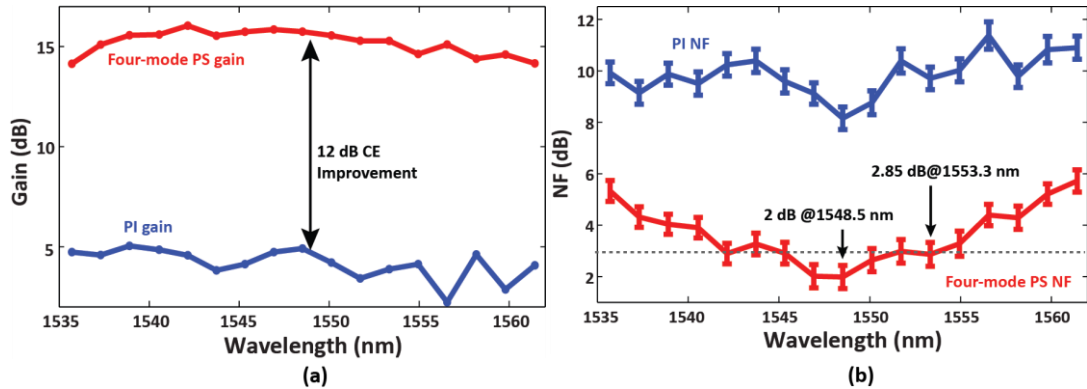


Figure 3.19 (a) G/CE comparison between the 4MPS and PI wavelength multicasting. (b) NF comparison.

Regarding the PI wavelength multicasting, the lowest NF over 17 replicas was 8.15 dB. Here, we consider the discrepancy of the PI NF from the quantum limit NF of 6-dB primarily results from the Brillouin scattering limited mixer length and its

induced inadequate localization of noise coupling. In contrast, as theory predicts, the 4MPS wavelength multicasting offers 6-dB NF benefit, as clearly demonstrated in the red curve of Fig. 3.19(b). Note that the lowest NF of 2-dB corresponds to the signal wave at 1548.5 nm; whereas regarding the newly generated replicas, the lowest NF is 2.85 dB at 1553.3 nm. Most importantly, there are 7 copies having NFs lower than 3 dB, and additionally, all the 17 replicas possess lower than 6-dB NFs. To the best knowledge of the authors, our demonstration reports the lowest NF and the highest copy number for wavelength multicasting. Note that all the PSDs were measured by the ESA at frequency of 3.37 GHz with resolution of 8 MHz and visual bandwidth of 3 Hz, and averaged over 64 iterations. The NF measurement errors ($<\pm 0.5$ dB) were calculated by differentiating Eq. 3.9 and 3.10, as illustrated by the error bar in Fig. 3.19(b). In addition, the optical G/CE profiles of the PI and 4MPS multicasting were summarized in Fig. 3.19(a), further confirming the 12-dB G/CE improvement induced by the 4MPS process.

To corroborate the tremendous advantages of the 4MPS parametric mixer, the wavelength multicasting was evaluated by BER measurements. Specifically, instead of being CWs, the input four optical signals were amplitude imprinted by a 10-Gbit/s non-return-to-zero (NRZ) on-off keying (OOK) data sequence by a MZM. Fig 3.20(a) presents the corresponding experimental architecture for the BER assessment. A specific signal copy was derived from the parametric mixer output by a wavelength division multiplexer (WDMer). Subsequently, the received optical power of the detected signal was pre-amplified by an EDFA with NF of 4.5-dB to obtain sufficient detected power on PD.

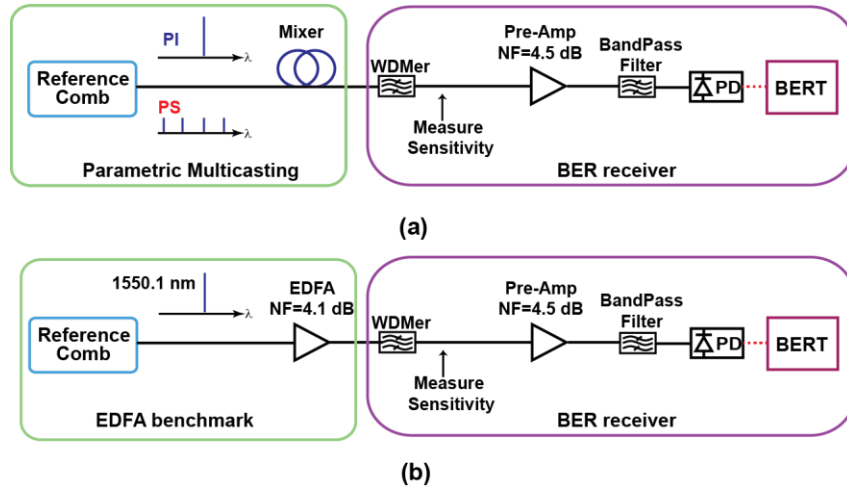


Figure 3.20 Experimental architecture of characterizing BER performance. (a) PS/PI parametric mixer. (b) EDFA benchmark.

Fig. 3.20(b) shows the experimental implementation of a comparison benchmark, where a single signal amplification at 1550.1-nm was evaluated by the same BER receiver. Specifically, instead of the parametric mixer, an EDFA (characterized by a NF of 4.1-dB) was utilized for single signal amplification, where pump recovery and DPLL was off. The corresponding BER performance was demonstrated in the black solid curve in Fig. 3.21. Here, the total power of the input optical signal(s) into the parametric mixer (or EDFA for single channel amplification) was maintained at -34 dBm, implying that the power of each input signal for PS operation is -40 dBm. We note that the presented BER curves were selected based on the availability of the WDMer.

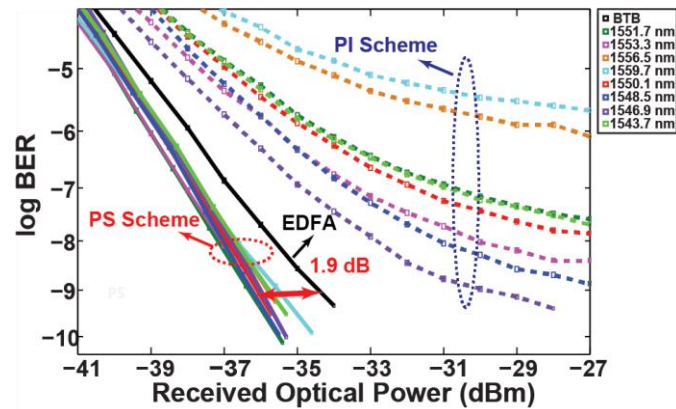


Figure 3.21 BER performance comparisons between the 4MPS and PI wavelength multicasting over eight multicasted signal copies from 1543.7 to 1559.7 nm.

Fig. 3.21 compares the BER curves of eight multicasted signal channels under the PI and 4MPS scenarios, illustrating the PS operation has a 1.9-dB receiver sensitivity improvement compared to the single channel (at 1550.1 nm) amplification by the EDFA. Moreover, multiple channels were successfully replicated with significantly improved BER receiver sensitivity compared to the EDFA, as demonstrated in Fig. 3.21.

3.8 Summary

Relying on the dispersion managed fiber mixer, the 4MPS wavelength multicasting in unsaturated gain regime was thoroughly investigated in this chapter.

Theoretical analysis, including mathematical derivation and numerical simulation, supports the dispersion-managed fiber mixer as an efficient wavelength multicaster, and the wavelength multicasting with the 4MPS architecture having noiseless performance.

Experiments with stabilized and maximized G/CE were implemented by a DPLL and phase manipulation. In particular, the HoFWM effect can be effectively

mitigated by the phase management, with the maximized G/CE maintained. Most importantly, experimental characterization on NF and BER performance validated the ultra-low noise wavelength multicasting operated in the 4MPS architecture. Record performances of wavelength multicasting were reported in this chapter.

Chapter 3, in part, is a reprint of the material as it appears in *Optics Express* in the article authored by Lan Liu, Zhi Tong, Andreas O. J. Wiberg, Bill P.-P. Kuo, Evgeny Myslivets, Nikola Alic and Stojan Radic, “Digital multi-channel stabilization of four mode phase sensitive parametric multicasting,” vol. 22, no. 15, pp. 18379-18388 (2014). The dissertation author was the primary investigator and author/co-author of this article.

Chapter 3, in part, is a reprint of the material as it appears in *Journal of Lightwave Technology* in the article authored by Lan Liu, Andreas O. J. Wiberg, Evgeny Myslivets, Bill. P.-P. Kuo, Nikola Alic and Stojan Radic, “Suppression of inter-channel higher order four wave mixing in four-mode phase-sensitive parametric wavelength multicasting,” vol. 33, No. 11, pp. 2324-2331 (2015). The dissertation author was the primary investigator and author/co-author of this article.

Chapter 3, in part, is a reprint of the material currently being prepared for submission for publication, contributed by Lan Liu, Zhi Tong, Andreas O. J. Wiberg, Bill. P.-P. Kuo, Evgeny Myslivets, Nikola Alic and Stojan Radic, “Noiseless channel cloning using four-mode phase-sensitive parametric mixer” The dissertation author was the primary investigator and author/co-author of this article.

Chapter 4 All optical regenerative multicaster

Relying on the coherent field summation of 4MPS process, dispersion engineered parametric mixer is fully capable of creating ultra-low noise wavelength multicasting, as theoretically and experimentally demonstrated in previous chapters. To accurately evaluate the noise and BER performances, the parametric mixer was operated in the unsaturated gain regime with low input signal power to meet the shot noise limited requirement.

In contrast, the investigation in this chapter focuses on all-optical phase and amplitude regenerative multicaster [64, 65], working in the saturated gain regime with high input signal power. Starting from the introduction to the basic principle and following the numerical simulations, this chapter details the experimental implementation and characterization of the 4MPS regenerative multicasting.

4.1 Introduction

Owing to the explosive growth of the internet traffic, lightwave systems and networks have been propelled from research to widespread commercial deployment. Conventionally, opto-electronic/electro-optic (OE/EO) devices were exploited in fiber communication and networks, performing various signal processing functions, such as amplification and switching [66], as well as wavelength conversion [15] in the cross-connect of the WDM networks. However, due to the limited bandwidth and restricted transparency to modulation formats of the OE/EO conversions, all-optical signal processing

techniques are anticipated to take over the dominant positions in fiber transmissions and networks. For example, the advent of optical amplifiers, which are being employed periodically in fiber transmission to compensate for the fiber loss, defines the basic architecture of all-optical communication and network. Unfortunately, the optical amplification is achieved at the expense of adding ASE to the transmission link, consequently increasing the amplitude and phase distortions, leading to degradation of the received SNR. Even worse, nonlinear phase noise that results from interaction between the amplitude noise (AN) and the fiber Kerr nonlinearity [67, 68] is detrimental to the phase encoded systems. As a result, owing to the high speed potential, low power consumption and flexibility in handling arbitrary modulation formats, it is essential to exploit all-optical regenerator to alleviate the performance degradation induced by the amplitude fluctuations and phase distortions, and consequently to increase the capacity of fiber optic transmission.

Previously, 2R (i.e. reamplification and reshaping) regeneration, designed for OOK signals, has been extensively investigated, relying on the nonlinear effects, including SPM [69-71], XPM and FWM [72-74]. In particular, due to the instantaneous response time and transparency to arbitrary modulation formats, FWM effect in saturated mode has been developed as an exceptional amplitude limiter [72-76]. In phase encoded systems, 2R regeneration needs to be combined with phase to amplitude conversion [77-79], in order to remove the nonlinear phase noise. Phase-preserving amplitude regenerator is a simpler solution [80-82], effectively mitigating the nonlinear phase noise by reducing the amplitude perturbations. In addition, the nonlinear phase noise can also be canceled by the post [83, 84] or distributed [85, 86]

phase compensations. However, none of these aforementioned methods possess re-configurability and flexibility, a necessity for an ideal all-optical regenerator. Even worse, for example, the phase to amplitude conversion inevitably induces extra noise in the regeneration process. Consequently, direct removal of phase noise by PS process is desired in the prevailing phase encoded systems. Recent developments in PS process have motivated research efforts into this direction, owing to its unique properties of ultra-low noise amplification [28] and phase squeezing [40]. For example, an all-optical regenerator based on dual-pump driven PS one-mode parametric process has been successfully demonstrated [40].

In addition to all-optical regenerator, extensive research efforts have been made to achieve various all-optical signal processing functions in last two decades, such as optical switching [87] and wavelength conversion [13, 60, 88]. Among all these essential components, wavelength multicaster, duplicating one incoming signal to multiple destinations, anticipated to increase the efficiency and scalability of the WDM network, has been introduced to contend with the growing demands of modern communication [6]. In recent studies, owing to the great capability of creating sizable number of signal copies, dispersion synthesized parametric mixer has been identified as an optimal wavelength multicaster [16, 17]. In particular, the investigations on the 4MPS wavelength multicasting with ultra-low noise performance were implemented in the unsaturated gain regime [18, 57, 58], implying that the input signal power is low so that the multicasting output signal power is linearly dependent on the input signal power, whereas the pump depletion is negligible.

In contrast, the 4MPS multicaster in the saturated gain regime is investigated in this chapter, working as an all-optical phase and amplitude regenerative multicaster. Specifically, PS process, amplifying one quadrature but de-amplifying the other, has the inherent capability of squeezing phase noise [40-42]; in addition, amplitude perturbations can be mitigated by the amplitude clamping of the saturated parametric device [75, 80]. In other words, wavelength multicasting and amplitude/phase regeneration were accomplished simultaneously in a single PS parametric device. Experimental characterizations on the 4MPS regenerative multicaster were implemented by performing measurements on BER and constellation diagrams. Most prominently, 16 newly generated signal replicas, having the regenerative performances and exhibiting negative BER receiver sensitivities compared to the noise degraded input signal(s), are demonstrated to confirm the superiority of the dispersion synthesized parametric mixer based wavelength multicasting.

This chapter is structured as follows: The basic operating principle for the regenerative multicaster is introduced in Section 4.2, including the simulations and corresponding results. Section 4.3 demonstrates the experimental implementation, indicating the input signal power range for the saturation operation. Moreover, the experimental results of the amplitude and phase regeneration over 20 multicasting replicas (signals) are reported in Section 4.4 and Section 4.5, respectively. Finally, Section 4.6 summarizes this paper.

4.2 Operating Principle

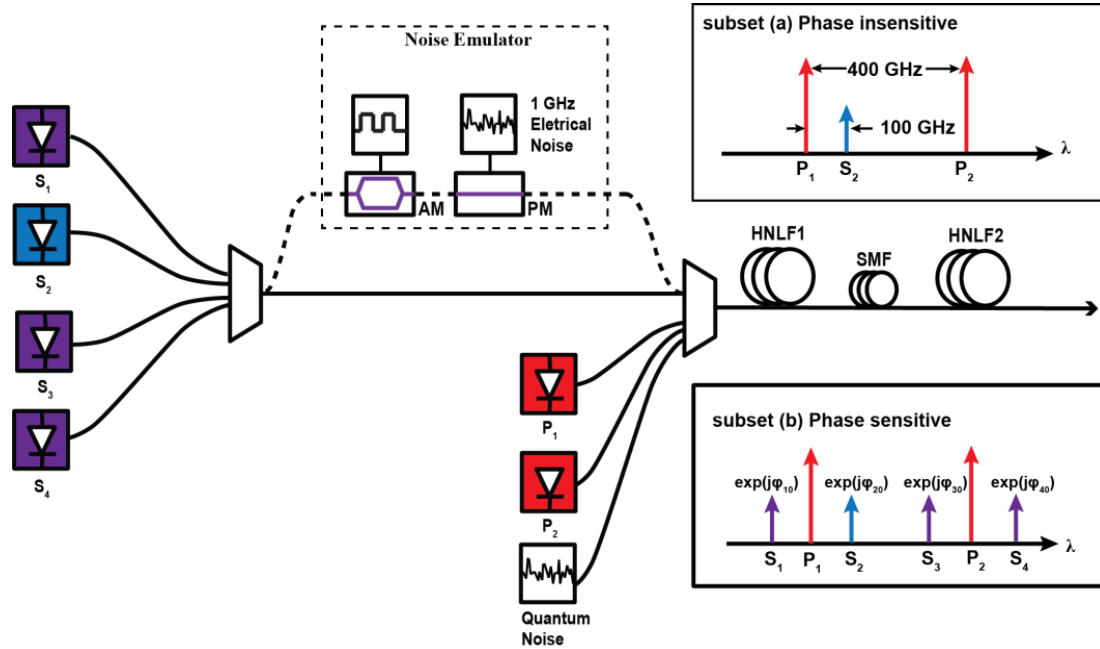


Figure 4.1 The simulated configuration in NLSE solver. P_1 , P_2 : two pumps, S_1 to S_4 : four signals, AM: amplitude modulator, PM: phase modulator, HNLF: highly nonlinear fiber, SMF: single mode fiber. subset (a) Spectral overview of pump and signal seedings in phase insensitive multicasting. subset (b) Spectral overview of pump and signal seedings for phase sensitive multicasting, where the four signals possess same data modulation and noise statistics, $\varphi_{S10} = \varphi_{S20} = \varphi_{S30} = \varphi_{S40} = \varphi_{Data} + \varphi_{noise}$

Fig. 4.1 depicts the simulated architecture of the parametric mixer. As detailed in Section 3.2, two pumps (P_1 and P_2) were picked at 1547.7 and 1550.9 nm, while four signals (S_1 to S_4) were located at 100-GHz off the closest pump. The input six waves, ideally frequency-locked and phase-correlated to each other, were combined and then launched into the three-stage, dispersion synthesized parametric mixer, with the same parameters as in Section 3.2.

When there is only one input signal (spectrally offset from the center of the two pumps, see Fig. 4.1 subset(a)), the parametric mixer is operated as a PI device,

possessing identical gain for both the in-phase and out-of-phase quadrature components of the signal field.

In contrast, a four-beam operation (see Fig. 4.1 subset(b)) has been extensively investigated in the unsaturated regime, presenting a 12-dB G/CE improvement compared to the PI mode, stemming from the constructive interference between multiple optical fields. In other words, the in-phase quadratures of the multicasting signals are amplified by g , whereas the other quadrature components experience de-amplification by $1/g$, leading to a phase-dependent multicasting G/CE profile [57] and therefore, such scenario is referred as PS mode. Owing to the amplification and de-amplification on the respective in-phase and out-of-phase quadratures, phase fluctuations will be converted to amplitude perturbations, that is the so called PS induced phase squeezing. Furthermore, the removal of the amplitude noise can be realized by the same device, as long as the parametric multicaster is operated in the saturation regime.

The response of the proposed parametric multicaster in Fig. 4.1 was calculated by the NLSE solver, where the SBS and Raman scattering were neglected. Quantum noise was modeled as an additive Gaussian white noise at the input of the mixer, with the variance defined by half-photon PSD. The pumps were initialized as having power of 0.6 W and phase of 0° , while the power of each input signal was swept from -20 dBm to 10 dBm. Corresponding, the simulated output spectra were inspected, so as to obtain the output replicas' powers and the power transfer characteristic of the parametric multicaster.

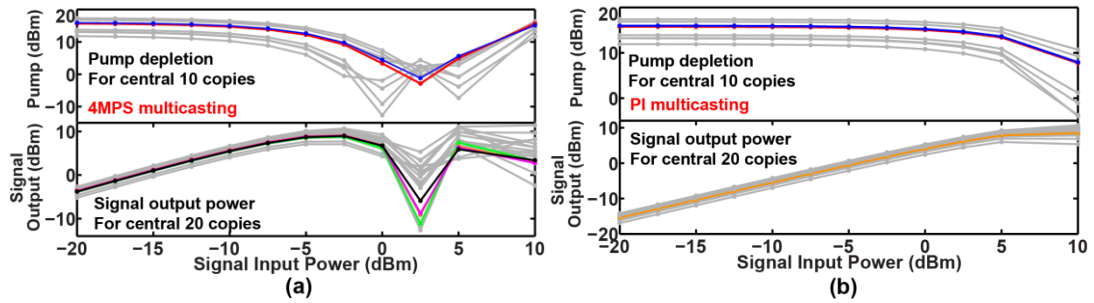


Figure 4.2 Power transfer characteristics between output and input signals, as well as pump depletion versus input signal power. (a) Power transfer curve for PS scheme. (b) Power transfer curves for PI case.

Fig. 4.2(a) presents the power transfer curve between the 4MPS multicasting output and the single input signal, as well as the pump depletion versus the input signal power. As presented, the multicaster is operated in the linear (unsaturated) regime when each input signal power is lower than -10 dBm, showing linearly increasing output power with the input signal power and negligible pump depletion. In contrast, the 4MPS multicaster is obviously operated in the saturation mode when the signal power is higher than -5 dBm. Specifically, at single input signal power of -2 dBm, the pump depletion is more than 10 dB, while the signal output power is peaked, implying that the multicaster has the capability of AN removal relying on the inherent power transfer characteristics. In addition, the power transfer and pump depletion characteristics versus the input signal power were also simulated for the PI mode, as shown in Fig. 4.2(b). Opposite to the PS operation, the PI multicasting is working in unsaturated regime, indicating that the signal output is linearly changing with input power, while the pump depletion is negligible until the signal power is higher than 5 dBm. In Fig. 4.2(a), the curves corresponding to the original input pumps (at 1547.7 and 1550.9 nm) are marked in blue and red, while the original input four signals (at 1546.9, 1548.5, 1550.1 and 1551.7 nm) are denoted as green, black, orange and

magenta curves, respectively. Whereas regarding the PI case in Fig. 4.2(b), only one input signal at 1550.1 nm was shown in the orange curve. Additionally, all the grey curves in Fig. 4.2 represent the newly generated high order pumps and signal replicas.

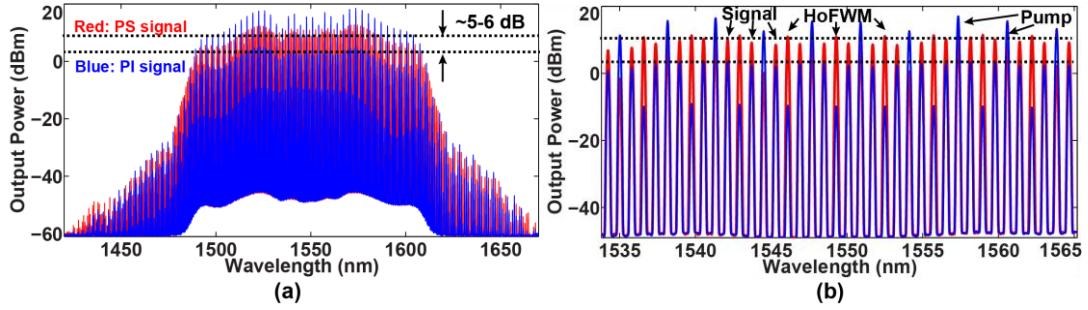


Figure 4.3 (a) Simulated spectra of parametric mixer based wavelength multicasting under 4MPS (red curve) and PI (blue curve) operation modes. (b) Expanded spectral comparison.

The simulated spectra of the 4MPS and PI multicaster were calculated at input signal power level of -2 dBm, as shown in Fig. 4.3(a). We note that instead of a 12-dB G/CE improvement [57], the saturated 4MPS multicasting presents a 5 to 6-dB G/CE improvement compared to the PI scheme, as clearly demonstrated in the expanded spectrum of Fig. 4.3(b). To achieve the maximum PS multicasting G/CE in the saturation regime, the optimum phase relations between the input six waves are not as intuitive as the unsaturated case [57]. Specifically, the depleted pumps and increased signal powers induced SPM and XPM both give substantial contributions to the phase rotations of the multicasting replicas, complicating the phase analysis and making the conclusion in Ref. [57] non-adaptive here. However, due to the saturation effect, the phase dependent property is not as critical as in the unsaturated case, and therefore, the complex phase relation and optimum phase combination are not considered in this section. While the phases of the input optical waves were judiciously selected based on extensive simulations, and to obtain the multicasting spectrum with highest

equalized G/CE in Fig. 4.3, the input waves were arranged as synchronized (i.e. 0°). In Fig. 4.3(b), we note that besides the pumps and signal replicas, the HoFWM tones have high output power due to the increased nonlinear efficiency [58], whose analysis is beyond the scope of this dissertation and will not be included either.

In addition to the power transfer characteristics, the regenerative performance of the parametric multicaster was also evaluated by constellation diagrams when the input signals were phase encoded. As shown in Fig. 4.1 (the dashed bypass following the input signals), the four optical signals were first phase imprinted by a 10-Gbit/s NRZ data pattern by making use of the π phase shift of a null-position-biased AM, a typical method for BPSK modulation. A PM, following the AM as a noise emulator, was driven by a 5.8-GHz electrical noise source. The corresponding mathematical expression for each input optical signal with phase modulation is denoted in Fig. 4.1 subset(b) (where $\varphi_{S10} = \varphi_{S20} = \varphi_{S30} = \varphi_{S40} = \varphi_{Data} + \varphi_{noise}$), while the output signal can be represented as (take S_2 as an example)

$$\begin{aligned}
 & |A_{S_2}| \cdot \exp(i\varphi_{S_2}) \\
 &= \sqrt{GP_0} (\exp(i\varphi_{S_{20}}) + \exp(-i\varphi_{S_{10}}) + \exp(-i\varphi_{S_{30}}) + \exp(i\varphi_{S_{40}})) \\
 &= 2\sqrt{GP_0} \text{COS}(\varphi_{Data} + \varphi_{noise}) \tag{4.1}
 \end{aligned}$$

where G and P_0 are the parametric gain and power of each input signal wave, respectively, assuming the input four optical waves are power balanced and the gain profile is equalized. φ_{Data} is the two-level quantized phase induced by the BPSK modulation (i.e. 0 or π). φ_{noise} is the phase perturbation generated by the noise emulator, spectrally broadening the input signal.

Eq. 4.1 indicates that the 4MPS multicasting output signal only exhibits two-state quantization (i.e. 0 or π), implying amplification on one quadrature and de-amplification on the other. In other words, phase perturbations are projected onto the in-phase quadrature, and converted into amplitude fluctuations.

Table 4.1 Simulated constellation comparison among input signal and output signals in the unsaturated and saturated operation

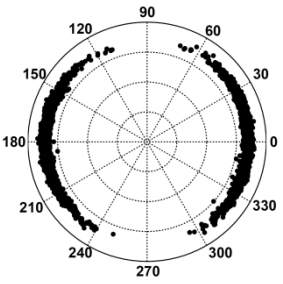
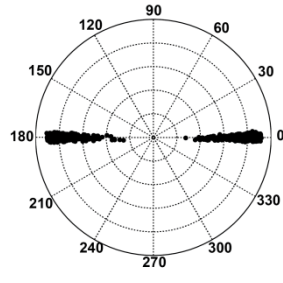
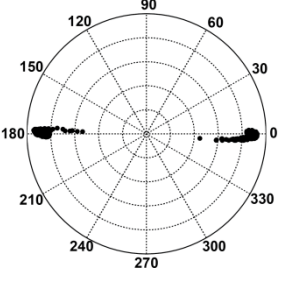
The input signal at 1550.1nm with PN perturbations	The output signal at 1550.1nm with input signal power of -10 dBm	The output signal at 1550.1 nm with input signal power of -2 dBm
		

Table 4.1 compares the simulated constellations of the multicasted output signals in the unsaturated and saturated cases. Here, the input signal constellation is shown in the first column, exhibiting $\pm 60^\circ$ phase error. In contrast, the constellation of the output signal at 1550.1 nm was shown in the second column, corresponding to the unsaturated multicaster with the input signal power of -10 dBm. As predicted, the PS operation converts the phase errors into amplitude perturbations, but the unsaturated operation has no effect on clamping the AN. On the other hand, when the signal power is as high as -2 dBm, the saturated PS operation can squeeze PN and remove AN simultaneously, as demonstrated in the third column of Table 4.1. More prominently,

the regenerator also works as a multicaster, and the regenerative multicasting is demonstrated in the experimental sections.

4.3 Experimental Configuration

As demonstrated in previous chapters (e.g. Section 3.3), four modules, including reference comb, pump recovery, parametric mixer and PLL, are constituting the experimental architecture of the 4MPS multicasting. Relying on the same experimental configuration, 4MPS regenerative multicaster was achieved with increased signals' powers, as shown in Fig. 4.4. In addition, a fifth signal processing module was inserted into the signal path for phase encoding and signal power amplification. Nevertheless, in subsequent experimental demonstrations, the fiber lengths of the two pump paths, containing injection locking lasers and high power EDFAs, were matched to the signal processing block length within 1-cm difference, in order to maintain the coherence between the input waves.

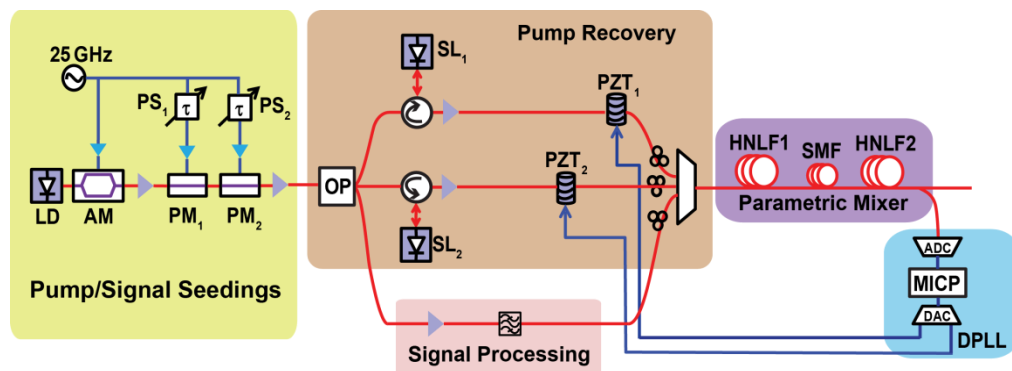


Figure 4.4 Experimental architecture for all-optical multicaster and regenerator, consisting of five parts: Creation of pump/signal seedings, Pump recovery, signal processing, parametric mixer, and DPLL. LD: laser diode, AM: amplitude modulator, PM: phase modulator, PS: phase shifter, OP: optical processor, SL: slave laser, PZT: piezoelectric transducer, HNLF: highly nonlinear fiber, SMF: single mode fiber, MICP: microprocessor, ADC: analog-to-digital converter, DAC: digital-to-analog converter

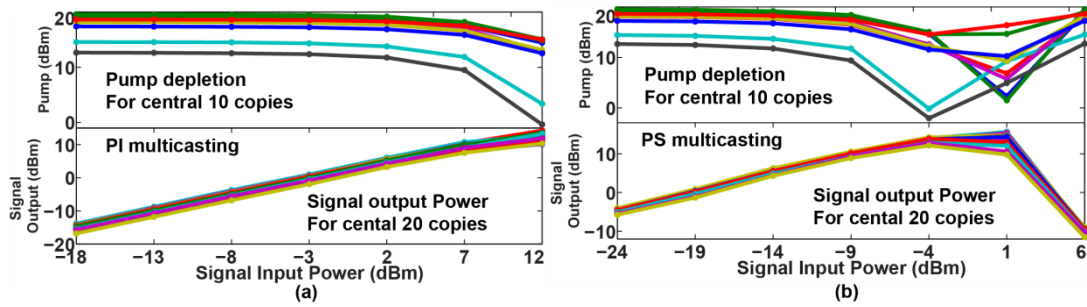


Figure 4.5 Experimental power transfer function of parametric wavelength multicasting under 4MPS (a) and PI (b) modes, as well as the pump depletion versus the input signal power.

To learn the input power range for the saturated operation, the power transfer characteristics of the parametric multicaster under the PI and 4MPS modes were measured by step-changing the input signals' powers, as shown in Fig. 4.5. Fig. 4.5(a) clearly demonstrates that the saturated PI multicaster demands high input signal power (7 dBm). In contrast, the 4MPS multicaster is operated in the saturation regime at much lower input power (as low as -4 dBm), stemming from the fact that the PS constructive summation induced increased output signal power and consequently enhanced saturation effects. The corresponding output spectra of the parametric mixer with input signal power of 0-dBm is shown in Fig. 4.6. Specifically, as indicated in the power transfer curves of Fig. 4.5, the 4MPS multicaster (shown as red curve in Fig. 4.6) with 0-dBm input signal power is working in the saturation mode, whereas the corresponding PI counterpart (shown as blue curve in Fig. 4.6) is working as an unsaturated case. Consequently, the PS induced G/CE improvement is 5-dB at most (less than 12 dB), as shown in the magnified spectrum of Fig. 4.6(b). Here, we note that the stabilized phase relation (as well as constant 4MPS multicasting output power) was guaranteed by the DPLL, while the signals' phases were optimized by trial and error phase sweeping to obtain the equalized highest G/CE profile. Note that, the

reduced HoFWM tones (see Fig. 4.6) are not considered in this dissertation, which, however, can be reduced by optimization of signals' phases [58, 59]. We next proceed to the experimental details and results in Section 4 and 5, covering two functions of the 4MPS multicaster: amplitude regenerator and phase squeezer, respectively.

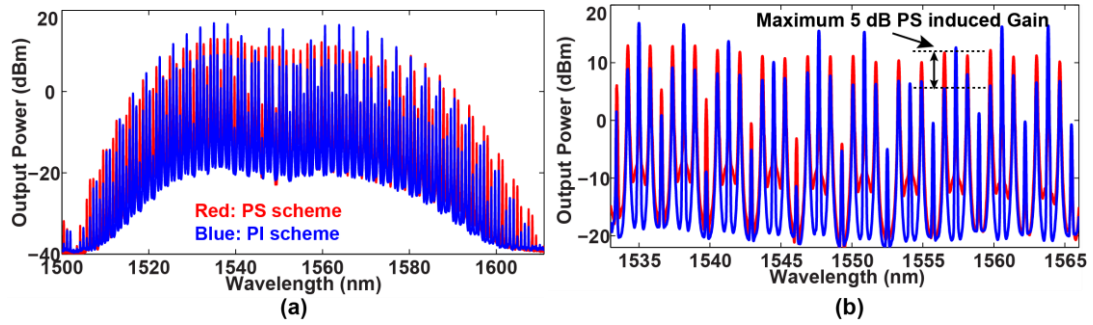


Figure 4.6 Experimental spectra of 4MPS multicaster under saturated operation mode. (a) entire spectrum. (b) expanded spectrum for central 20 replicas.

4.4 Amplitude Regeneration

As predicted by the power transfer characteristics in Fig. 4.5, compared to the PI operation, the 4MPS multicaster has the potential to enhance the AN regeneration over multiple replicas at relatively low input signal power [64]. To implement AN regenerator and verify the effectiveness of the regenerative performance over multicasted replicas, the experimental configuration in Fig. 4.7 was constructed based on the aforementioned 4MPS multicaster, and additionally was equipped with data modulation and noise emulation for BER characterization in the signal processing block. Specifically, in the signal processing part, the four optical signals were amplitude imprinted with a 10-Gbit/s NRZ-OOK data pattern, instead of being operated as CWs. Subsequently, the four input signals were further modulated by a second AM, driven by 1-GHz-wide electrical thermal noise source, which was

produced as a random data sequence by an arbitrary waveform generator (AWG) and then amplified to a specific power level. At the output of the parametric mixer, 10% of the power was divided into the DPLL for phase optimization and power stabilization, whereas specific signal replicas were individually derived from the rest of the output power by a narrow-band tunable filter, and then photo-detected for BER counting.

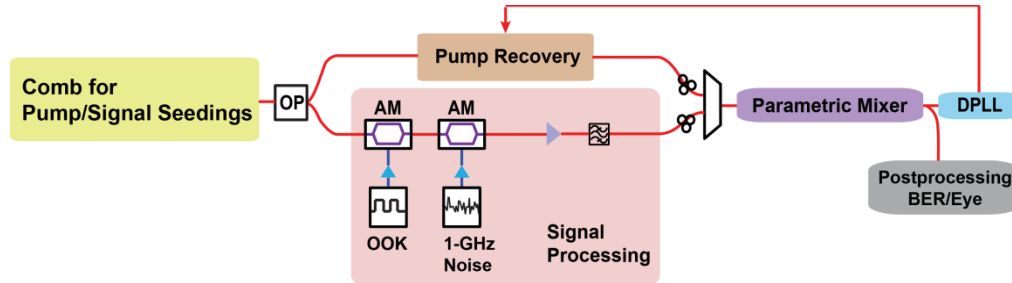


Figure 4.7 Experimental configuration for AN regeneration.

Ref. [64] demonstrated successful amplitude regenerative multicasting over 10 signal copies with two AN levels, including BER performances and eye diagrams. Here, the AN regeneration was extended to 20 multicasting replicas (from 1534.1 to 1564.7 nm), and the corresponding BER measurements are presented in Fig. 4.8(a). To validate the superiorities of the 4MPS multicaster, a single channel (at 1550.1 nm) amplification was measured as a BTB benchmark for comparison. The corresponding BER curve, shown as the dashed black curve in Fig. 4.8(a), was achieved by turning off the powers of two pumps and three signals, and data imprinting one signal at 1550.1 nm before EDFA amplification. Additionally, when the single signal (at 1550.1 nm) was contaminated by electrical noise source through the second AM (see signal processing module in Fig. 4.7), the BER performance was represented by the black solid curve in Fig. 4.8(a), with 5-dB sensitivity degradation. The input AN was calibrated by noise to signal-mean ratio (after noise modulation without data

imprinting) in electrical domain (ENSR), corresponding to 4% in the BER measurements of Fig. 4.8(a).

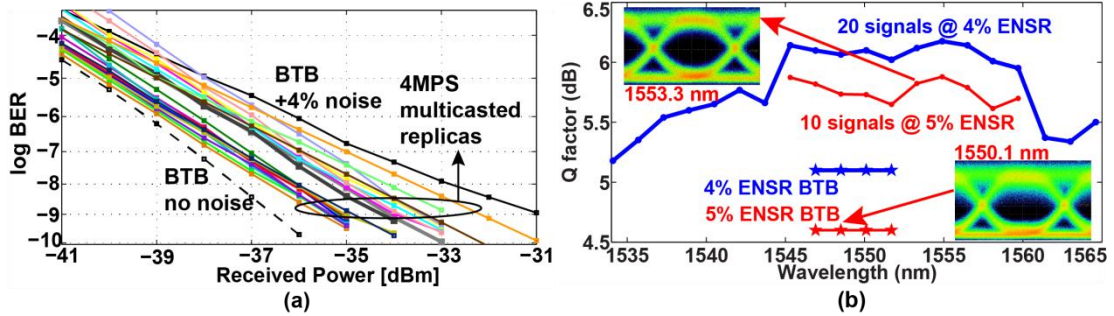


Figure 4.8 (a) BER curves for BTB with and without the artificial AN source, and the central 20 multicasting signal copies. (b) Q factor and eye diagram comparison between the multicasting output and input at the receiver sensitivity of -35 dBm. Q factor spectra for input BTB condition with 4% and 5% ENSR were presented as blue and red solid curves with star, respectively. Q factor spectra for central 20 multicasting replicas with 4% and 5% ENSR were presented as blue and red solid curves with dot, respectively

In contrast, the BER curves of the central 20 signal copies for the 4MPS multicaster all exhibit negative penalties, compared to the AN degraded BTB BER curve. In particular, the central 10 copies of the 4MPS multicasting show 4-dB sensitivity improvement [64]. Here, we note that the multicasted replicas have at least 1-dB BER penalties compared to the black dashed curve, i.e. BTB curve without added AN, which is ascribed to the imperfect power transfer characteristics of the 4MPS multicaster (see Fig. 4.5(b)). Ideally, a step-function of the power transfer curve is preferred for amplitude regenerator, in order to suppress the signal fluctuations in both marks and spaces [73, 89]. However, our simulated and experimental power transfer curves (see Fig. 4.2 and Fig. 4.5) are not in the optimal situations, leading to residual AN and BER sensitivity degradation. Nevertheless, the 4MPS multicaster can effectively work as an AN regenerator over 20 signal copies. An elevated AN level (i.e. 5% ENSR) has been tested in [64], where the 4MPS multicaster (over 10 signal

copies) possesses more than 6-dB receiver sensitivity improvement compared to the AN perturbed BTB.

Furthermore, the corresponding Q factor spectra of the 4MPS multicasting, assessed at the receiver sensitivity of -35 dBm, were summarized in Fig. 4.8(b). With the input noise level of 4% ESNR, the corresponding Q factor is 5.1 dB, shown in blue star curve. In contrast, the central 10 multicasted replicas exhibit more than 1-dB Q factor improvement (the solid blue dot curve).

In addition, the input and output Q factors of the 4MPS wavelength multicasting with 5% ESNR are represented in red curves, exhibiting more than 1-dB difference as well. Moreover, two eye diagrams for the newly generated replica (at 1553.3 nm) and BTB input (at 1550.1 nm) are compared in Fig. 4.8(b), in order to visually confirm the superiority of the 4MPS regenerative multicaster.

4.5 Phase Regeneration

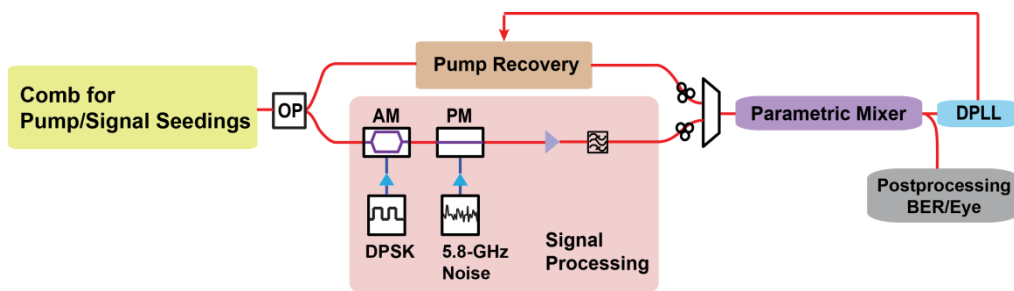


Figure 4.9 Experimental configuration for 4MPS multicaster as a phase noise regenerator.

The measurements on squeezing PN, having the same experimental structure as the AN regeneration, were implemented as shown in Fig. 4.9. However, the data imprinting AM in the signal processing block was biased at null position (instead of the quadrature position) and driven by a 10-Gbit/s pseudorandom binary sequence

(PRBS) NRZ data to achieve differential phase-shifted keying modulation format. A PM followed and was exploited as a PN emulator, modulated by an AWG-generated and amplified 5.8-GHz random data sequence. Subsequently, the optical signals were amplified to certain power level (the power of each input signal was 0 dBm), allowing the multicaster to be working in the saturation mode.

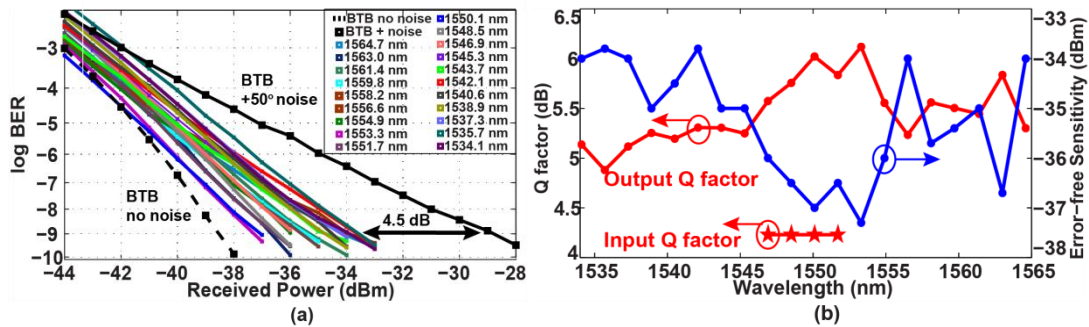


Figure 4.10 (a) The BTB BER curves without and with PN are shown in black dashed and solid curves, respectively. The colorful solid curves represent the BER curves of the central 20 signal copies, characterizing the 4MPS multicaster performance as a phase regenerator, where the phase error amounted to $\pm 50^\circ$. (b) Red curve: Q factor corresponding to the received central 20 signal copies at the receiver sensitivity of -37 dBm. Blue curve: the corresponding receiver sensitivities at BER of 10^{-9} (error-free detection) for the central 20 multicasting copies.

The phase regeneration was characterized by BER performance, Q factor and constellation diagram analysis. Fig. 4.10(a) presents the BER performance over 20 multicasted replicas, where the BTB curve was measured for single signal amplification (at 1550.1 nm) under the same circumstances as in Section 4.6 (pump recovery and DPLL were turned off, while the parametric mixer was substituted by an EDFA). The extent of the phase errors was manipulated by controlling the electrical amplifier output power into the PN modulator (i.e. the power of the 5.8-GHz electrical noise source). Correspondingly, the phase perturbations on the optical signals amounted to $\pm 50^\circ$ [65], induced receiver sensitivity degradation by as much as 9.5 dB,

shown as the solid black curve in Fig. 4.10(a). In contrast, the 4MPS multicaster successfully squeezes the phase noise by selectively amplifying one quadrature and de-amplifying the other. Consequently, phase noise was transferred to amplitude perturbations, which were effectively suppressed by saturation effect. Fig. 4.10(a) shows the BER performance of the central 20 signal copies with at least 4.5-dB BER sensitivity improvement, whose corrected constellations have been evaluated in Ref. [65]. Here, the Q factors over 20 multicasted signal copies and input signals were analyzed and compared at receiver sensitivity of -37 dBm, exhibiting a maximum 2-dB Q factor improvement (at 1553.3 nm). Additionally, there is at least 0.6-dB correction over 20 multicasting replicas. The corresponding error-free receiver sensitivities were also summarized in Fig. 4.10(b), comparing the regenerative performance of the central 20 multicasted replicas, as well as validating the 4.5-dB receiver sensitivity improvement induced by the PN regeneration.

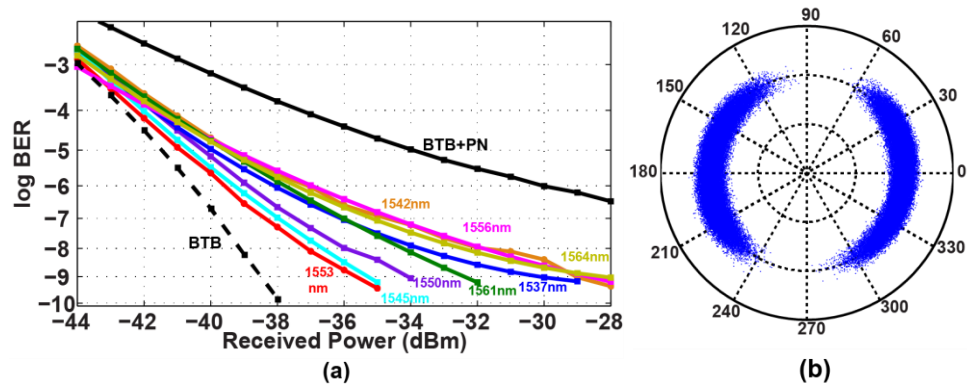


Figure 4.11 (a) The BTB BER curves without and with PN are shown in black dashed and solid curves, respectively. The colorful solid curves represent the BER curves of the selected eight signal copies, characterizing the 4MPS multicaster performance as a phase regenerator. (b) The corresponding constellation for input signal with $\pm 60^\circ$ phase errors.

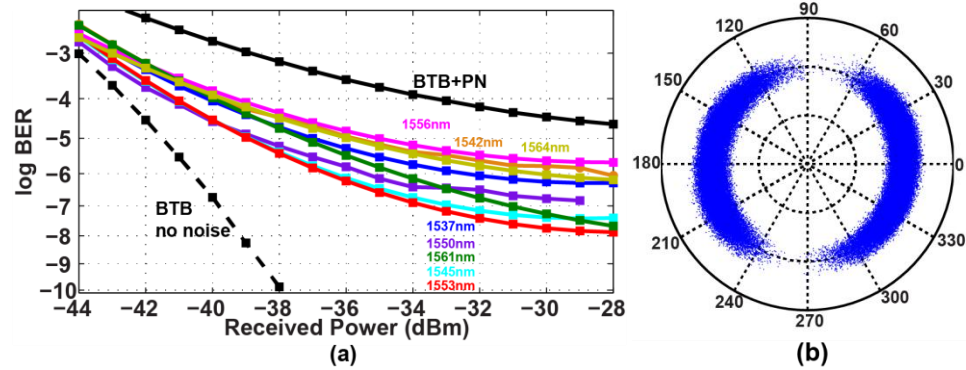


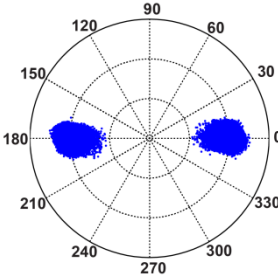
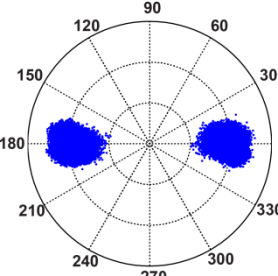
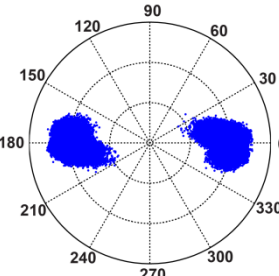
Figure 4.12 (a) The BTB BER curves without and with PN are shown in black dashed and solid curves, respectively. The colorful solid curves represent the BER curves of the selected eight signal copies, characterizing the 4MPS multicaster performance as a phase regenerator. (b) The corresponding constellation for input signal with $\pm 60^\circ$ phase errors.

Furthermore, the BER performances and constellation diagrams were also evaluated at elevated input noise levels. The input BTB signal with increased phase perturbations, corresponding to $\pm 60^\circ$ constellation in Fig. 4.11(b), was represented as the black solid curve with an error floor in Fig. 4.11(a). In contrast, eight multicasting copies, including the amplified input signal (at 1550.1 nm) and the newly generated copies (in the middle and extreme edge of the multicasting spectrum), were derived from the narrow bandwidth filter individually and assessed for the BER performance, possessing error free detection and more than 6 dB sensitivity improvement compared to the PN degraded input signal.

The noise level was even increased to phase perturbation of $\pm 75^\circ$, as presented by the constellation diagram of the input signal (at 1550.1 nm) in Fig. 4.12(b). Fig. 4.12(a) shows the BER characteristics of the selected 4MPS multicaster replicas, exhibiting a reduced detection error floor. In other words, the 4MPS multicaster still has detection improvement compared to the PN degraded BTB BER curve. To

visually validate the regenerative performance of the 4MPS multicaster, the output suppressed constellations were summarized in Table 4.2.

Table 4.2 Constellation comparison for the 4MPS multicasting output replicas at selected wavelengths

Multicasting output at 1550.1 nm	Multicasting output at 1553.3 nm	Multicasting output at 1556.5 nm
		

4.6 Summary

In this chapter, the parametric mixer based 4MPS multicaster has been investigated as an efficient means for all-optical regeneration. Relying on the mathematical derivations and simulations, we have theoretically presented that the phase errors were squeezed into amplitude fluctuations by the phase dependent amplifications and de-amplifications, while the amplitude perturbations were further regenerated by the power transfer characteristics of the parametric effect.

Experiments on amplitude regeneration over multiple multicasted signal copies were successfully implemented based on the 4MPS multicaster. The corresponding BER performances, Q factors and eye diagrams with two AN levels were evaluated to validate the amplitude regenerative multicaster. Furthermore, the 4MPS multicaster was also experimented with BPSK signals, and characterized by BER curves and

constellation diagrams, presenting successful phase squeezing even with input phase error of $\pm 75^\circ$. Most prominently, this is the first experimental demonstration of an all-optical regenerative 4MPS multicaster, producing over 20 signal replicas.

Chapter 4, in full, is a reprint of the material currently being prepared for submission for publication, contributed by Lan Liu, Eduardo Temprana, Vahid Ataie, Andreas O. J. Wiberg, Bill. P.-P. Kuo, Evgeny Myslivets, Nikola Alic and Stojan Radic, “All optical wavelength multicaster and regenerator based on four-mode phase-sensitive Parametric Mixer.” The dissertation author was the primary investigator and author/co-author of this article.

Chapter 5 One-mode and three-mode phase sensitive wavelength multicasting

Dual-pump driven dispersion synthesized parametric mixer has been identified as an efficient method for wavelength multicasting. Relying on the 4MPS architecture, the ultra-low noise performance of the wavelength multicasting has been theoretically and experimentally demonstrated in Chapter 3. In addition, Chapter 4 discusses the all-optical phase and amplitude regenerative multicasting based on the saturated 4MPS parametric mixer.

To further corroborate the superiorities of the PS multi-mode operation, degenerate one- and three-mode PS parametric multicasting were numerically and experimentally compared in this chapter, in terms of phase manipulation and G/CE, as well as noise performance.

5.1 Introduction

The PS process, amplifying the in-phase quadrature but de-amplifying the out-of-phase one, has gained substantial attention in recent years. Relying on such phase dependent property, considerable research efforts have been made towards accomplishing noiseless amplification [27, 28] and phase squeezing [40, 90]. In particular, most of the reported PS experiments have been achieved by nonlinear parametric effects, relying on χ^2 [27, 90] and χ^3 [28, 40] nonlinear platforms. Specifically, the PS process superimposes the correlated photons at identical (degenerate) or distinct (non-degenerate) wavelengths for constructive field

summation, in addition to the parametric effect induced nonlinear gain, leading, consequently, to improved SNR.

As aforementioned, the investigation in this dissertation focuses on the χ^3 nonlinearity based dispersion-synthesized parametric mixer, in order to obtain ultra-low noise wavelength multicasting. Dependent on the input signal wave number and degenerate/non-degenerate configuration, the parametric multicasting can be categorized as one-, two-, three- and four-mode, respectively. Most of these proposed schemes have been experimentally implemented for specific interests and applications. For example, a record low NF of 1.1-dB has been reported for FOPA, a one-pump two-mode PS process [28]. While the 4MPS architecture has been employed in dual-pump driven dispersion-synthesized parametric mixer for broadband wavelength multicasting [16, 17], whose ultra-low noise performance [18] and phase squeezing over 20 multicasted signal copies [65] have been experimentally validated in previous two chapters.

On the other hand, due to the inherent simplicity, one-mode FOPA has been extensively investigated. In particular, fully degenerate one-mode PS process, i.e. pump and signal sharing the same frequency, has been theoretically discussed and experimentally demonstrated, as shown in Fig. 2.3(a). Before the 1980s, theoretical work has been reported, describing such one-mode PS process as potential method for quadrature squeezing [39]. Subsequently, the experimental implementations replying on the interferometric structures, like Mach-Zehnder interferometer and Sagnac loop, have been reported in Ref. [91-93], certainly validating the phase dependent amplification and quadrature squeezing. While the capability of noiseless

amplification was experimentally confirmed by [26, 94], demonstrating a NF of 1.8 dB, lower than the quantum limit NF of 3-dB for the PI device. In addition to the ultra-low noise operation, phase noise regeneration has been achieved by the fully degenerate one-mode PS amplifier [42, 95]. Here, we note that the PS parametric device not only squeezes the phase variations, but also mitigates the amplitude fluctuations by the saturation effect, as illustrated in Chapter 4. Even though the first experimental demonstrations of ultra-low noise amplifier and phase regenerator were achieved by the fully degenerate configuration, the parametric gain is restricted by quadratic profile, instead of having exponentially increasing gain. Even worse, the interferometric configuration associated with the fully degenerate scheme is fundamentally limited by the guided acoustic-wave Brillouin scattering.

To eliminate these drawbacks, dual-pump driven degenerate one-mode (signal wave is spectrally positioned in the middle of the two pumps) parametric amplifier, inherently a PS device, has been utilized as an all-optical regenerator in phase-encoded systems [40, 96]. Experimental BER characterization on such PS one-mode parametric process has demonstrated successful regenerative wavelength multicasting over 5 replica copies [97]. However, to fully exploit the potential of dual-pump driven one-mode PS parametric multicasting, rigorous characterizations are dictated, i.e. NF evaluation. Equally important, in terms of the multicasting efficiency, smart design of the parametric mixer is demanded for high count copy number.

In this chapter, the dual-pump driven PS one-mode process was employed in the dispersion-synthesized parametric mixer, and characterized by NF measurement and BER evaluation. In contrast, three-mode PS multicasting is first demonstrated

here, anticipated to possess noiseless performance over multicasted signals. In addition, the phase relations between the input pumps and signal(s) were numerically calculated, comparing the phase dependent properties between PS one- and three-mode multicasting. Most prominently, nearly noiseless multicasting, relying on the three-mode PS process, was theoretically and experimentally addressed here.

This chapter is structured as followed. Section 5.2 introduces the theory of dual-pump driven single- and multi-mode wavelength multicasting, including simulations and corresponding results. The experiments based on the proposed one- and three-mode configurations were experimentally implemented, as detailed in Section 5.3. Section 5.4 discusses the rigorous characterizations on NF and BER performances, in order to corroborate the superiority of the multi-mode PS multicasting. Section 5.5 summarizes this paper.

5.2 Theory

The frequency configurations of dual-pump driven single- and multi-mode parametric processes are shown in Fig. 5.1. Fig. 5.1(a) presents the input scheme of the PI one-mode multicasting, where the input signal frequency is offset from the center of the two pumps. While the corresponding 4MPS counterpart is presented in Fig. 5.1(b). Both of these two schemes have been theoretically and experimentally [18, 57] investigated in Chapter 2 and 3, respectively. Particularly, the 4MPS parametric multicasting features ultra-low noise performance [18] and phase squeezing properties [65] over 20 signal copies, validating the superiorities of multi-mode operation.

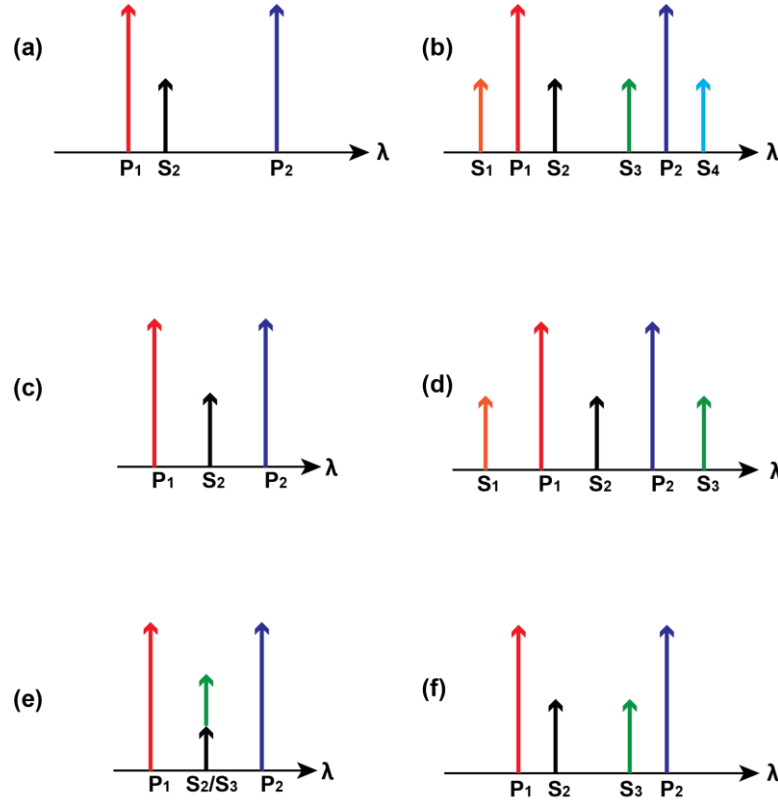


Figure 5.1 (a) Dual-pump driven PI one-mode scheme. (b) Dual-pump driven 4MPS configuration. (c) Dual pump driven PS one-mode configuration. (d) Dual-pump driven PS three-mode configuration. (e) PS one-mode scheme is equivalent to the dual pump driven two-mode case, as shown in (f). (f) Dual-pump driven two-mode configuration

Here, we further our studies on single- and multi-mode parametric multicasting, focusing on the degenerate one- and three-mode schemes. The dual pump driven degenerate one-mode configuration, shown in Fig. 5.1(c), has the signal frequency located in the middle of the two pumps, i.e. $\omega_{P_1} + \omega_{P_2} = 2\omega_{S_2}$. Theoretically, the parametric interaction between P_1 , P_2 and S_2 creates a conjugated idler at the frequency of S_2 (i.e. S_2^*), leading to interferometric interference between S_2 and S_2^* . Consequently, dual-pump driven degenerate one-mode scheme is inherently a PS process, so as to the three-mode scheme, as shown in Fig. 5.1(d).

Previously, the noise properties of the dual-pump degenerate one-mode PS amplifier has been simulated in depth [98], illustrating that close to 0-dB NF can be obtained if the parametric nonlinear processes are constrained in the input three waves (no high order pumps and signals generated). Confidently, we believe that the same principle works for the dual-pump driven three-mode PS amplifier (without no high order pumps and signals), since all the internal modes are occupied by the input waves [39], and no extra noise will be introduced to the three-mode PS amplifier.

On the other hand, when the one- (shown in Fig. 5.1(c)) and three-mode (shown in Fig. 5.1(d)) PS processes were employed in the wavelength multicasting, HoFWM processes create high order pumps and therefore more signal replicas are multicasted by the cascaded FWMs. Our previous investigations have indicated that the noise properties of the high copy-count wavelength multicasting in normally dispersive parametric mixer has a quantum limit NF of 6-dB, instead of scaling up with the copy number (see Chapter 2). Here, the response of the PS one- and three-mode wavelength multicasting and its noise performance were simulated by the adaptive-step NLSE solver.

One-stage fiber mixer

First, numerical simulations were implemented in a one-stage fiber mixer, same as the simulation in Section 2.4 and Section 3.7. Specifically, two pumps (at 1547.7 and 1550.9 nm) were initialized as having input power of 0.6 W and phase of 0° . One input signal was picked at 1549.3 nm (i.e. the center frequency between the two pumps) with power of -20 dBm and phase of 0° (S_2 in Fig. 1(c)), combined with two pumps and launched into the 600-m dispersion flattened HNLFF, characterized by

a peak dispersion of -0.05 ps/nm/km and dispersion fluctuation less than 0.5 -ps/nm/km over 100-nm bandwidth. Here, we note that the pump and signal fields were treated as classical waves, whereas the quantum noise (vacuum fluctuations) was modeled as additive Gaussian white noise at the mixer input, characterized by a half-photon variance. The NF was obtained by calculating the ratio between the input and output electrical SNRs of the wavelength multicasting, as demonstrated in Chapter 2 and 3.

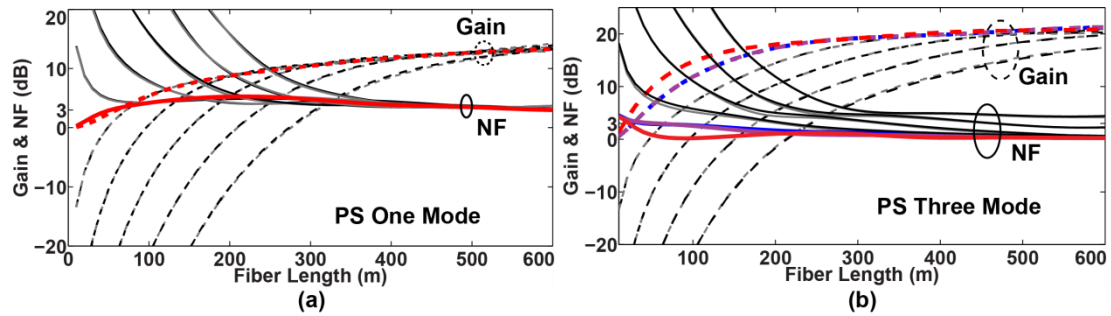


Figure 5.2 Gain and NF evolution diagrams for one- (a) and three-mode (b) PS wavelength multicasting in normally dispersive HNLF.

Fig. 5.2(a) shows the G/CE and NF evolution diagrams of the central 11 signal copies of the PS one-mode multicasting, where the solid curves represent NFs, and the dashed ones denote the G/CE profiles. The red dashed and solid curves correspond to the gain and NF evolutions of the single signal wave at 1549.3 nm in the fiber mixer, respectively. The newly generated high order signal waves' frequencies are symmetric to 1549.3 nm, and the symmetric pairs possess similar CE and noise performances, which are represented in black and grey curves, respectively. Here, it is not necessary to distinguish the specific performances of each frequency copy. Owing to the localization effect in the normally dispersive mixer, the central 11 copies have G/CE profiles converged to 13 dB, and possess a quantum limit NF of 3 dB. In essence, the

signal wave in the middle of the two pumps can be considered as two waves, sharing the same frequency (see Fig. 5.1(e)), and consequently, degenerate PS one-mode configuration is equivalent to the two-mode PS process (see Fig. 5.1(f)), possessing a quantum limit NF of 3 dB.

In addition, the noise evolution of the PS three-mode wavelength multicasting was simulated under the same circumstances but with three equalized input signal waves (at 1546.1, 1549.3 and 1552.5 nm, each having power of -20 dBm and phase of 0°), as shown in Fig. 5.2(b). Correspondingly, the red curves represent the signal wave at 1549.3 nm, while the magenta and blue curves denote the signal waves at 1546.1 and 1552.5 nm, respectively. Compared to the PS one-mode case, three-mode multicasting has a gain improvement close to 9-dB, stemming from the constructive field combination. More importantly, the NFs of the central copies converge to 0-dB, implying the essential capability of noiseless amplification and multicasting.

Three-stage dispersion synthesized parametric mixer

Recognizing the advantages of the PS multi-mode multicasting, we calculated the frequency response of the dispersion-synthesized parametric mixer based one- and three-mode multicasting, as shown in Fig. 5.3. Here, two pumps were initialized as having input power levels of 0.6 W and phase of 0° , while one input signal was picked at 1549.3 nm with power of -20 dBm and phase of 0° , exactly the same as in Fig. 5.2. However, instead of one normally dispersive HNLF, the input waves were launched into the three-stage parametric mixer (105-m HNLF1+6-m SMF+230-m HNLF), as detailed in Chapter 2 to Chapter 4. The simulated spectra of the one- and three-mode PS wavelength multicasting are shown in Fig. 5.3, where all the input waves were

initialized as phase of 0° , i.e. phase synchronized, and no phase fluctuations are considered.

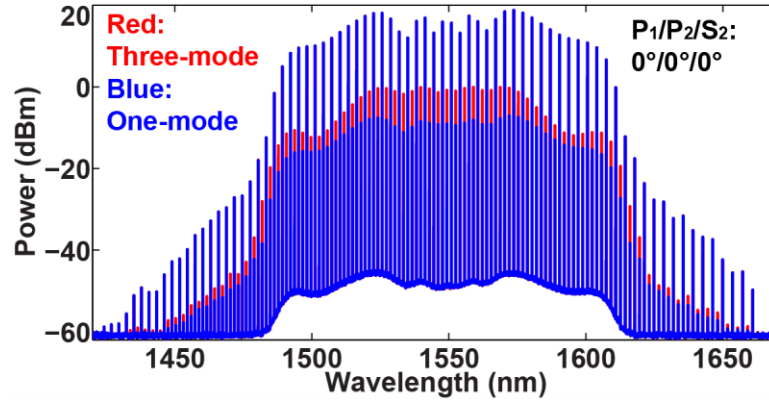


Figure 5.3 Simulated spectral comparison between one- and three-mode PS multicasting. Red: three-mode. Blue: one-mode.

However, in practical terms, the input waves are subject to the ambient induced phase fluctuations (e.g. acoustic and temperature perturbations), leading to an instable output spectrum. Consequently, a PLL is demanded by the PS operation. Next, we will discuss and compare the phase relations of the one- and three-mode multicasting, resulting in different PLL implementations.

Regarding the one-mode process, to achieve the maximum multicasting G/CE, the input three waves should satisfy the phase matching condition, as expressed in Eq. 5.1.

$$\theta_{P1} + \theta_{P2} = 2\theta_{S2} \quad 5.1$$

Therefore, the maximum multicasting G/CE was guaranteed by the synchronized phase arrangement, shown as the blue curve in Fig. 5.3. In contrast to the 4MPS scheme (requiring dual-pump phase locking), PS one-mode multicasting can be stabilized by one-pump PLL. Take another phase arrangement as an example, when the phases of P_2 and S_2 were randomly chosen as $50^\circ/70^\circ$, PLL can manipulate the

phase of P_1 to 90° , according to the phase matching requirement. Correspondingly, Fig. 5.4(a) shows the simulated spectrum with phase setting of $90^\circ/50^\circ/70^\circ$ ($P_1/P_2/S_2$), exhibiting the same G/CE profile with the phase synchronized condition (blue curve in Fig. 5.3).

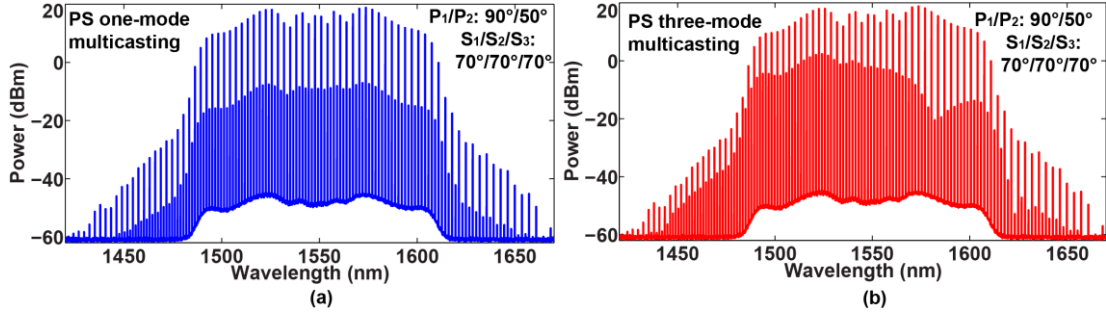


Figure 5.4 Simulated spectra of one- and three-mode PS multicasting, with different phase arrangements. (a) PS one-mode spectrum with phase setting of $P_1/P_2/S_2: 90^\circ/50^\circ/70^\circ$. (b) PS three mode spectrum with phase setting of $P_1/P_2/S_1/S_2/S_3: 90^\circ/50^\circ/70^\circ/70^\circ/70^\circ$.

In contrast, three-mode wavelength multicasting has more complex phase matching requirements, as denoted in Eq. 5.2

$$\theta_{P_1} + \theta_{P_2} = 2\theta_{S_2} \quad (5.2a)$$

$$\theta_{S_1} + \theta_{S_2} = 2\theta_{P_1} \quad (5.2b)$$

$$\theta_{S_2} + \theta_{S_3} = 2\theta_{P_2} \quad (5.2c)$$

$$\theta_{S_1} + \theta_{S_3} = 2\theta_{S_2} \quad (5.2d)$$

In practical terms, the three signals are sharing the same waveguide, resulting in constant phase relation between the input three signals (see Eq. 5.2(d)). However, relying on one-pump PLL, only P_1 is phase locked to P_2 and S_2 (see Eq. 5.2(a)), but the phase relations in Eq. 5.2(b) and (c) are not guaranteed. Again, take the phase arrangement $P_1/P_2/S_1/S_2/S_3: 90^\circ/50^\circ/70^\circ/70^\circ/70^\circ$ as an example, Eq. 5.2(a) is satisfied by manipulating one-pump phase through PLL, and the simulated spectrum is shown in Fig. 5.4(b). Compared to the spectrum with synchronized phase setting (red curve in Fig. 5.3), the output spectrum in Fig. 5.4(b) is neither equalized nor maximized. In

other words, the PS three-mode wavelength multicasting needs a dual-pump PLL, same as the 4MPS case. In all the above simulations, the SBS and Raman scattering were neglected, while the pumps and signal(s) were assumed as co-polarized for maximum mixing efficiency.

Phase dependence of one- and three-mode wavelength multicasting

Furthermore, the phase dependent properties of the degenerate one- and three-mode multicasting were simulated by sweeping the phase of the signal wave at 1549.3 nm, as shown in Fig. 5.5(a) and (b), respectively. Specifically, with the signal phase (at 1549.3 nm) swept from 0° to 360° and other input waves initialized as 0° , the output spectra and output power of the central 11 signal copies were inspected. Consequently, the phase transfer characteristic of the one-mode PS multicasting (see Fig. 5.5(a)) is sinusoid with periodic of π rad, exactly as predicted by the phase matching condition in Eq. 5.1. In contrast, when two more signal waves get involved, we can find a distinct phase dependence for the three-mode multicasting, a sinusoid trend with periodic of 2π rad, as shown in Fig. 5.5(b). Here, the red solid curves in Fig. 5.5 represent the signal wave at 1549.3 nm. The magenta and blue curves denote the signal waves at 1546.1 and 1552.5 nm in Fig. 5.5(b) (for three-mode multicasting), respectively. While all the newly generated signal copies are manifested in black solid curves in Fig. 5.5.

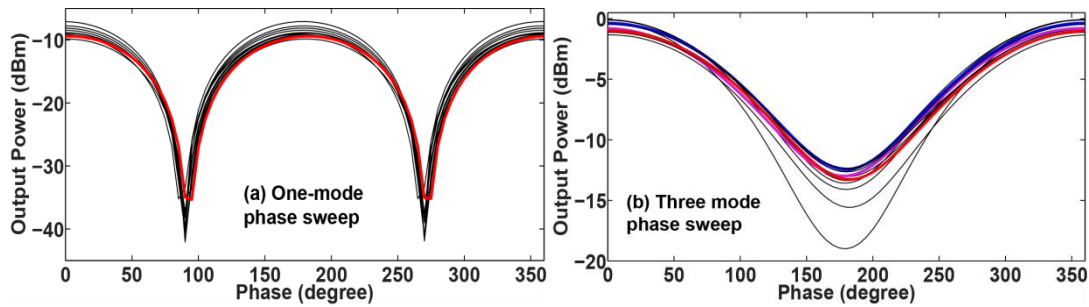


Figure 5.5 Phase dependent properties of one- and three-mode PS wavelength multicasting. (a) One-mode phase transfer characteristic. (b) Three-mode phase transfer characteristic.

5.3 Experimental demonstration

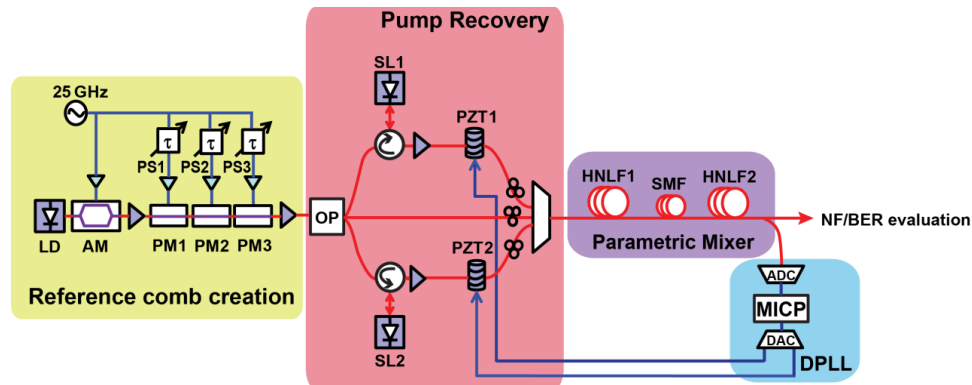


Figure 5.6 Experimental setup configuration, including reference comb, pump recovery, parametric mixer and DPLL. LD: laser diode, AM: amplitude modulator, PM: phase modulator, PS: phase shifter, OP: optical processor, SL: slave laser, PZT: piezoelectric transducer, HNLF: highly nonlinear fiber, SMF: single mode fiber, ADC: analog to digital converter, DAC: digital to analog converter, MICP: microprocessor, DPLL: digital phase-locked loop.

We next proceed to the experimental implementation of the PS single- and multi-mode parametric multicasting. Fig. 5.6 shows the experimental architecture for dual-pump driven parametric multicasting, consisting of four partitions.

In the first module, cascaded modulators were utilized to create an optical frequency comb, providing mutually correlated waves, as well as defining the frequency reference for the subsequent wavelength multicasting. Specifically, a narrow linewidth laser at 1549.3 nm was launched into a tandem combination of one

AM and three PMs. The driving RF tone on the modulators defines the frequency reference comb with a 25-GHz grid. As shown in Fig. 5.7(a), the corresponding optical reference comb with 6-nm 10-dB-bandwidth was achieved by manipulating the AM bias and RF delays into the PMs.

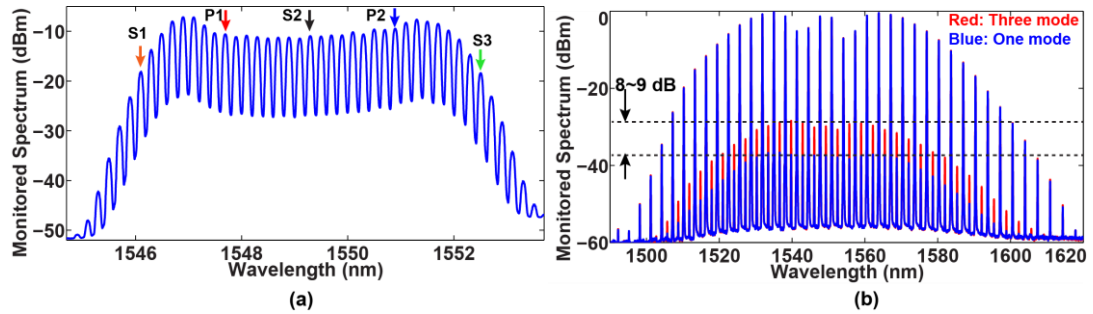


Figure 5.7 Monitored optical spectra of reference comb (a) and multicasting output (b).

Subsequent to the amplified frequency reference comb, the seeds of two pumps (1547.7 and 1550.9 nm) and signal(s) were derived by an OP and de-multiplexed into three fiber branches. In the signal path, one wave at 1549.3 nm was selected for single-mode operation, whereas three waves were picked by the OP for multi-mode PS process. In each pump path, injection locking was employed for attaining pump wave with high SNR and output power, as well as maintaining the phase correlation between the input waves. After further amplification to 33 dBm by high power EDFA, the pumps were combined with the co-polarized signal(s) and launched into the parametric mixer.

As reported in the previous chapters and analyzed in Section 5.2, to obtain exceedingly highly efficient parametric multicasting, a three-stage dispersion-engineered parametric mixer follows the pump recovery module. The first two stages were a HNLF (HNLF1, characterized by a ZDW of 1597 nm, dispersion slope of

0.018 ps/nm²/km, and nonlinear coefficient of 22 km⁻¹W⁻¹) and a 6-m SMF. The final stage is a 230-m dispersion flatten HNLF2 with peak dispersion of -0.2 ps/nm/km.

To make the comparison between simulations and experiments clearer, several statements need to be clarified here. First, contrary to the simulations in Section 5.2, the SBS cannot be neglected in practice and thus the 105-m long HNLF1 was longitudinal strained in sections with different tensions to elevate the Brillouin threshold [45]. Secondly, the fibers utilized in the simulations have constant (non-varying) ZDWs, differing from the experimental conditions. To compensate for the longitudinal variation of the dispersion governed phase matching condition and practically obtain highly efficient wavelength multicasting, different HNLF parameters were utilized in the simulations and experiments. For example, the HNLF1 in the experiment has a global shifted dispersion profile compared to the simulation, selected to achieve highly efficient wavelength multicasting. Finally, in practical terms, the PS process is subject to the ambient induced phase fluctuations, resulting from the interferometric pump recovery module. Consequently, at the output of the parametric mixer, a small fraction of the power was utilized for phase tracking and compensation by a PLL, as detailed in [57]. Whereas majority of the output power was launched into the a tunable narrow bandwidth filter to extract a specific replica copy for further postprocessing.

Fig. 5.7(b) shows the PLL stabilized experimental spectra of the one- and three-mode wavelength multicasting. The blue curve represents the spectrum of the PS one-mode multicasting, stabilized by a one-pump PLL. We note that the signal phase optimization is unnecessary here, owing to the phase matching condition in Eq. 5.1

can be satisfied automatically by the one-pump PLL. In contrast, the three-mode multicasting spectrum, shown in red curve, having a 3-dB flatness over 12 copies and 8~9-dB G/CE improvement, was stabilized by a dual-pump DPLL [19]. In addition, the equalized and maximum three-mode multicasting needs single signal phase optimization, as predicted in the complex phase matching condition of Eq. 5.2.

5.4 Discussion on ultra-low noise performance

In this section, we compare the PS one- and three-mode wavelength multicasting, in terms of NF and BER performance. As aforementioned, one-mode PS process has been employed in the phase regenerator [98] and regenerative multicaster [97], where the parametric device is operated in the saturation mode. In contrast, this chapter focuses on the ultra-low noise performance of the wavelength multicasting, and the theoretical analysis and experiments were implemented with low input signal power, i.e. linear gain regime, in order to accurately evaluate the NF defined with shot noise limited input signal.

At the output of the parametric mixer, a specific copy was extracted by a narrow bandwidth filter, photo-detected, amplified and then launched into an ESA for measuring noise PSD. The NF was calculated by the RIN subtraction method, as detailed in [62]. Fig. 5.8 shows the experimental G/CE and NF profiles for the central 5 copies of the one- and three-mode wavelength multicasting. The G/CE profiles are represented in blue curves, while the blue dashed curve manifests the one-mode process, and the blue solid curve denotes the three-mode case. Here, a 8 to 9 dB G/CE improvement can be observed, resulting from the three-fold coherent field

combinations. Furthermore, the red dashed curve represents the NF spectrum for one-mode multicasting. As predicted by the NF estimation in Section 5.2, the PS one-mode multicasting has a quantum limit NF of 3-dB and the measured lowest NF for the one-mode process is 3.6 dB. Most importantly here, the three-mode case possesses a lowest NF of 1-dB and all the central five copies have NFs lower than 3 dB.

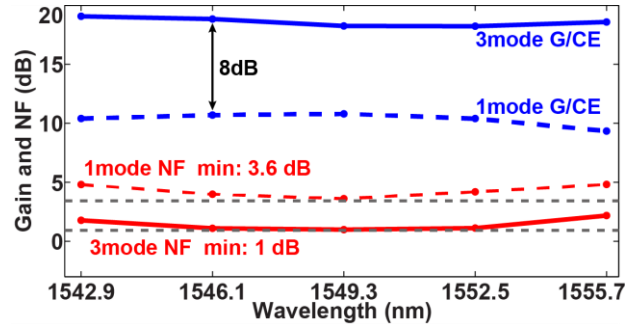


Figure 5.8 Experimental G/CE and NF comparisons over 5 replica copies between one- and three-mode multicasting. Blue dashed: one-mode G/CE. Blue solid: three-mode G/CE. Red dashed: one-mode NF. Red solid: three-mode NF.

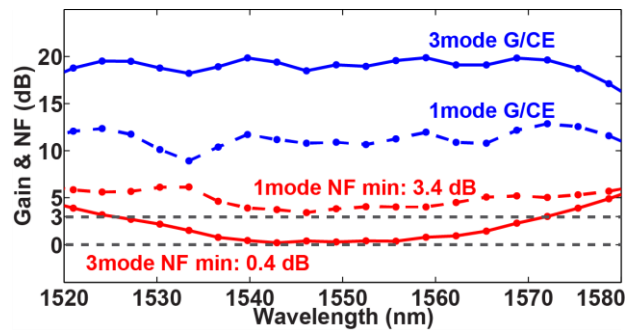


Figure 5.9 Simulated G/CE and NF comparisons over 5 replica copies between one- and three-mode multicasting. Blue dashed: one-mode G/CE. Blue solid: three-mode G/CE. Red dashed: one-mode NF. Red solid: three-mode NF.

To further corroborate the great potential of the multi-mode operation, the noise performance of the wavelength multicasting in the three-stage dispersion-synthesized parametric mixer was calculated and presented in Fig. 5.9. Here, the simulated parameters for the parametric mixer and input waves were exactly the same

as the theoretical analysis in Fig. 5.3 (see *Three-stage dispersion synthesized parametric mixer* in Section 5.2). The simulated lowest NF for three-mode scheme is 0.4 dB, and additionally, there are 15 signal copies, having NFs lower than quantum limit NF of 3-dB. We note that the comparison between the NF diagrams in the experiment (see Fig. 5.8) and simulation (see Fig. 5.9) manifests the most critical result in this chapter. In the three-mode experiment, only five copies show NF lower than quantum limit NF of 3-dB. In contrast, the simulation in Fig. 5.9, implemented with different dispersion profiles of HNLFs, presents exceptional noiseless multicasting, implying that dispersion engineering is essential to the noiseless performance of wavelength multicasting. We believe that relying on more precise dispersion manipulation in the parametric mixer, it is possible to achieve efficient wavelength multicasting with scalable high count copy number and noiseless performance.

While the experimental characterization on noise performance in Fig. 5.8 also shows a discrepancy from the quantum limit NF. For example, one-mode process has a quantum limit NF of 3-dB (see Fig. 5.2), but the lowest NF for the practically implemented one-mode multicasting is 3.6 dB in the experiment (see Fig. 5.8), which is attributed to the inadequate noise localization resulting from the SBS limited mixer length.

Furthermore, the BER performance of the experimental wavelength multicasting was evaluated at 1549.3, 1552.5 and 1555.7 nm. As predicted in Fig. 5.8, the central copies at 1549.3 and 1552.5 nm have comparable noise performance with a commercial EDFA, thus possessing similar BER performances with the BTB

benchmark, measured for single signal wave (at 1549.3 nm) amplification by an EDFA with NF of 4.1 dB. Note that the BTB benchmark (EDFA amplification) is denoted as the black solid curve in Fig. 5.10, whereas the red (blue) dashed curve represents the BER performance for the signal copy at 1549.3 nm (1552.5 nm) in the one-mode PS multicasting. In comparison, the corresponding BER curves at 1549.3 and 1552.5 nm in the three-mode wavelength multicasting have a 2-dB negative sensitivity penalty, marked as the red and blue solid curves in Fig. 5.10, respectively. The purple dashed curve in Fig. 5.10 shows the BER performance of the signal copy at 1555.7 nm for one-mode wavelength multicasting, whereas the purple solid curve represents the BER curve of 1555.7 nm for three-mode architecture. Due to the degraded noise performance at 1555.7 nm, the BER curves exhibit sensitivity penalty, compared to the signal copies at 1549.3 and 1552.5 nm. However, we still can conclude that PS multi-mode multicasting has unprecedented performance improvement compared to the PS one-mode case.

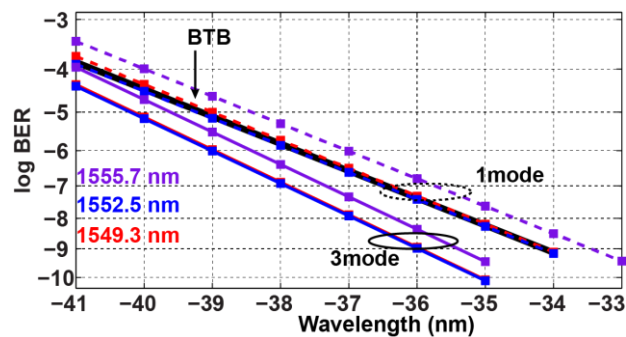


Figure 5.10 BER performance comparison between one- and three-mode wavelength multicasting. BTB is represented by the black solid curve. Dashed curves denote the one-mode wavelength multicasting over 1549.3, 1552.5 and 1555.7 nm. Solid colored curves shows the BER performance of the three-mode multicasting.

5.5 Summary

Dual-pump degenerate one- and three-mode PS processes, operated in unsaturated regime, were employed in the dispersion engineered parametric mixer. The analysis on the input phase relations indicates that a one-pump PLL can stabilize one-mode PS multicasting; on the other hand, a three-mode scheme requires a dual pump DPLL, same as the 4MPS condition. Moreover, the experimental results demonstrate ultra-low noise performance over 5 multicasted copies, and the lowest NF for three-mode operation is 1 dB, the record low noise performance for wavelength multicasting. While a 2-dB BER sensitivity improvement between three- and one-mode multicasting further confirms the superiority of the multi-mode PS operation. Most importantly, the extended simulations indicate that, relying on a dispersion precisely controlled parametric mixer, wavelength multicasting with noiseless performance over sizable copy number can be achieved, providing unprecedented advantages for various applications in signal processing and commercial services.

Chapter 5, in full, is a reprint of the material currently being prepared for submission for publication, contributed by Lan Liu, Andreas O. J. Wiberg, Bill. P.-P. Kuo, Evgeny Myslivets, Nikola Alic and Stojan Radic, "Comparison of One- and Three-Mode Phase Sensitive Wavelength Multicasting." The dissertation author was the primary investigator and author/co-author of this article.

Chapter 6 Summary and Future work

6.1 Summary

An ideal wavelength multicasting should possess compatibility to WDM network and full transparency to arbitrary modulation formats, in addition to preserve the integrity and SNR of the input signal over scalable high count copy number. In contrast to the conventional technologies, demanding the output signal carriers be externally seeded during the multicasting process, highly efficient self-seeded wavelength multicasting can be implemented by a dispersion managed fiber mixer. In addition to the scalable high count copy number, the ultra-low noise wavelength multicasting based on the dispersion-managed fiber mixer operated in the multi-mode PS architecture was demonstrated in the unsaturated and saturated gain regimes in this dissertation.

Recognized by the broad conversion bandwidth, instantaneous response speed and full transparency to arbitrary modulation formats, parametric effect has been identified as an efficient means for amplification and wavelength conversion. In particular, the advent of the multi-stage dispersion-managed fiber mixer makes the scalable and efficient wavelength multicasting achievable. The PI parametric wavelength multicasting, relying on the dispersion synthesized parametric mixer, was numerically investigated in Chapter 2. The simulation results indicated that the dual-pump driven PI one-mode wavelength multicasting has a quantum limit NF of 6-dB, stemming from the localized noise coupling in normally dispersive fiber mixer.

In comparison, the PS parametric process, amplifying the inphase quadrature but de-amplifying the out-of-phase component, has gained substantial attention in recent years, owing to its great potential in noiseless amplification and phase squeezing. Specifically, the PS process superimposes the correlated photons at identical (degenerate) or distinct (non-degenerate) wavelengths for constructive field summation, in addition to the parametric effect induced nonlinear gain, leading to ultra-low noise performance. Chapter 3 describes the basic principle of the 4MPS parametric multicasting, followed by the investigations on the phase manipulation and theoretical noiseless performance. Experimental demonstrations verified the feasibility of manipulating two-pump phases for tracking and compensating for the phase fluctuation to obtain the stabilized wavelength multicasting. In addition, one signal phase management allows the maximized multicasting G/CE profile, while the HoFWM terms can be mitigated by optimizing the phases of the multi-mode input signals. Besides, experimental characterization confirmed the record performance of the 4MPS wavelength multicasting, in terms of NF, BER sensitivity and multicasting copy number.

The ultra-low noise parametric multicasting was enabled by the coherent signal field combination and incoherent noise localized coupling, and therefore, the experimental implementation requires low input signal power, i.e. working in the unsaturated gain regime. In Chapter 4, we furthered our study into the saturated 4MPS multicasting with relatively high input signal power. The power transfer characteristics of the 4MPS multicaster indicated its enhanced capability of removing amplitude perturbations. Combined with the saturation effect enabled amplitude noise

regeneration, the phase errors were regenerated by the phase dependent amplification and de-amplification in the 4MPS multicaster. The experimental implementation and record performances were reported in Chapter 4.

Dual-pump driven parametric mixer, identified as an efficient means for wavelength multicasting, has different frequency configurations for input signals. In addition to the PI one-mode and 4MPS scheme presented, PS one- and three-mode wavelength multicasting was investigated in Chapter 5, to further corroborate the superiority of the multi-mode PS wavelength multicasting.

6.2 Future work

The dissertation has addressed the need for ultra-low noise wavelength multicasting through the multi-mode PS parametric mixer. Nevertheless, many open questions need to be further considered; for example, the ultimate noiseless wavelength multicasting over sizable copy number demands more research efforts, and the regenerative multicasting should have transparency to complex modulation formats, such as quadrature phase shifted keying (QPSK) and quadrature amplitude modulation (QAM). Recognizing these great potentials of the wavelength multicasting, we propose possible future directions in this section.

First, phase management is pivotal to the PS parametric process. Chapter 3 introduced the principle and implementation of the DPLL structure, an essential module for the stabilized multicasting. Specifically, the utilized DPLL possesses a 3-kHz locking bandwidth, tracking and compensating for the ambient induced phase and power fluctuations. The feasibility of the DPLL highly relies on the accessible

hardware, including phase stretcher, real-time processor and high-voltage amplifier. In particular, advanced real-time processor with complex algorithm would lead to a further increase in the locking bandwidth and would allow the PS multicasting be operating in harsh environments exposed to rapid mechanical and temperature shocks.

In addition to the phase manipulation, dispersion engineering is another prerequisite for the efficient and ultra-low noise wavelength multicasting. Chapter 2 and 3 mathematically derived the theoretical NF for the PI and 4MPS wavelength multicasting, indicating a quantum limit NF of 6-dB for the PI case and noiseless performance for the PS scheme. Particularly, numerical simulation of the G/CE and NF profiles for the parametric multicasting has revealed that normally dispersive mixer with localized noise coupling, combined with the PS architecture, allows the noiseless multicasting. However, the bandwidth of the wavelength multicasting, another important factor for the high count copy number, is also governed by the dispersion profile. In effect, the normal dispersion induced phase mismatch reduces the multicasting bandwidth to a certain extent. Therefore, further investigations on the normally dispersive mixer are demanded to balance the tradeoff between the bandwidth and localized noise coupling.

Furthermore, the experimental demonstrations on NF and BER performance in Chapter 3 present the record-low noise performance for wavelength multicasting over 17 signal copies. However, theoretically, the 4MPS multicasting possesses noiseless performance over high count copy number. The discrepancy between the theory and experiment is primarily ascribed to the SBS limited mixer length and its induced inadequate noise localization. In effect, to achieve the ultimate noiseless wavelength

multicasting, precise and complex dispersion manipulation for the fiber mixer is needed for simultaneous realization of broad bandwidth and noise localization. It is conceivable that the multi-mode PS parametric mixer with advanced dispersion and phase manipulation can potentially lead to noiseless multicasting, possessing critical importance to wide-ranging applications in signal processing and commercial services.

To increase the transmission capacity and efficiency, advanced modulation formats, such as QPSK and QAM, have been developed and widely employed in commercial applications. Chapter 4 discloses the great potential of the 4MPS parametric mixer as an all-optical regenerative multicaster. However, the proposed implementation is only effective for BPSK modulation format. Therefore, it is essential to design new experimental architecture for multicasting signal with advanced modulation formats. For example, the optical frequency reference comb, providing frequency-locked and phase-correlated pumps and signals, can be implemented by a FOPA, instead of modulator concatenation. Specifically, phase conjugated signals can be created by the FOPA, enabling the QPSK signal multicasting. On the other hand, wavelength multicasting with QAM modulation format, particularly 16-QAM, requires even more research efforts to solve the unequal phase quantization and multi-level amplitude regeneration.

A final consideration regarding the future direction is utilizing integration platform for practical wavelength multicasting. In this dissertation, the wavelength multicaster is achieved by the fiber mixer, requiring precise dispersion and phase manipulation. However, with a highly efficient integrated nonlinear platform, not only the demands of strict phase management might be mitigated, but also it is an enabling

technology to propel the wavelength multicasting from research to commercial deployment.

Bibliography

- [1] T. Miya, Y. Terunuma, T. Hosaka, and T. Miyashita, "Ultimate low-loss single-mode fiber at 1.55 μm ," *Electronics Letters*, vol. 15, no. 4, pp. 106-108, 1979.
- [2] T. Y. Li, "The impact of optical amplifiers on long-distance lightwave telecommunications," *Proceedings of the IEEE*, vol. 81, no. 11, pp. 1568-1579, Nov. 1993.
- [3] N. S. Bergano, "Wavelength division multiplexing in long-haul transoceanic transmission systems," *Journal of Lightwave Technology*, vol. 23, no. 12, pp. 4125-4139, Dec. 2005.
- [4] C. A. Brackett, "Dense wavelength division multiplexing networks: principles and applications," *IEEE Journal on Selected Areas in Communications*, vol. 8, no. 6, pp. 948-964, Aug. 1990.
- [5] L. H. Sahasrabudde and B. Mukherjee, "Light-trees: optical multicasting for improved performance in wavelength-routed networks," *IEEE Communications Magazine*, vol. 37, no. 2, pp. 67-73, Feb. 1999.
- [6] R. Malli, X. Zhang, and C. Qiao, "Benefit of multicasting in all-optical networks," *Conference on All-Optical Networking: Architecture, Control, and Management Issues*, pp. 209-220, Boston, MA, 1998.
- [7] G. N. Rouskas, "Optical layer multicast: rationale, building blocks, and challenges," *IEEE Network*, vol. 17, no. 1, pp. 60-65, Jan.-Feb. 2003.
- [8] C. H. Kwok, S. H. Lee, K. K. Chow, C. Shu, L. Chinlon, and A. Bjarklev, "Polarization-insensitive all-optical wavelength multicasting by self-phase-modulation in a photonic-crystal fiber," *Conference on Lasers and Electro-Optics (CLEO)*, CTuD4, Long Beach, CA, 2006.
- [9] W. Wei, L. Rau, and D. J. Blumenthal, "All-optical label switching/swapping of 160 Gbps variable length packets and 10 Gbps labels using a WDM Raman enhanced-XPM fiber wavelength converter with unicast/multicast operation," *Optical Fiber Communication Conference (OFC)*, PDP8, Los Angeles, CA, 2004.
- [10] C. S. Bres, N. Alic, E. Myslivets, and S. Radic, "Scalable multicasting in one-pump parametric amplifier," *Journal of Lightwave Technology*, vol. 27, no. 3, pp. 356-363, Feb. 2009.
- [11] C. S. Bres, A. O. J. Wiberg, B. P. P. Kuo, N. Alic, and S. Radic, "Wavelength multicasting of 320-Gb/s channel in self-seeded parametric amplifier," *IEEE Photonics Technology Letters*, vol. 21, no. 14, pp. 1002-1005, Jul. 2009.

- [12] G. Contestabile, N. Calabretta, R. Proietti, and E. Ciaramella, "Double-stage cross-gain modulation in SOAs: An effective technique for WDM multicasting," *IEEE Photonics Technology Letters*, vol. 18, no. 1, pp. 181-183, Jan. 2006.
- [13] T. Durhuus, B. Mikkelsen, C. Joergensen, S. L. Danielsen, and K. E. Stubkjaer, "All-optical wavelength conversion by semiconductor optical amplifiers," *Journal of Lightwave Technology*, vol. 14, no. 6, pp. 942-954, June 1996.
- [14] M. Fujiwara, N. Shimosaka, M. Nishio, S. Suzuki, S. Yamazaki, S. Murata, and K. Kaede, "A coherent photonic wavelength-division switching system for broadband networks," *14th European Conference on Optical Communication (ECOC)*, pp. 139-42 vol.1, Brighton, 1988.
- [15] J. M. H. Elmirghani and H. T. Mouftah, "All-optical wavelength conversion: Technologies and applications in DWDM networks," *IEEE Communications Magazine*, vol. 38, no. 3, pp. 86-92, Mar. 2000.
- [16] E. Myslivets, B. P. P. Kuo, N. Alic, and S. Radic, "Generation of wideband frequency combs by continuous-wave seeding of multistage mixers with synthesized dispersion," *Optics Express*, vol. 20, no.3, pp. 3331-3344, Jan. 2012.
- [17] B. P. P. Kuo, E. Myslivets, N. Alic, and S. Radic, "Wavelength multicasting via frequency comb generation in a bandwidth-enhanced fiber optical parametric mixer," *Journal of Lightwave Technology*, vol. 29, no.23, pp. 3515-3522, Dec. 2011.
- [18] Z. Tong, L. Liu, A. O. J. Wiberg, V. Ataie, E. Myslivets, B. P. P. Kuo, N. Alic, and S. Radic, "First Demonstration of Four mode phase sensitive Multicasting of Optical Channel," *Conference on Lasers and Electro-Optics (CLEO)*, CTh5D.6, San Jose, CA, 2013.
- [19] A. J. Wiberg, D. J. Esman, L. Liu, J. R. Adleman, S. Zlatanovic, V. Ataie, E. Myslivets, B. P. P. Kuo, N. Alic, E. W. Jacobs, and S. Radic, "Coherent filterless wideband microwave/millimeter-wave channelizer based on broadband parametric mixers," *Journal of Lightwave Technology*, vol. 32, no. 20, pp. 3609-3617, Oct. 2014.
- [20] A. O. J. Wiberg, L. Liu, Z. Tong, E. Myslivets, V. Ataie, B. P. P. Kuo, *et al.*, "Photonic preprocessor for analog-to-digital-converter using a cavity-less pulse source," *Optics Express*, vol. 20, no. 26, pp. B419-B427, Dec. 2012.
- [21] D. J. Esman, A. O. J. Wiberg, Y. Mu-Han, L. Liu, B. P. P. Kuo, N. Alic and S. Radic, "Photonic parametric sampled analog-to-digital conversion at 100 GHz and 6 ENOBs," *40th European Conference on Optical Communication (ECOC)*, Mo.3.5.6, Cannes, France, 2014.
- [22] V. Ataie, E. Myslivets, B. P. P. Kuo, N. Alic, and S. Radic, "Spectrally equalized frequency comb generation in multistage parametric mixer with

- nonlinear pulse shaping,” *Journal of Lightwave Technology*, vol. 32, no. 4, pp. 840-846, Feb. 2014.
- [23] V. Ataie, E. Temprana, L. Liu, Y. Myslivets, P. P. Kuo, N. Alic, and S. Radic, “Flex-grid compatible ultra wide frequency comb source for 31.8 Tb/s coherent transmission of 1520 UDWDM channels,” *Optical Fiber Communication Conference (OFC)*, Postdeadline Th5B.7, San Francisco, CA, 2014.
- [24] R. Tang, P. L. Voss, J. Lasri, P. Devgan, and P. Kumar, “Noise-figure limit of fiber-optical parametric amplifiers and wavelength converters: experimental investigation,” *Optics Letters*, vol. 29, no. 20, pp. 2372-2374, Oct. 2004.
- [25] Z. Tong, A. O. J. Wiberg, E. Myslivets, C. K. Huynh, B. P. P. Kuo, N. Alic, and Stojan Radic, “Noise performance of phase-insensitive frequency multicasting in parametric mixer with finite dispersion,” *Optics Express*, vol. 21, no. 15, pp. 17659-17669, Jul. 2013.
- [26] W. Imajuku, A. Takada, and Y. Yamabayashi, “Low-noise amplification under the 3dB noise figure in high-gain phase-sensitive fibre amplifier,” *Electronics Letters*, vol. 35, pp. 1954-1955, Oct. 1999.
- [27] M. Asobe, T. Umeki, and O. Tadanaga, “Phase sensitive amplification with noise figure below the 3 dB quantum limit using CW pumped PPLN waveguide,” *Optics Express*, vol. 20, no. 12, pp. 13164-13172, June 2012.
- [28] Z. Tong, C. Lundstrom, P. A. Andrekson, C. J. McKinstrie, M. Karlsson, D. J. Blessing, E. Tipsuwannakul, B. J. Puttnam, H. Toda and L. Gruner-Nielsen, “Towards ultrasensitive optical links enabled by low-noise phase-sensitive amplifiers,” *Nature Photonics*, vol. 5, pp. 430-436, July 2011
- [29] Z. Tong, A. O. J. Wiberg, E. Myslivets, B. P. P. Kuo, N. Alic, and S. Radic, “Broadband parametric multicasting via four-mode phase-sensitive interaction,” *Optics Express*, vol. 20, no. 17, pp. 19363-19373, Aug. 2012.
- [30] G. P. Agrawal, *Nonlinear fiber optics*. Oxford: Academic, 2013.
- [31] Y. R. Shen, *The principles of nonlinear optics*. New York: J. Wiley, 1984.
- [32] C. J. McKinstrie, S. Radic, and A. R. Chraplyvy, “Parametric amplifiers driven by two pump waves,” *IEEE Journal of Selected Topics in Quantum Electronics*, vol. 8, no. 3, pp. 538-547, May-June 2002.
- [33] H. A. Haus, “The noise figure of optical amplifiers,” *IEEE Photonics Technology Letters*, vol. 10, no.11, pp. 1602-1604, Nov. 1998.
- [34] Y. Yamamoto and K. Inoue, “Noise in amplifiers,” *Journal of Lightwave Technology*, vol. 21, no. 11, pp. 2895-2915, Nov. 2003.
- [35] C. H. Henry and R. F. Kazarinov, “Quantum noise in photonics,” *Reviews of Modern Physics*, vol. 68, no. 3, pp. 801-853, July 1996.

- [36] C. J. McKinstrie, S. Radic, and M. G. Raymer, "Quantum noise properties of parametric amplifiers driven by two pump waves," *Optics Express*, vol. 12, no. 21, pp. 5037-5066, Oct. 2004.
- [37] C. J. McKinstrie, M. Yu, M. G. Raymer, and S. Radic, "Quantum noise properties of parametric processes," *Optics Express*, vol. 13, no. 13, pp. 4986-5012, June 2005.
- [38] S. Radic, "Parametric Signal Processing," *IEEE Journal of Selected Topics in Quantum Electronics*, vol. 18, no. 2, pp. 670-680, Mar-Apr 2012.
- [39] C. M. Caves, "Quantum limits on noise in linear amplifiers," *Physical Review D*, vol. 26, pp. 1817-1839, 1982.
- [40] R. Slavik, F. Parmigiani, J. Kakande, C. Lundstrom, M. Sjodin, P. A. Andrekson, R. Weerasuriya, S. Sygletos, A. D. Ellis, L. Gruner-Nielsen, D. Jakobsen, S. Herstrom, R. Phelan, J. O'Gorman, A. Bogris, D. Syvridis, S. Dasgupta, P. Petropoulos, and D. Richardson, "All-optical phase and amplitude regenerator for next-generation telecommunications systems," *Nature Photonics*, vol. 4, pp. 690-695, Oct. 2010.
- [41] T. Richter, R. Elschner, and C. Schubert, "QAM phase-regeneration in a phase-sensitive fiber-amplifier," *39th European Conference on Optical Communication (ECOC)*, We.3.A.2, pp. 489-491, London, UK, 2013.
- [42] K. Croussore and G. F. Li, "Phase and amplitude regeneration of differential phase-shift keyed signals using phase-sensitive amplification," *IEEE Journal of Selected Topics in Quantum Electronics*, vol. 14, no. 3, pp. 648-658, May-June 2008.
- [43] M. Vasilyev, "Distributed phase-sensitive amplification," *Optics Express*, vol. 13, no. 19, pp. 7563-7571, Sep 2005.
- [44] T. Richter, B. Corcoran, S. L. Olsson, C. Lundstrom, M. Karlsson, C. Schubert, and P. A. Andrekson, "Experimental characterization of a phase-sensitive four-mode fiber-optic parametric amplifier," *38th European Conference on Optical Communication (ECOC)*, Th.1.F.1, Amsterdam, The Netherlands, 2012.
- [45] E. Myslivets, C. Lundstrom, J. M. Aparicio, S. Moro, A. O. J. Wiberg, C. S. Bres, N. Alic, P. A. Andrekson, and S. Radic, "Spatial equalization of zero-dispersion wavelength profiles in nonlinear fibers," *IEEE Photonics Technology Letters*, vol. 21, no. 24, pp. 1807-1809, Dec. 2009.
- [46] B. Corcoran, S. L. I. Olsson, C. Lundstrom, M. Karlsson, and P. Andrekson, "Phase-sensitive optical pre-amplifier implemented in an 80 km DQPSK link," *Optical fiber communication conference (OFC)*, PDP5A.4, pp. 1-3, Los Angeles, CA, 2012.
- [47] T. Sakamoto, G. W. Lu, A. Chiba, and T. Kawanishi, "Digital optical phase locked loop for real-time coherent demodulation of multilevel PSK/QAM,"

Optical Fiber Communication Conference(OFC), OMS5, San Diego, CA, 2010.

- [48] Y. X. Ma, P. Zhou, X. L. Wang, H. T. Ma, X. J. Xu, L. Si, Z. J. Liu, and Y. Zhao, "Coherent beam combination with single frequency dithering technique," *Optics Letters*, vol. 35, no. 9, pp. 1308-1310, May 2010.
- [49] Z. X. Xu, X. Zhang, K. K. Huang, and X. H. Lu, "A digital optical phase-locked loop for diode lasers based on field programmable gate array," *Review of Scientific Instruments*, vol. 83, Sep. 2012.
- [50] T. Torounidis, H. Sunnerud, P. O. Hedekvist, and P. A. Andrekson, "Amplification of WDM signals in fiber-based optical parametric amplifiers," *IEEE Photonics Technology Letters*, vol. 15, no. 8, pp. 1061-1063, Aug. 2003.
- [51] F. Forghieri, R. W. Tkach, A. R. Chraplyvy, and D. Marcuse, "Reduction of four-wave mixing crosstalk in WDM systems using unequally spaced channels," *IEEE Photonics Technology Letters*, vol. 6, no. 6, pp. 754-756, June 1994.
- [52] M. Jamshidifar, A. Vedadi, and M. E. Marhic, "Reduction of four-wave-mixing crosstalk in a short fiber-optical parametric amplifier," *IEEE Photonics Technology Letters*, vol. 21, no. 17, pp. 1244-1246, Sep. 2009.
- [53] F. A. Callegari, J. M. C. Boggio, and H. L. Fragnito, "Spurious four-wave mixing in two-pump fiber-optic parametric amplifiers," *IEEE Photonics Technology Letters*, vol. 16, no. 2, pp. 434-436, Feb. 2004.
- [54] J. L. Blows, "Design strategy for controlling four-wave mixing-induced crosstalk between channels in a fibre optical parametric amplifier," *Optics Communications*, vol. 236, pp. 115-122, June 2004.
- [55] K. K. Y. Wong, G. W. Lu, and L. K. Chen, "Experimental studies of the WDM signal crosstalk in two-pump fiber optical parametric amplifiers," *Optics Communications*, vol. 270, pp. 429-432, Feb. 2007.
- [56] K. K. Y. Wong, G. W. Lu, and L. K. Chen, "Polarization-interleaved WDM signals in a fiber optical parametric amplifier with orthogonal pumps," *Optics Express*, vol. 15, no. 1, pp. 56-61, Jan. 2007.
- [57] L. Liu, Z. Tong, A. O. J. Wiberg, B. P. P. Kuo, E. Myslivets, N. Alic, and S. Radic, "Digital multi-channel stabilization of four-mode phase-sensitive parametric multicasting," *Optics Express*, vol. 22, no. 15, pp. 18379-18388, July 2014.
- [58] L. Liu, Z. Tong, A. O. Wiberg, Y. Myslivets, P. P. Kuo, N. Alic, and S. Radic, "Conversion efficiency and crosstalk optimization in four-mode phase-sensitive multicasting mixer by vectorial phase manipulation," *Optical Fiber Communication Conference (OFC)*, Tu2K.4, San Francisco, California, 2014.
- [59] L. Liu, A. O. J. Wiberg, E. Myslivets, B. P. P. Kuo, N. Alic, and S. Radic, "Suppression of Inter-channel Higher Order Four Wave Mixing in Four-Mode

- Phase-Sensitive Parametric Wavelength Multicasting, ” *Journal of Lightwave Technology*, vol. 33, no. 11, pp. 2324-2331, June 2015.
- [60] J. Hansryd, P. A. Andrekson, M. Westlund, J. Li, and P. O. Hedekvist, “Fiber-based optical parametric amplifiers and their applications,” *IEEE Journal of Selected Topics in Quantum Electronics*, vol. 8, no. 3, pp. 506-520, May-Jun 2002.
- [61] L. Liu, Z. Tong, A. O. J. Wiberg, E. Myslivets, B. Kuo, N. Alic, and Stojan Radic, “Digital phase-locked loop-stabilized four-mode phase-sensitive parametric multicasting,” *39th European Conference and Exhibition on Optical Communication (ECOC)*, We.3.A.4, London, UK, 2013.
- [62] G. Obarski, “Precise calibration for optical amplifier noise figure measurement using the RIN subtraction method,” *Optical Fiber Communications Conference (OFC)*, ThZ3, 2003.
- [63] M. Movassaghi, M. K. Jackson, V. M. Smith, and W. J. Hallam, “Noise figure of erbium-doped fiber amplifiers in saturated operation,” *Journal of Lightwave Technology*, vol. 16, no. 5, pp. 812-817, May 1998.
- [64] L. Liu, E. Temprana, V. Ataie, E. Myslivets, B. P. P. Kuo, A. O. J. Wiberg, N. Alic, and S. Radic, “Demonstration of enhanced amplitude regeneration in four-mode phase-sensitive parametric multicasting mixer,” *40th European Conference on Optical Communication (ECOC)*, Tu. 1. 4. 2, Cannes, France, 2014.
- [65] L. Liu, E. Temprana, V. Ataie, B. P. P. Kuo, E. Myslivets, A. O. J. Wiberg, N. Alic, and S. Radic, “The first demonstration of phase and amplitude regenerative multicasting by a four-mode phase-sensitive process,” *IEEE Photonics Conference (IPC)*, WB2.4, San Diego, CA, 2014.
- [66] L. Thylen, G. Karlsson, and O. Nilsson, “Switching technologies for future guided wave optical networks: potentials and limitations of photonics and electronics,” *IEEE Communications Magazine*, vol. 34, no. 2, pp. 106-113, Feb 1996.
- [67] J. P. Gordon and L. F. Mollenauer, “Phase noise in photonic communications systems using linear amplifiers,” *Optics Letters*, vol. 15, no. 23, pp. 1351-1353, Dec. 1990.
- [68] C. J. McKinstrie and C. Xie, “Phase jitter in single-channel soliton systems with constant dispersion,” *IEEE Journal of Selected Topics in Quantum Electronics*, vol. 8, no. 3, pp. 616-625, May-Jun 2002.
- [69] P. V. Mamyshev and E. Telefon, “All-optical data regeneration based on self-phase modulation effect,” *24th European Conference on Optical Communication*, 1998.

- [70] M. Matsumoto, "Efficient all-optical 2R regeneration using self-phase modulation in bidirectional fiber configuration," *Optics Express*, vol. 14, no. 23, pp. 11018-11023, Nov. 2006.
- [71] S. Boscolo, S. K. Turitsyn, and K. J. Blow, "Nonlinear loop mirror-based all-optical signal processing in fiber-optic communications," *Optical Fiber Technology*, vol. 14, no. 4, pp. 299-316, Oct. 2008.
- [72] Y. Su, L. Wang, A. Agarwal, and P. Kumar, "All-optical limiter using gain flattened fibre parametric amplifier," *Electronics Letters*, vol. 36, no. 13, pp. 1103-1105, June 2000.
- [73] S. Radic, C. J. McKinstrie, R. M. Jopson, J. C. Centanni, and A. R. Chraplyvy, "All-optical regeneration in one- and two-pump parametric amplifiers using highly nonlinear optical fiber," *IEEE Photonics Technology Letters*, vol. 15, no. 7, pp. 957-959, July 2003.
- [74] E. Ciaramella and S. Trillo, "All-optical signal reshaping via four-wave mixing in optical fibers," *IEEE Photonics Technology Letters*, vol. 12, no. 7, pp. 849-851, July 2000.
- [75] K. Inoue and T. Mukai, "Experimental study on noise characteristics of a gain-saturated fiber optical parametric amplifier," *Journal of Lightwave Technology*, vol. 20, no. 6, pp. 969-974, June 2002.
- [76] E. Ciaramella, F. Curti, and S. Trillo, "All-optical signal reshaping by means of four-wave mixing in optical fibers," *IEEE Photonics Technology Letters*, vol. 13, no. 2, pp. 142-144, Feb 2001.
- [77] M. Matsumoto and H. Sakaguchi, "DPSK signal regeneration using a fiber-based amplitude regenerator," *Optics Express*, vol. 16, no. 15, pp. 11169-11175, July 2008.
- [78] M. Matsumoto and Y. Morioka, "Fiber-based all-optical regeneration of DPSK signals degraded by transmission in a fiber," *Optics Express*, vol. 17, no. 8, pp. 6913-6919, Apr. 2009.
- [79] C. Kouloumentas, M. Bougioukos, A. Maziotis, and H. Avramopoulos, "DPSK regeneration at 40 Gb/s and beyond using a fiber-sagnac interferometer," *IEEE Photonics Technology Letters*, vol. 22, no. 16, pp. 1187-1189, Aug. 2010.
- [80] K. Croussore and G. Li, "Amplitude regeneration of RZ-DPSK signals based on four-wave mixing in fibre," *Electronics Letters*, vol. 43, no. 3, pp. 177-178, Feb. 2007.
- [81] M. Matsumoto and K. Sanuki, "Performance improvement of DPSK signal transmission by a phase-preserving amplitude limiter," *Optics Express*, vol. 15, no. 13, pp. 8094-8103, June 2007.
- [82] M. Matsumoto and T. Kamio, "Nonlinear phase noise reduction of DQPSK signals by a phase-preserving amplitude limiter using four-wave mixing in

- fiber,” *IEEE Journal of Selected Topics in Quantum Electronics*, vol. 14, no. 3, pp. 610-615, May-June 2008.
- [83] X. Liu, X. Wei, R. E. Slusher, and C. J. McKinstrie, “Improving transmission performance in differential phase-shift-keyed systems by use of lumped nonlinear phase-shift compensation,” *Optics Letters*, vol. 27, no. 18, pp. 1616-1618, Sep. 2002.
- [84] J. Hansryd, J. V. Howe, and C. Xu, “Experimental demonstration of nonlinear phase jitter compensation in DPSK modulated fiber links,” *IEEE Photonics Technology Letters*, vol. 17, no. 1, pp. 232-234, Jan. 2005.
- [85] K. P. Ho, “Mid-span compensation of nonlinear phase noise,” *Optics Communications*, vol. 245, pp. 391-398, Jan. 2005.
- [86] C. J. McKinstrie, S. Radic, and C. Xie, “Reduction of soliton phase jitter by in-line phase conjugation,” *Optics Letters*, vol. 28, no. 17, pp. 1519-1521, Sep. 2003.
- [87] A. Pejkic, R. R. Nissim, E. Myslivets, A. O. J. Wiberg, N. Alic, and S. Radic, “All-optical switching in a highly efficient parametric fiber mixer: design study,” *Optics Express*, vol. 22, no. 19, pp. 23512-23527, Sep. 2014.
- [88] S. Zlatanovic, J. S. Park, S. Moro, J. M. C. Boggio, I. B. Divliansky, N. Alic, S. Mookherjea, and S. Radic, “Mid-infrared wavelength conversion in silicon waveguides using ultracompact telecom-band-derived pump source,” *Nature Photonics*, vol. 4, pp. 561-564, Aug. 2010.
- [89] M. Matsumoto, “Fiber-Based All-Optical Signal Regeneration,” *IEEE Journal of Selected Topics in Quantum Electronics*, vol. 18, no. 2, pp. 738-752, Mar-Apr 2012.
- [90] B. J. Puttnam, D. Mazroa, S. Shinada, and N. Wada, “Phase-squeezing properties of non-degenerate PSAs using PPLN waveguides,” *Optics Express*, vol. 19, no. 26, pp. 131-139, Dec. 2011.
- [91] K. Bergman and H. A. Haus, “Squeezing in fibers with optical pulses,” *Optics Letters*, vol. 16, no. 9, pp. 663-665, May 1991.
- [92] G. Bartolini, L. Ruo-Ding, P. Kumar, W. Riha, and K. V. Reddy, “1.5-um phase-sensitive amplifier for ultrahigh-speed communications,” *Optical Fiber Communication Conference(OFC)*, pp. 202-203, 1994,.
- [93] M. E. Marhic, C. H. Hsia, and J. M. Jeong, “Optical amplification in a nonlinear fiber interferometer,” *Electronics Letters*, vol. 27, no. 3, pp. 210-211, Jan. 1991.
- [94] W. Imajuku and A. Takada, “In-line optical phase-sensitive amplifier with pump light source controlled by optical phase-lock loop,” *Journal of Lightwave Technology*, vol. 17, no. 4, pp. 637-646, Apr. 1999.

- [95] K. Croussore, C. Kim, and G. F. Li, "All-optical regeneration of differential phase-shift keying signals based on phase-sensitive amplification," *Optics Letters*, vol. 29, no. 20, pp. 2357-2359, Oct. 2004.
- [96] K. Croussore and G. F. Li, "Phase regeneration of NRZ-DPSK signals based on symmetric-pump phase-sensitive amplification," *IEEE Photonics Technology Letters*, vol. 19, no. 11, pp. 864-866, May-June 2007.
- [97] R. Slavik, A. Bogris, J. Kakande, F. Parmigiani, L. Gruner-Nielsen, R. Phelan, J. Vojtech, P. Petropoulos, D. Syvridis, and D. J. Richardson, "Field-trial of an all-optical PSK regenerator/multicaster in a 40 Gbit/s, 38 channel DWDM transmission experiment," *Journal of Lightwave Technology*, vol. 30, no. 4, pp. 512-520, Feb. 2012.
- [98] A. Bogris, D. Syvridis, and C. Efstathiou, "Noise properties of degenerate dual pump phase sensitive amplifiers," *Journal of Lightwave Technology*, vol. 28, no. 8, pp. 1209-1217, Apr. 2010.